Investigation of a Millimeter Wave with a Helical Wavefront

by

Yuki Goto, M. Eng.

Dissertation Presented for the Degree of
Doctor of Engineering

Department of Applied Energy
Graduate School of Engineering
Nagoya University

Supervisor
Dr. Shin Kubo

Acknowledgments

First of all, I wish to thank my supervisor Dr. Shin Kubo. He provided me the most important guidance, encouragement, and invaluable support throughout my doctoral course. I was very happy to be able to study again under his supervision. I am convinced that my decision to return to graduate school after working in the private sector under his supervision was the correct choice.

I am grateful to my dissertation committee: Dr. Shinya Yagi, Dr. Hiroaki Nakamura, and Dr. Masahiko Katoh. Thank you very much for your invaluable comments and advise.

I also would like to thank Dr. Toru Ii Tsujimura and Mr. Hidenori Takubo. Through discussions with Dr. Tsujimura I obtained many research ideas and knowledge. And, our experimental device would not exist were it not for Mr. Takubo. Thank you very much.

I am grateful that I could join the "Optical Vortex group," which is one of the National Institutes of Natural Sciences (NINS) joint research programs. They gave me many chances to make presentations and engage in discussions. These were productive every time and further enhanced my knowledge. Thank you very much.

In addition, I would like to express my thanks to Dr. Tomio Petrosky, of the University of Texas at Austin (UT). He taught me many things about life, philosophy, culture, and history etc. as well as physics that I would not have learned without him. During my stay in the United States for six months, I went to many places and have experienced many things. However, my favorite place is in front of his blackboard where we discussed physics for many hours. I will never forget the days I spent with him in UT. My research there is not yet finished. However, I will continue that research in the future. My mind is still there.

Special thanks to my lab mate Max and Corey, and to my friends of the conversation table: Grant, Michel, and Cameron. I was really happy because I could stay in UT with all of them. I want to express my greatest thanks for their support throughout my stay. They really made my life easier. Without their help, I could not have stayed for six months, and I might have returned to Japan. Thanks y'all.

I would like to thank the TOBITATE scholarship. I was very happy to receive an opportunity to study at the UT. This program is extremely valuable because it evaluates what students want to do rather than what they can do now. I hope this program will

continue for the next generation.

Please do not be angry if your name is not included here. I have not forgotten that I was supported by so many people, many of whom I cannot thank here. Thank you all very much.

Finally, I would like to thank my family, Dad, Mam, and sisters. Please forgive me for making up my mind many times without telling you. I guess you were worried about me. I don't know what will happen to my life in the future. However, I will never forget being helped by you so many times. Now, I will start new my life.

The author wishes to express his thanks to the Institute for Molecular Science (IMS) for supporting some of the experimental devices. This research was supported by the grant of Joint Research by the National Institutes of Natural Sciences (NINS) (NINS program no. 01111701), by a grant from The Murata Science Foundation, by the NIFS grant ULRR033, and by the NINS program for cross-disciplinary study (grant no. 01311802).

Abstract

In 2017, it was theoretically shown that the higher harmonics radiation from charged particles in spiral motion has a helical wavefront. Since electron cyclotron motion is a kind of spiral motion, Electron Cyclotron Emission (ECE) should also have a helical wavefront. ECE exists commonly in nature, such as in the interaction between the solar wind and Earth's magnetosphere, magnetic reconnection in solar flares, and radiation from magnetic confinement fusion plasma. However, observations of the ECE with helical wavefront have never been reported and experimental demonstration is expected to make a significant contribution to these studies as well.

Laguerre–Gaussian (LG) beam with a helical wavefront known as an optical vortex is shown by Allen *et al.* in 1992. Optical vortex has been actively studied since the approximate solution of the wave equation in the cylindrical coordinate system showed the presence of an angular momentum that does not depend on the polarization. A beam with a helical wavefront has a donut-shaped intensity distribution, which does not have intensity on the beam axis, and has the orbital angular momentum in addition to the spin angular momentum which depends on the polarization. Many research fields utilized these characteristics for applications, such as nanostructure formation by matter-optical vortex interaction, the interaction between the magnetic material and an optical vortex, chemical researches of molecules with asymmetry, and telecommunication by controlling orbital angular momentum.

The optical vortex is passively generated by conversion from a Gaussian beam without a helical wavefront using an optical element, for example, a spiral phase plate, computer-generated holography, and q-plate. An optical vortex can be easily produced by those passive methods at a visible frequency. But at other frequencies, producing an optical vortex is difficult due to restrictions of the available optical elements. However, if we can control the electron motion, we can obtain any waveband of a vortex beam. Therefore, there is a great significance in actively generating the beams with helical wavefront in any wavebands by controlling the rotation frequency of the charged particle.

At present, the generation experiments for the beam with helical wavefront actively generated in a shorter wavelength regime such as γ-rays and extreme ultraviolet are intensively carried out. In the γ-ray regime, it is possible to generate a γ-ray with a helical wavefront by using inverse Compton scattering by specifically colliding low-energy laser

photons with circular polarization with a high-energy electron. And, the donut-shaped intensity distribution for the radiation with helical wavefront in γ-ray was observed. In the extreme ultraviolet regime, by passing an electron through a helical undulator, a relativistic electron with a spiral trajectory is generated, and the radiation with a helical wavefront is obtained.

On the other hand, the studies of active radiation with helical wavefront in the longer wavelength regime such as millimeter-wave have not been reported yet. This is because the measurement focusing on the helical wavefront has never been carried out. In addition, the phase of the ECE from the multi-electron system is usually cancelled out due to the random rotation phase of each electron. In order to demonstrate the ECE with helical wavefront, we designed and developed an experimental device that generates the ECE with helical wavefront in multi-electron system. In this experiment, we attempt to control the rotation phase of electrons with cyclotron motion by externally applied circularly polarized wave so that the coherent radiation can be generated. This experiment is equivalent to the principle of Electron Cyclotron Resonance Heating (ECRH) in fusion plasma. In the fusion plasma, the ECRH plays an important role in which it is necessary to produce and maintain the high temperature plasma electron. Then, electrons in the plasma are in the state where the rotation phase of each electron is locally controlled by externally applied electromagnetic wave. And then, such electrons produce the coherent ECE with helical wavefront as well. By thermalizing the resonantly accelerated electrons, that is, being randomized for the rotation phase of each electron, the helical wavefront of ECE should be cancelled out. Therefore, time scale of appearance and disappearance for the helical wavefront provides an indication of the coherent acceleration and the thermalization of the electrons. In this basic experiment, producing a pure group of electrons and measuring the ECE in millimeter-wave regime with helical wavefront greatly contribute to the understanding of plasma heating physics in fusion research.

In this study, we conducted comprehensive studies 1) - 4), concerning measuring the helical wavefront of ECE in the millimeter-wave regime, which is a longer wavelength band than such as the γ-ray and the ultraviolet; 1) We carried out the numerical calculations of ECE with a helical wavefront from the electron with a cyclotron motion in magnetic field accelerated by a circularly polarized wave; 2) An experimental device was developed based on the obtained numerical calculation results; 3) A grating mirror that separates fundamental radiation and second harmonic radiation from ECE, including higher harmonics radiation, was developed and a general theory concerning development of grating mirror was also developed; 4) We developed a method for measurement of a beam with a helical wavefront by a triangular aperture. The details of these research results are presented below.

1) Numerical calculation regarding ECE with a helical wavefront from an electron accelerated by a circularly polarized wave.

In this calculation, a Right-Handed Circularly Polarized (RHCP) wave was applied to an electron with cyclotron motion. And radiation from the rotation phase-controlled electron was performed. The helical wavefront of the ECE cancels out due to the random rotation phase of the multi-electron system and it has not been experimentally observed that the cyclotron radiation from a multi-electron system as well as that from a single electron has a helical wavefront. However, our calculation shows that the rotation phase of the electron can be controlled by high power RHCP wave by accelerating the electron with cyclotron motion resonantly and then demonstrates the coherent radiation with a helical wavefront. We calculated two types of external magnetic fields: one is a static uniform magnetic field, the other is the magnetic mirror field. The system in which an electron in cyclotron motion under the uniform magnetic field is accelerated by circularly polarized wave is the simplest case of the ECRH. And the system gives us a basic behavior of the electron. In addition, the system where an electron in cyclotron motion under the magnetic mirror field is accelerated by circularly polarized wave is the experimental system. This calculation with magnetic mirror field greatly contributes to the understanding of the experimental results.

In the case of a static uniform magnetic field, when the RHCP wave is applied to the electron with cyclotron motion, the electron receives energy from the incident RHCP wave and the relativistic mass gradually increases. Thus, the Larmor radius increases and the cyclotron frequency decreases. Meanwhile, the electron is accelerated in the z-direction (magnetic field direction) by the Lorentz force $\boldsymbol{\beta}_\perp \times \boldsymbol{B}_{\mathrm{in}}$ ($\boldsymbol{\beta}_\perp$: the electron perpendicular velocity, $\boldsymbol{B}_{\mathrm{in}}$: the magnetic component of the externally applied electromagnetic wave), and reaches a relativistic velocity. In this case, the frequency of the RHCP wave seen from the reference frame of electron is observed to be downshifted due to the Doppler effect. The results confirmed a phenomenon called cyclotron auto-resonance, i.e., the relativistic electron cyclotron frequency and the downshifted frequency of RHCP wave seen from the reference frame of electron are almost equal and electron maintains the resonance state. In addition, it was confirmed that the direction of the externally applied electric field and the acceleration direction of the electron were in the same direction. Also, the electron was trapped by the RHCP wave. Although this calculation is performed for a single electron, the same phenomenon occurs for each electron in a multi-electron system. Therefore, by applying RHCP wave to a multi-electron system with a initial random rotational phase, the rotational phase of each electron is controlled and coherent radiation with a helical wavefront can be obtained.

Radiation from the electron in a such a state was calculated using the Liénard-Wiechert potential and observed on the upper hemisphere. As a result, only the fundamental radiation appears in the frequency spectrum on the z-axis ($\theta = 0$), and the spectrum of higher harmonics radiation did not appear. However, a spectrum of

radiation including higher harmonics was observed at a position distant from the optical axis. The absence of harmonics radiation on the optical axis (z-axis) indicates that the intensity distribution of higher harmonics radiation is donut-shaped. This indicates that active radiation from the charged particle with spiral motion produces helical wavefront - one of the characteristics of the vortex beam. In addition, we calculated the phase difference of the radiation at the symmetric point with respect to the beam axis. The higher harmonics have the phase difference with the relationship of $180(n-1)$ deg. (n: harmonic number), while the fundamental radiation has no phase difference. These results suggest that ECE has a helical wavefront from the characteristics of donut-shaped intensity distribution and azimuth-dependent phase structure.

The same calculation was performed for the magnetic mirror field. We confirmed that ECE has a helical wavefront even in the magnetic mirror field, which can be easily realized experimentally. ECE with a helical wavefront will be generated by interaction between the electrons with cyclotron motion in the magnetic mirror field accelerated by the externally applied RHCP wave.

2) Development of the experimental device producing ECE with a helical wavefront.

We designed and constructed the experimental device that generates the ECE with helical wavefront based on the numerical calculation as mentioned in point 1). We created magnetic mirror configuration by the use of superconducting coils. Into such a magnetic field we supplied a group of electrons. An electron gun at the bottom of the device was used as source. The group of electrons follows cyclotron motion and travels to the interaction region. Then, the RHCP wave is applied from the outside to accelerate the electron at the resonance region and control the rotation phase. As a result, coherent cyclotron radiation including fundamental radiation and higher harmonics radiation can be obtained. However, since these optical axes regarding fundamental radiation and higher harmonics radiation are coaxial, they are separated into fundamental radiation and second harmonic radiation by a grating mirror. The separated fundamental radiation is guided to the dummy load, and the second harmonic radiation is measured by the measurement system. This experimental device has already been designed and constructed, including a transmission system for guiding the RHCP wave from the gyrotron.

3) Development of the grating mirror and its general theory.

A grating mirror has been developed to separate only the second harmonic radiation from the fundamental and higher harmonics radiation in the experimental device of 2). A grating mirror with a blaze angle and line spacing that satisfies the Littrow condition is designed so that the second harmonic radiation can be effectively separated. In other words, the line spacing of the grating mirror and the blaze angle is optimized so that the propagation direction of the -1st order wave

diffracted by the grating and the wave reflected on the slope on the saw-tooth is the same. Therefore, low power second harmonic radiation can be effectively measured. This grating mirror is a planar type for the convenience of machining, but in this study, we generalized the design method of the grating mirror and succeeded in defining a grating mirror with an arbitrary surface shape. When parameters such as the focal point, the waist size of the input Gaussian beam, and the output of the m-th order diffracted wave are given, a grating can be designed on the mirror surface.

4) Development of the measurement system for a beam with helical wavefront by a triangular aperture.

We have developed a measurement system to detect a helical wavefront radiation separated by a grating mirror. Although radiation with a helical wavefront is common in nature, that radiation has not been measured yet. This is either because of the lack of a measurement system or an attempt to measure the a helical wavefront. Here, the diffraction method by an aperture is excellent because the diffraction can be caused by each photon. That is, the helical wavefront can be identified even if it is not coherent radiation. However as mentioned, since the harmonics ECE have low power, it is important to produce spatially coherent electrons by the externally applied electromagnetic wave for improving the sensitivity of the measurement.

Given this, we have developed a diffraction method of the wave with helical wavefront using a triangular aperture. In order to develop the measurement system, we need the beam source with a helical wavefront in the millimeter wave spectrum. First, we developed a device called a spiral mirror which passively converts a Gaussian beam into vortex beams. The mirror surface of the spiral mirror has a helical shape, which changes continuously in the azimuth direction and the mirror center is a singular point whose height is not defined. We have developed six kinds of spiral mirrors, one for each Topological Charge (TC) from -3 to +3 except for 0. TC = 0 is a normal mirror. We have also confirmed that each mirror produced a donut-shaped intensity distribution. Therefore, since we have obtained a stable continuous-wave source with a helical wavefront, the measurement system can be developed.

According to the Huygens-Fresnel principle, when a beam with helical wavefront passes through the aperture, a characteristic diffraction pattern appears according to its TC. In the case of a triangular aperture, the symmetric diffraction pattern appears depending on the sign of TC. Using a triangular aperture with a larger area is more appropriate for our purpose than other types of apertures because more diffracted light can be obtained. In the experiment, an equilateral triangular aperture with a side of 40 mm was used. Also, the aperture's optical system was designed and calibrated so that the optical axis and the center of gravity of the triangular aperture coincide. In the experiment, we obtained the characteristic diffraction patterns which resemble polka dot patterns. The data acquisition was made by

a sub-THz imaging camera. These experimental results were perfectly compatible with the calculation results based upon Kirchhoff's diffraction formula, which is an exact mathematical expression of the Huygens-Fresnel principle. In addition, we also confirmed that the characteristic diffraction patterns did not appear when the Gaussian beam without a helical wavefront was injected into a triangular aperture. Therefore, we were able to detect a millimeter-wave with a helical wavefront and to identify the TC.

This diffraction method by an aperture can be applied to the radiation without phase coherence because the pattern is a result of self interference pattern for diffracted and non-diffracted beam.

Contents

Acknowledgments **i**

Abstract **iii**

List of Figures **xi**

List of Tables **xvii**

1 Introduction **1**
1.1 History of the Wave with an Orbital Angular Momentum and the Characteristics of the Wave . . . 1
1.2 How to Generate the Optical Vortex . . . 3
1.3 Application of the Optical Vortex . . . 5
1.3.1 Production of Nanostructure . . . 5
1.3.2 Communication using a Vortex Beam in Millimeter Wave Regime . 5
1.4 Vortex Radiation from a Charged Particle in Spiral Motion . . . 6
1.5 Progress of the Wavelength Spectrum regarding Actively Generated Vortex Beams . . . 9
1.6 Purpose of the Research . . . 11
1.6.1 Electron Cyclotron Emission . . . 12
1.7 Vortex Radiation from the Gyrotron . . . 12
1.8 Composition of this Dissertation . . . 13

Bibliography **14**

2 Basic Theory **17**
2.1 Charged Particle Motion . . . 17
2.1.1 Cyclotron Motion in the Externally Applied Electromagnetic Field . 17
2.2 Radiation Theory . . . 21
2.2.1 Maxwell's Equation . . . 21
2.2.2 Gauge Transformation . . . 22
2.2.3 Liénard Wiechert Potential . . . 25

2.3 Diffraction Theory . . . 29
2.3.1 Huygens-Fresnel Principle . . . 29
2.3.2 Kirchhoff's Diffraction Formula . . . 31

Bibliography **35**

3 Calculations of ECE with Helical Wavefront **36**
3.1 Outline for the Calculations . . . 36
3.2 In the Case of a Static Magnetic Field . . . 37
3.2.1 Electron Trajectory in the Electromagnetic Wave . . . 39
3.2.2 Regarding Application to Multi-electron System . . . 43
3.2.3 Observation of the ECE with Helical Wavefront . . . 45
3.2.4 Transverse Doppler Shift by Traveling with Relativistic Velocity in Cyclotron Motion . . . 47
3.2.5 Phase Difference Observed at Two Spatial Points . . . 49
3.2.6 Intensity Distribution and Phase Structure . . . 52
3.3 In the Case of a Magnetic Mirror Field . . . 54
3.3.1 Electron Trajectory in the Electromagnetic Wave . . . 54
3.3.2 Observation of the ECE with Helical Wavefront . . . 59
3.3.3 Transverse Doppler Shift by Traveling with Relativistic Velocity in Cyclotron Motion . . . 62
3.3.4 Phase Difference Observed at Two Spatial Points . . . 65
3.4 Summary . . . 71

Bibliography **73**

4 Experimental Devices **74**
4.1 Arrangement . . . 74
4.2 Concept of the Experiment . . . 74
4.3 Gyrotron . . . 75
4.4 Matching Optics Unit . . . 77
4.5 Transmission System . . . 79
4.6 Polarizer . . . 79
4.7 Interaction Vacuum Chamber . . . 80

Bibliography **87**

5 Development of the Grating Mirror **88**
5.1 Grating Condition . . . 88
5.2 Low Power Test . . . 89
5.3 General Theory of the Grating Mirror Development . . . 89
5.3.1 Definition of the Mirror Surface . . . 90

5.3.2 Relationship between Grating Condition and Mirror Surface 91
5.4 Summary 94

Bibliography **96**

6 Development of the Measurement System **97**
6.1 Development of the Spiral Mirror 97
6.1.1 Spiral Mirror with Flat Surface 97
6.1.2 Spiral Mirror with Focusing 98
6.2 Diffraction Method by a Triangular Aperture 99
6.2.1 Experimental Setup 100
6.2.2 Huygens-Fresnel Principle 102
6.2.3 Experiment and Calculation Results 103
6.3 Direct Phase Measurement 106
6.3.1 Heterodyne System 106
6.3.2 Two Spatial Points Measurement by Heterodyne Detectors 107
6.4 Summary 110

Bibliography **111**

7 Summary **115**

List of Figures

1.1 The phase front structure and the intensity distribution (a): Gaussian beam as HG_{00} mode. (b): Optical vortex as LG_{01} mode. 3
1.2 The intensity distribution regarding HG_{mn} mode and LG_{lp} mode. 3
1.3 Passive methods for producing a optical vortex. (a): Spiral phase plate [8]. (b): Computer-generated hologram [9]. (c): Q-plate [11]. 4
1.4 The nanoneedle produced by an optical vortex. Since the optical vortex has positive and negative topological charge depending on the direction of the spiral, a chiral nanostructure can be created [12]. 5
1.5 Telecommunication using optical vortex. Since each optical vortex with different topological charge is orthogonal to each other, it is possible to communicate by OAM-MDM [14]. 6
1.6 The coordinate system for deriving the radiation theory where an electron with spiral motion produces electromagnetic field with helical wavefront actively [7]. 8
1.7 The intensity distribution and the direction of the electric fields at a given time [7]. (a): fundamental radiation, (b): second harmonic radiation, and (c): third harmonic radiation. 9
1.8 The experimental results at the UVSOR synchrotron facility. For the first time, it has been demonstrated that the radiation from high-energy electron with spiral motion in helical undulator has a helical wavefront [7]. 10
1.9 The method to generate γ-ray with helical wavefront. When the laser used for the laser Compton scattering is circularly polarized, the scattered photons by high-energy electron produce the γ-ray with helical wavefront [21]. 11
1.10 The radiation with helical wavefront from the gyrotron cavity in millimeter-wave regime. The vortex radiation is produced by the whispering gallery mode [23]. 13

2.1 Huygens-Fresnel Principle. (a): In the case of plane wave. (b): In the case of spherical wave. A wavefront at a given time produces wavelets at each point on the wavefront as a wave source, then the wavelets propagate as a spherical wave. And the envelope in contact with the wavefronts of the wavelet becomes a new wavefront at the next time step. 30

3.1 Calculation flow. First, solve the eq.(2.26) for obtaining the trajectory information, and then calculate the radiation by substituting the trajectory information into Liénard-Wiechert potential. 38
3.2 Coordinate system of the calculation where an electron with cyclotron motion in magnetic field is accelerated by the RHCP wave. The angle α between the line of sight of the observer and the propagation direction of the electron is also defined. 39
3.3 Trajectory information and some parameters. (a): Part of the electron trajectory when the RHCP wave is applied into an electron with cyclotron motion in static uniform magnetic field from the outside. (b)-(d): Trajectory information concerning positions, velocities, and accelerations. (e): Relativistic electron cyclotron frequency and Doppler-shifted frequency of RHCP wave seen from the reference frame of electron with relativistic velocity. (f): Kinetic energy of the electron. (g): Phase relationships between the acceleration of the electron in the x-y direction $\dot{\boldsymbol{\beta}}_\perp$and the electric field $\boldsymbol{E}_{\rm in}$, also between the velocity of the electron in the x-y direction $\boldsymbol{\beta}_\perp$ and the magnetic field $\boldsymbol{B}_{\rm in}$, which are defined by eq.(3.3) and eq.(3.4). 42
3.4 Change of frequency for $\cos\phi_{\boldsymbol{E}}$ and $\sin\phi_{\boldsymbol{B}}$ when the power of $\boldsymbol{E}_{\rm in}$ is changed from 100 kW to 1000 kW by 100 kW. 43
3.5 Spatial coherence of the electrons. If the injected beam is high power, each phase relationship between the electric field vector and the acceleration vector of the electron is the same at a given z plane. 44
3.6 Time variation of the spectrum observed on the upper hemisphere at the distance from the origin $|\boldsymbol{R}| = 15$ m, each θ on $\phi = 0$. 46
3.7 Time variation of the frequency calculated by eq.(3.7) observed at each θ. When θ is small, the $\cos\alpha$ becomes negative, and the observer receives radiation with blue-shifted frequency larger than $\omega_{{\rm ce},\gamma}$. On the other hand, when θ is large, the $\cos\alpha$ becomes positive and the observer receives radiation with red-shifted frequency smaller than $\omega_{{\rm ce},\gamma}$. 48
3.8 Time variation of the cosine value of the phase difference between $\phi = 0$ deg. and $\phi = 90$ deg. calculated by eq.(3.8). 50
3.9 Time variation of the cosine value of the phase difference between $\phi = 0$ deg. and $\phi = 180$ deg. calculated by eq.(3.8). 51
3.10 Intensity distribution and phase structure of the fundamental radiation and second harmonic radiation at $t = 70.4$ n sec. Both figures are projected on the x-y plane. The arrows indicate the direction of the electric field at a given time and place, and the color bars indicate the power of the electric field, which is normalized by the maximum value. The power is time-averaged. 52
3.11 FFT results of the Fig.3.11, which is observed from 70 n sec. 53

3.12 Externally applied magnetic mirror field structure used by the calculation with a normalized magnetic field strength by the maximum value on the optical axis at the origin. (a): Spatial distribution on x-z plane. (b): Spatial distribution on the optical axis. 55
3.13 Trajectory information and some parameters when the magnetic field is set to 2.286 T and the energy in z-direction has 18 keV. (a): Electron trajectory (b)-(d): Trajectory information concerning positions, velocities, and accelerations. (e): The magnetic field strength along the electron trajectory. (f): Electron cyclotron frequency along the electron trajectory. (g): Kinetic energy of the electron. 57
3.14 Trajectory information and some parameters when the magnetic field is set to 2.909 T and the energy in z-direction has 0.1 keV. (a): Electron trajectory (b)-(d): Trajectory information concerning positions, velocities, and accelerations. (e): The magnetic field strength along the electron trajectory. (f): Electron cyclotron frequency along the electron trajectory. (g): Kinetic energy of the electron. 58
3.15 Time variation of the spectrum observed on the upper hemisphere at the distance from the origin $|\boldsymbol{R}| = 3$ m, each θ on $\phi = 0$ when the magnetic field is set to 2.286 T and the energy in z-direction has 18 keV. The spectra intensity are measured by log scale. 60
3.16 Time variation of the spectrum observed on the upper hemisphere at the distance from the origin $|\boldsymbol{R}| = 3$ m, each θ on $\phi = 0$ when the magnetic field is set to 2.909 T and the energy in z-direction has 0.1 keV. The spectra intensity are measured by log scale. 61
3.17 Time variation of the frequency calculated by eq.(3.7) observed at each θ when the magnetic field is set to 2.286 T and the energy in z-direction has 18 keV. 63
3.18 Time variation of the frequency calculated by eq.(3.7) observed at each θ when the magnetic field is set to 2.909 T and the energy in z-direction has 0.1 keV. 64
3.19 Time variation of the cosine value of the phase difference between $\phi = 0$ deg. and $\phi = 90$ deg. calculated by eq.(3.8) when the magnetic field is set to 2.286 T and the energy in z-direction has 18 keV. 67
3.20 Time variation of the cosine value of the phase difference between $\phi = 0$ deg. and $\phi = 180$ deg. calculated by eq.(3.8) when the magnetic field is set to 2.286 T and the energy in z-direction has 18 keV. 68
3.21 Time variation of the cosine value of the phase difference between $\phi = 0$ deg. and $\phi = 90$ deg. calculated by eq.(3.8) when the magnetic field is set to 2.909 T and the energy in z-direction has 0.1 keV. 69

3.22 Time variation of the cosine value of the phase difference between $\phi = 0$ deg. and $\phi = 180$ deg. calculated by eq.(3.8) when the magnetic field is set to 2.909 T and the energy in z-direction has 0.1 keV. 70

4.1 Arrangement of the radiation control area where our experimental equipment is installed. 75
4.2 Schematic diagram of the experimental device which produces the ECE with helical wavefront. 76
4.3 (a) and (b) are a diagram for gyrotron and a photograph of 84 GHz gyrotron which is used in the experiment. 77
4.4 Photograph of the mirrors system inside the MOU. The MOU is composed of six mirrors, and the shaped beam is coupled to the corrugated waveguide. 78
4.5 Diagram of the mirrors system inside the MOU. (a) shows the south side view and (b) shows the east side view. 78
4.6 Diagram of the transmission system. (a) shows the top view and (b) shows the side view. 83
4.7 Photograph of the transmission system. This transmission system is composed of 13 mirrors including the mirrors in the polarizer box and the vacuum chamber. This transmission system is designed so that the waist size of the beam becomes 30 mm at the center of the superconducting coil where the magnetic field strength is strongest on the optical axis. 84
4.8 Photograph of the polarizer box. This polarizer box is composed of five mirrors including two grooved surface mirrors with $\frac{\lambda}{4}$ and $\frac{\lambda}{8}$. 85
4.9 Distribution of the magnetic field strength along the optical axis. It is possible to apply a magnetic field strength of 6.5 T at the center of the torus. 85
4.10 (a): Overall photograph of the vacuum chamber. (b): Photograph taken from the top of the vacuum chamber. There are four ICF203 flanges on the top. (c): Photograph of the electron gun installed at the bottom of the vacuum chamber. Photograph of the M10 mirror. The mirror has a small hole with a diameter of 5 mm in the center, which allows electrons supplied from the electron gun to travel to the interaction region along the optical axis. Photograph of the 150 turned enamel wire used in diamagnetism measurement. This is wound with a width of 1 cm around the vacuum vessel inside the torus coil. 86

5.1 (i)Required grating mirror performance. Fundamental high power beam is to be reflected only toward +30 deg. Main power of the 2nd harmonics is to be diffracted toward -30 deg. (ii)The radiation of the frequency ω_1 is only reflected or 0th order diffracted toward +30 deg. direction without higher order diffraction by setting $d < \lambda/2$ or $k_g > 2k_0$ on the grating mirror. (iii)The main power of the radiation of the frequency ω_2 is diffracted toward -30 deg. by the slope with the blaze angle θ_B on the mirror. (iv) Many slopes are placed on the mirror in order to make the grating. Determining the line spacing so that the -1st beam can be directed toward -30 deg [1]. . 90
5.2 Relationship between the line spacing and the direction of the diffracted beam [1]. 91
5.3 Low power experimental set up: The beams which are emitted by the oscillator are reflected or diffracted by the grating mirror. These beam radiation patterns are measured by the angle scanning receiving antenna by 1 deg. Because the experimental setup is arranged so that both long sides of the antenna area and moving distance of the antenna per deg. are almost the same, the angular resolution is best [1]. 92
5.4 Angular distribution of the ω_1 and the ω_2: Intensity is represented by the radial direction and it is normalized by the maximum. Propagation directions of the reflection or diffraction beams are represented by the angle direction [1]. 93
5.5 (a): Mirror surface calculated by eq.(5.4). (b): Direction of the desired diffraction beam. (c): Definition of the grating function. 94

6.1 Definition of the normal vector on the mirror surface. 99
6.2 Experimental setup [16]: Sub-THz Imaging camera has a sensor size of 192×192 mm and 64×64 pixels, totaling 4096 pixels. The power sensitivity per pixel has 4 - 45 nW/pixel, which depends on the exposure. Frequency sensitivity also has the range from 0.02 THz (20 GHz) to 0.7 THz (700 GHz). 101
6.3 Spiral mirror with TC = +3. The origin has a singular point with indefinite z_{m} value, and then the step (at $\phi_{\mathrm{m}} = 0$) depends on TC of the vortex beam and on the injection angle [16]. 102

6.4 Intensity distributions of the millimeter wave in 154 GHz with a helical wavefront at the aperture position [16]. The left figure shows the calculated intensity distribution by eq.(6.7) with waist size 13 mm. The right figure shows the measured intensity distribution. Both figures had clear donut-shaped intensity distribution. Scale of both the vertical axis and the horizontal axis were 200 mm, and the intensity with linear scale was normalized by being maximum value 1. Next, white line with triangle on the left figure represents size of the triangular aperture. The optical axis of the vortex beam coincided with the center of gravity of the triangular aperture. Then the bright ring became slightly larger than the inscribed circle. 104
6.5 (a): Diffraction patterns by the millimeter wave with a helical wavefront with negative TC. The left row shows the calculation results. The right row shows the experimental results. Top figures show TC = −1, middle figures show the TC = −2, and bottom figures show TC = −3. Scale of both the vertical axis and the horizontal axis are 200 mm, and then the intensity is normalized by being maximum value 1. (b): Same as Fig. 4(a), but the sign of the TC is positive [16]. 105
6.6 Diffraction patterns by the Gaussian millimeter wave (this is equivalent to TC = 0). The left figure shows the calculation result. The right figure shows the experimental result. In the case of the Gaussian beam, the characteristic diffraction pattern did not appear [16]. 106
6.7 Operation principle of the heterodyne method. The input signal is down-converted by multiplying LO signal using mixer. 107
6.8 Two spatial points measurement by heterodyne system. This measurement system has OMT after antenna so that the polarization of the vortex beam can be identified. 109

List of Tables

3.1 Initial condition of the electron with cyclotron motion in static uniform magnetic field, beam parameters applied from the outside, and some parameters. 40
3.2 Initial conditions of the electron with cyclotron motion in the magnetic mirror field, beam parameters applied from the outside, and some parameters. 56

Chapter 1

Introduction

1.1 History of the Wave with an Orbital Angular Momentum and the Characteristics of the Wave

Study on the phase singularity started with the seminal work of J. Nye and M. Berry [1,2]. The phase singularity of a wave was defined as a line along which the phase of the electromagnetic field is indeterminate, that is, a line on which the intensity is zero. It is well known that a photon has a Spin Angular Momentum (SAM) and an Orbital Angular Momentum (OAM). The SAM is characterized by a polarization of waves. A right-handed polarized wave and a left-handed polarized wave have $\pm$ 1 SAM, respectively. The presence of a photon OAM was shown by Allen [3] in 1992. The paraxial solution of the wave equation in the cylindrical coordinate system shows the presence of an angular momentum that does not depend on the polarization. This is called an orbital angular momentum to distinguish from a spin angular momentum. At present, one of the waves with OAM is called the Laguerre-Gaussian (LG) beam. In particular, the LG beams with the frequency band of the visible light are called an optical vortex. It is well-known that a Hermite–Gaussian (HG) beam has a plane or spherical equiphase front, on the other hand, the equiphase front of an optical vortex or LG beam has a helical wavefront. The reason why the LG beam is called a vortex is that there is a phase term that depends on the radial direction and forms a spiral phase front. Furthermore, the optical vortex has a singular point where the phase cannot be defined on the optical axis. Then the intensity on the optical axis is defined by zero.

It is well known that the wave equation in vacuum for the field component $\boldsymbol{F}(\boldsymbol{r}, t)$ is represented by

$$\left(\nabla^2 - \frac{1}{c^2}\frac{\partial^2}{\partial t^2}\right)\boldsymbol{F}(\boldsymbol{r}, t) = 0. \tag{1.1}$$

As we can see, this equation is independent for each field component $f(\boldsymbol{r},t)$. Thus, we can rewrite the eq.(1.1) in scalar Helmholtz equation by considering $f(\boldsymbol{r},t)$ as monochromatic light $f(\boldsymbol{r},t)=u(\boldsymbol{r},t)e^{i(kz-\omega t)}$

$$\left(\nabla_T^2+2ik\frac{\partial}{\partial z}\right)f(\boldsymbol{r},t)=0 \tag{1.2}$$

where ∇_T is the transverse component of nabla operator. In addition, we used paraxial appropriation. Then, by solving eq.(1.2) in Cartesian coordinate, we can obtain HG mode as follows

$$\mathrm{HG}_{mn};\ \ f_{mn}^{HG}(\boldsymbol{r},t)=E_0\frac{\omega_0}{\omega_z}H_m\left(\frac{x\sqrt{2}}{\omega_z}\right)H_n\left(\frac{y\sqrt{2}}{\omega_z}\right)e^{\left(-\frac{x^2+y^2}{\omega_z^2}\right)}e^{\left\{\frac{k(x^2+y^2)}{2R}+\psi\right\}}e^{i(kz-\omega t)} \tag{1.3}$$

where

$$\psi=(m+n+1)\tan^{-1}\left(\frac{z}{z_R}\right), \tag{1.4}$$

while, by solving eq.(1.2) in cylindrical coordinate, we can obtain LG mode as follows

$$\begin{aligned}\mathrm{LG}_{lp};\ \ f_{lp}^{LG}(\boldsymbol{r},t)=&\sqrt{\frac{2p!}{\pi(p+|l|!)}}\frac{1}{w(z)}\left(\frac{r\sqrt{2}}{w(z)}\right)^{|l|}L_p^{|l|}\left(\frac{2r^2}{w^2(z)}\right)\\&\times e^{\frac{-r^2}{w^2(z)}}e^{\frac{-ikr^2}{2R(z)}}e^{-i(2p+|l|+1)\tan^{-1}(\frac{z}{z_R})}e^{-il\phi}e^{i(kz-\omega t)}.\end{aligned} \tag{1.5}$$

Fig.1.1 shows the phase front structure and the intensity distribution regarding HG_{00} mode and LG_{01} mode. In the phase front structure, HG_{00} mode which is Gaussian beam has plane or spherical equiphase front, while LG_{01} mode which is optical vortex has helical wavefront. In the intensity distribution, HG_{00} mode has Gaussian-shaped intensity distribution as the name suggests, while LG_{01} mode has donut-shaped intensity distribution. In addition, Fig.1.2 shows the intensity distribution regarding HG_{mn} mode and LG_{lp} mode.

Basically, an optical vortex is passively generated by using optical elements such as a spiral phase plate, a computer-generated hologram, and a q-plate as will be mentioned in the next section in detail. However, it is suggested in helical undulator radiation that radiation from a charged particle in spiral motion has a helical wavefront [4]. Studies regarding actively generated radiation with a helical wavefront without using optical elements have been started [5]. Recently, it has been theoretically and experimentally shown that radiation from a charged particle in spiral motion has a helical wavefront by Katoh *et al.* in 2017 [6,7]. From this, it becomes possible to generate a vortex beam actively. Since the frequency of an actively generated vortex beam depends on the rotation frequency of the charged particle, it becomes possible to generate a vortex beam in any waveband. The theory regarding actively generated radiation from a charged particle will be discussed in Sec.1.4.

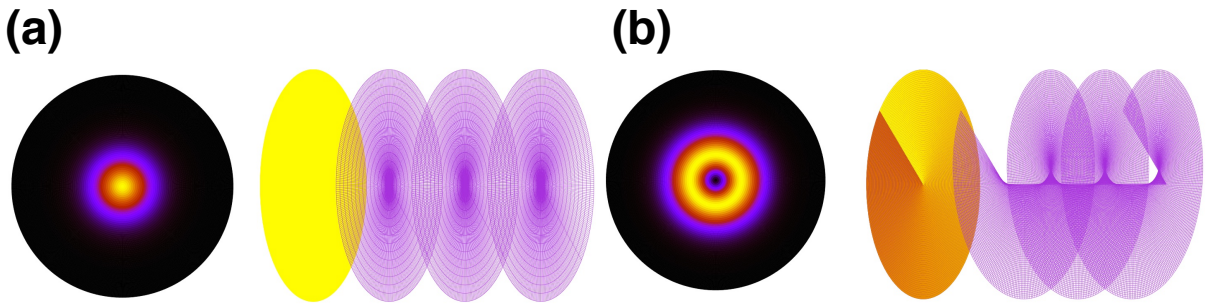

Figure 1.1: The phase front structure and the intensity distribution (a): Gaussian beam as HG_{00} mode. (b): Optical vortex as LG_{01} mode.

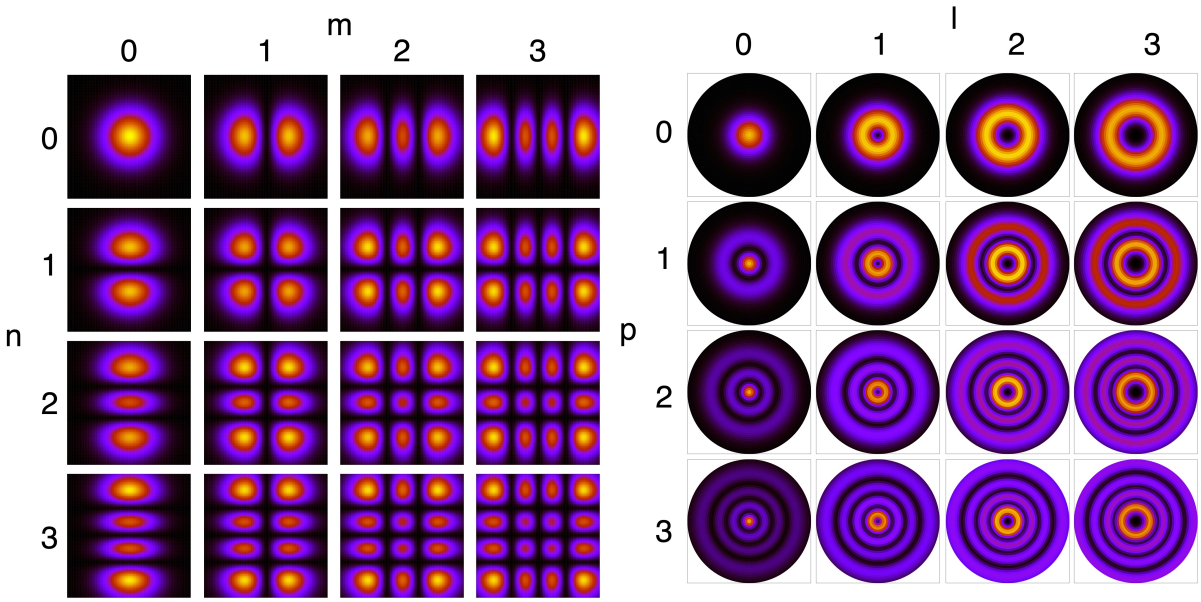

Figure 1.2: The intensity distribution regarding HG_{mn} mode and LG_{lp} mode.

1.2 How to Generate the Optical Vortex

As you will be shown below, there are two ways to make a vortex beam. One method is shown in Fig.1.3. This is a passive method using optical elements. The vortex beam is generated by passing a Gaussian beam through an optical element.

- Spiral Phase Plate:
  A spiral phase plate shown in Fig.1.3(a) is a phase plate whose thickness continuously changes in the azimuth direction, and can provide the phase difference of $2\pi n$ for the injected beam around the optical axis [8]. Here, n indicates a Topological Charge (TC).

- Computer-generated Hologram:
  A computer-generated hologram shown in Fig.1.3(b) is made based on calculation of diffraction patterns between a Gaussian beam as reference beam and the LG beam, and then the calculated diffraction patterns are drawn on the Spatial Light Modulator (SLM) [9]. Thus, when a reference beam such as Gaussian beam is injected into the hologram, the LG beam can be reproduced.

- Q-plate:
  Q-plate shown in Fig.1.3(c) is a liquid crystal plate with a TC q at its center, which can easily generate an axially symmetric polarized beam such as radial or azimuth polarized beams and an optical vortex [10, 11]. When circularly polarized beam is injected into the q-plate, an optical vortex can be generated, while a linearly polarized beam is injected, radial or azimuth polarized beams can be generated.

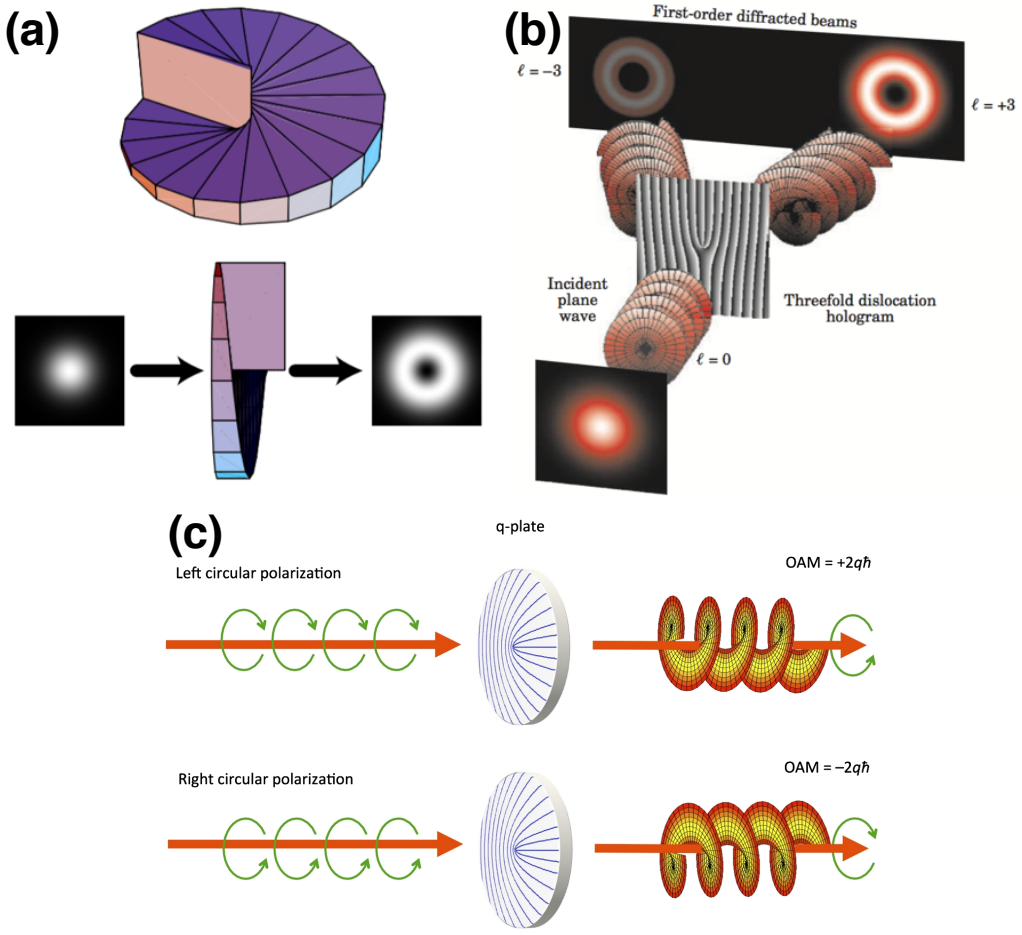

Figure 1.3: Passive methods for producing a optical vortex. (a): Spiral phase plate [8]. (b): Computer-generated hologram [9]. (c): Q-plate [11].

1.3 Application of the Optical Vortex

As mentioned, an optical vortex has a donut-shaped intensity distribution, which does not have intensity on the beam axis, and has the orbital angular momentum in addition to the spin angular momentum which depends on the polarization. Many research fields have utilized these characteristics for applications, such as nanostructure formation by matter-optical vortex interaction, the interaction between the magnetic material and an optical vortex, chemical researches of molecules with asymmetry, and telecommunication by controlling orbital angular momentum.

1.3.1 Production of Nanostructure

An optical vortex is also known as light with chirality. Chirality indicates the characteristic of molecules and materials that have mirror image, such as our right and left hands. Producing materials with chirality have been carried out by utilizing the chirality of light. Fig.1.4 shows the structure called nanoneedle produced by an optical vortex. The optical vortex has positive and negative topological charge depending on the direction of the spiral, and that indicates the chirality. By applying the optical vortex to the material, a chiral nanostructure can be created [12].

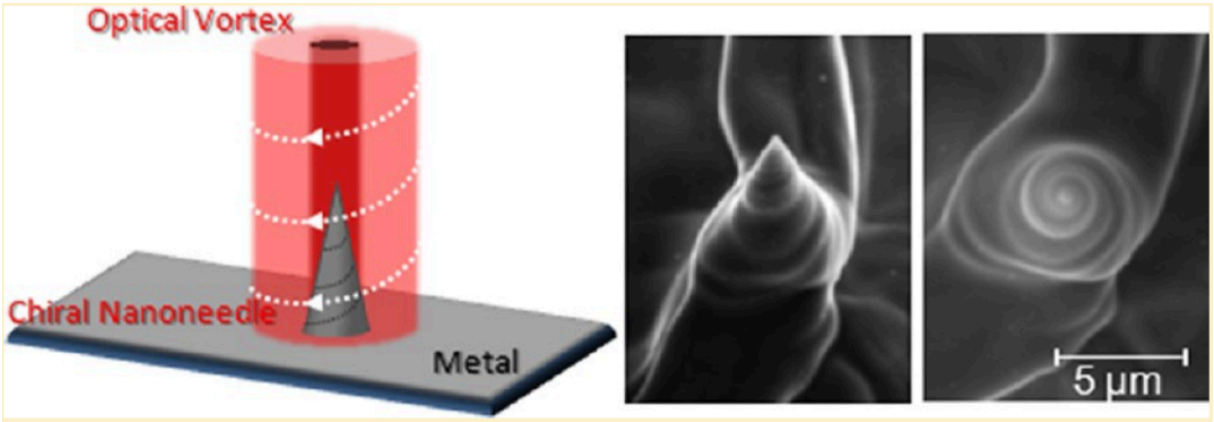

Figure 1.4: The nanoneedle produced by an optical vortex. Since the optical vortex has positive and negative topological charge depending on the direction of the spiral, a chiral nanostructure can be created [12].

1.3.2 Communication using a Vortex Beam in Millimeter Wave Regime

A vortex beam in millimeter wave regime has been actively investigated. Studies on millimeter wave with helical wavefront mainly focus on the use of the wave in telecommu-

nication [14–20]. Because it is an important issue to achieve high-capacity optical network technologies for contribution of high data traffic. Recently, Mode-Division Multiplexing (MDM) optical transmission technologies using multi-core optical fiber, which has been able to transmit high-capacity data than single-core optical fiber, have been studied. As shown in Fig.1.5, OAM of the optical vortex is considered as one of the degrees of freedom in the wave. It has been expected to achieve high-capacity telecommunication by multiplexing the topological charges. Since each optical vortex with different topological charge is orthogonal to each other, it is possible to communicate using different optical vortex which is called OAM mode-division multiplexing (OAM-MDM). The advantage using optical vortex is that the OAM- MDM can be data transmission with same frequency and it will contribute to overcome the lack of frequency assignment.

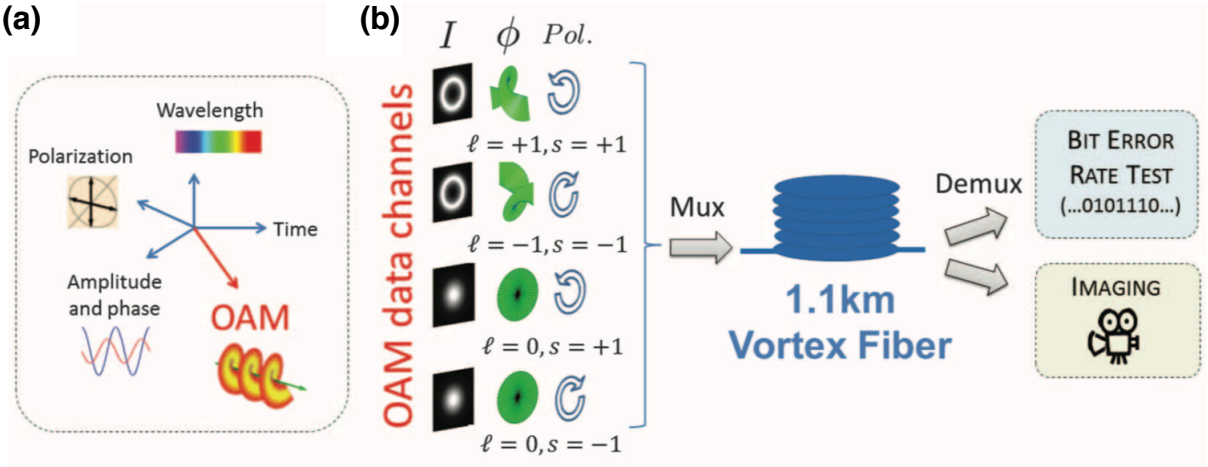

Figure 1.5: Telecommunication using optical vortex. Since each optical vortex with different topological charge is orthogonal to each other, it is possible to communicate by OAM-MDM [14].

1.4 Vortex Radiation from a Charged Particle in Spiral Motion

As mentioned above, there are two ways to make a vortex beam. The first was the passive method using optical elements as mentioned in Sec.1.2. The other is the active method theoretically derived by Katoh *et al.* [6]. They studied the radiation field created by electrons with spiral motion and theoretically showed that the higher harmonics radiation have helical wavefront as a classical phenomenon. The electromagnetic field created by an electron with an arbitrary trajectory is calculated with the Liénard-Wiechert potential

and in the case of having periodic motion, the potential can be Fourier decomposed as follows

$$\begin{aligned} \boldsymbol{A}(\boldsymbol{r},t) &= e\frac{\boldsymbol{\beta}(t_e)}{|\boldsymbol{r}-\boldsymbol{r}_e(t_e)|-(\boldsymbol{r}-\boldsymbol{r}_e(t_e))\cdot\boldsymbol{\beta}(t_e)}\Bigg|_{t_e=t-\frac{|\boldsymbol{r}-\boldsymbol{r}_e|}{c}} \\ &= \sum_{l=1}^{\infty}\tilde{\boldsymbol{A}}_l(\boldsymbol{r})e^{-il\omega t} \end{aligned} \tag{1.6}$$

where $\boldsymbol{A}(\boldsymbol{r},t)$ is vector potential; e, $\boldsymbol{\beta}$, $\boldsymbol{r}$, and $\boldsymbol{r}_e$ are electric charge, normalized velocity, position vector at observer position, and position vector at electron position; t and t_e are time at observer position and time at electron, that is retarded time. In addition, $\tilde{\boldsymbol{A}}(\boldsymbol{r},t)$ is Fourier component of vector potential and it is represented as follows

$$\tilde{\boldsymbol{A}}_l(\boldsymbol{r}) = \frac{e}{c}\frac{1}{2\pi/\omega}\frac{e^{ikr}}{r}\oint e^{il\omega(t_e-\frac{\boldsymbol{n}\cdot\boldsymbol{r}_e(t_e)}{c})}\mathrm{d}\boldsymbol{r}_e(t_e)+o\left(\frac{1}{r^2}\right) \tag{1.7}$$

Fig.1.6 shows the coordinate system in this theory. An electron has spiral motion with radius $|\boldsymbol{r}_e|$ around the origin. We consider the spherical coordinate system with unit vector $\boldsymbol{e}_r$, $\boldsymbol{e}_\theta$, and $\boldsymbol{e}_\phi$. The position vector of the electron at a given time is represented as follows

$$\boldsymbol{r}_e(t_e) = r_e(\sin\theta\sin(\omega t_e-\phi)\boldsymbol{e}_r+\cos\theta\sin(\omega t_e-\phi)\boldsymbol{e}_\theta-\cos(\omega t_e-\phi)\boldsymbol{e}_\phi). \tag{1.8}$$

By substituting the trajectory information into the Fourier component of vector potential, the radiation field with the helical wavefront can be calculated. Finally, we can obtain the equation below

$$\boldsymbol{E} = \frac{1}{4\pi\varepsilon_0}\frac{e}{c}l\omega\frac{e^{i(kr-l\omega t)}}{r}\left\{\varepsilon_+e^{i(l-1)\phi}\boldsymbol{e}_+ +\varepsilon_-e^{i(l+1)\phi}\boldsymbol{e}_- -i\varepsilon_z e^{il\phi}\boldsymbol{e}_z\right\}, \tag{1.9}$$

where

$$\varepsilon_\pm = \pm\frac{\cos^2\theta}{\sin\theta}J_l(l\beta\sin\theta)+\beta J_l'(l\beta\sin\theta), \tag{1.10}$$

$$\varepsilon_z = \cos\theta J_l(l\beta\sin\theta), \tag{1.11}$$

$$\boldsymbol{e}_+ = \frac{\boldsymbol{e}_x+i\boldsymbol{e}_y}{\sqrt{2}}, \quad \boldsymbol{e}_- = \frac{\boldsymbol{e}_x-i\boldsymbol{e}_y}{\sqrt{2}}. \tag{1.12}$$

Here, J_l and J_l' are a Bessel function of the first kind and its derivative, respectively. $\boldsymbol{e}_+$ and $\boldsymbol{e}_-$ are rotation unit vectors on the x-y plane, respectively. It should be noted

that the phase term with respect to ϕ is added in the eq.(1.9). This expression explicitly shows that the phase term is dependent on the azimuthal angle. Since ϕ represents the azimuthal angle of the position of the observer, eq.(1.9) has spatial phase structure. This is a characteristic of a beam with a helical wavefront. The helical wavefront arises at only 2nd and higher harmonics, and the radiation is circularly polarized (see Fig.1.7).

When hearing the word "vortex," a phenomenon with a spiral pattern is usually imagined. However, in general, a wave with helical wavefront is a wave that has the following two characteristics. 1): There is a phase term depending on the azimuthal angle, and the phase is characterized by an integer called a Topological Charge (TC). 2): The intensity distribution is donut-shaped with no intensity peak on the optical axis. Although it is difficult to imagine the spiral pattern from these characteristics, the phase structure of the cross section of the beam has vortex structure. For example, by creating the interference patterns between the wave with helical wavefront and the wave without helical wavefront, the spiral pattern can be visualized. The interference patterns are shown in Fig.1.8. Therefore, the word "vortex" is commonly used.

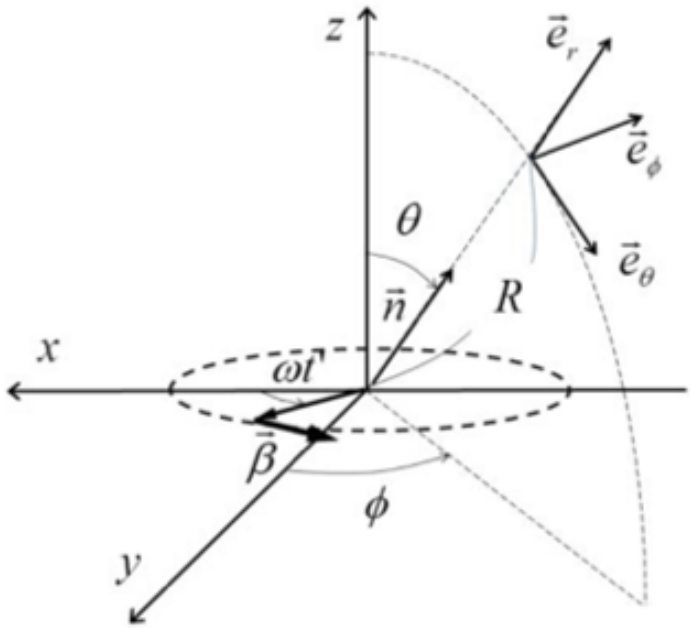

Figure 1.6: The coordinate system for deriving the radiation theory where an electron with spiral motion produces electromagnetic field with helical wavefront actively [7].

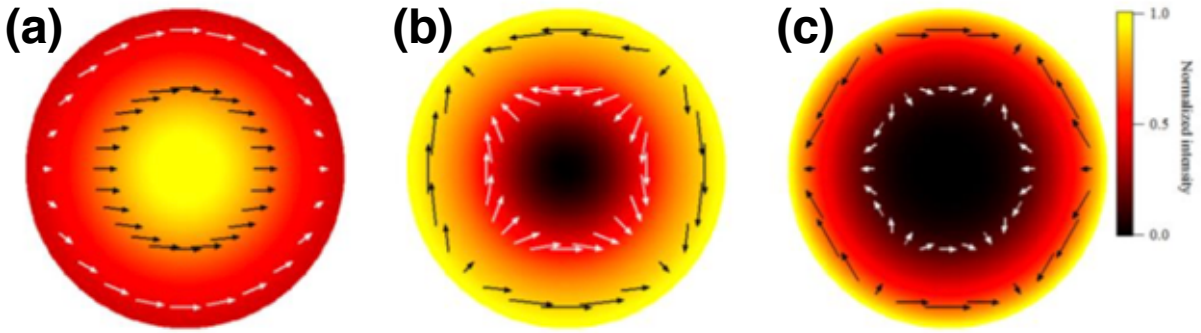

Figure 1.7: The intensity distribution and the direction of the electric fields at a given time [7]. (a): fundamental radiation, (b): second harmonic radiation, and (c): third harmonic radiation.

1.5 Progress of the Wavelength Spectrum regarding Actively Generated Vortex Beams

A vortex beam can be easily produced by passive methods at visible frequency. But at other frequencies, it is difficult to produce an optical vortex due to restrictions of the optical elements. However, if we can control the electron motion, we can obtain any waveband of vortex beam.

Historically, Sasaki *et al.* was theoretically suggested for the first time in helical undulator radiation that radiation from a charged particle in spiral motion may have a helical wavefront. The experimental demonstration was carried out at a synchrotron radiation facility in Germany in 2008 [4,5]. The results showed that the radiation from an electron with spiral motion in the helical undulator has helical wavefront. However, these results were not sufficient to show the characteristics of vortex beam. Recently, it has been theoretically and experimentally shown by Katoh *et al.* that radiation from a charged particle in spiral motion has a helical wavefront [6, 7]. From this, it becomes possible to generate a vortex beam actively. Studies regarding actively generated radiation with a helical wavefront without using optical elements have been started. Since the frequency of an actively generated vortex beam depends on the rotation frequency of the charged particle, it becomes possible to generate a vortex beam in any wave band. Therefore, actively generated vortex beams have been studied in several frequency bands such as gamma ray, x-ray, and ultraviolet, which are high-energy vortex beams because limitation of the optical elements no longer exists. Katoh *et al.* experimentally demonstrated for the first time that the radiation from high-energy electron with spiral motion in helical undulator has a helical wavefront at the UVSOR synchrotron facility (Fig.1.8) [7]. They succeeded in obtaining the characteristic diffraction patterns by passing the radiation from the helical undulator through the double-slit. In addition, they have succeeded

in measuring spiral interfering patterns by interfering with the fundamental radiation without helical wavefront and the second harmonic radiation with helical wavefront. In addition, Taira *et al.* theoretically deduced the method to generate γ-ray with helical wavefront(Fig.1.9) [21, 22]. γ-ray with helical wavefront is generated by laser Compton scattering. When the laser used for the laser Compton scattering is circularly polarized, the scattered photons by high-energy electron produce the γ-ray with helical wavefront.

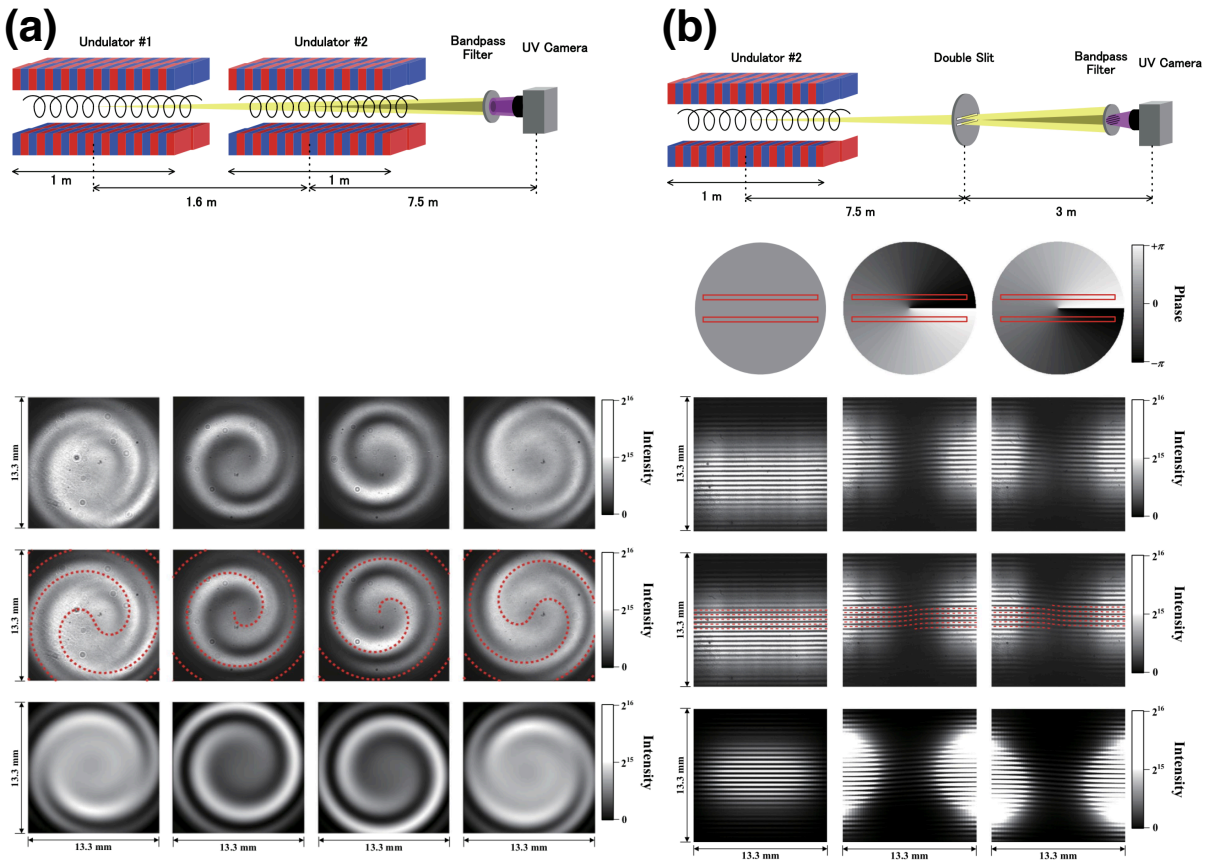

Figure 1.8: The experimental results at the UVSOR synchrotron facility. For the first time, it has been demonstrated that the radiation from high-energy electron with spiral motion in helical undulator has a helical wavefront [7].

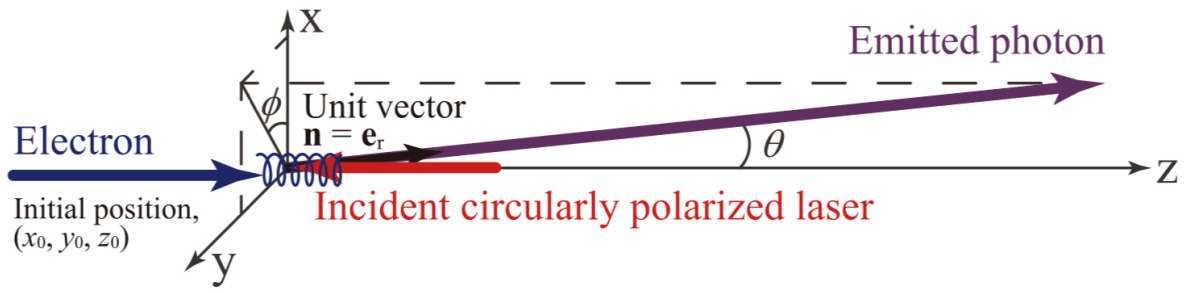

Figure 1.9: The method to generate γ-ray with helical wavefront. When the laser used for the laser Compton scattering is circularly polarized, the scattered photons by high-energy electron produce the γ-ray with helical wavefront [21].

1.6 Purpose of the Research

The radiation with helical wavefront in shorter wavelength regime such as extreme ultraviolet and γ-ray have been actively studied. However, the studies of active radiation with helical wavefront in the longer wavelength regime such as millimeter-wave have not been reported yet. This is because the measurement focusing on the helical wavefront has never been carried out. In addition, the phase of the ECE from the multi-electron system is usually cancelled out due to the random rotation phase of each electron. In the longer wavelength regime, passively generated vortex beam has been reported such as using spiral mirrors, spiral phase plates, and radiation from the gyrotron with whispering gallery mode described in the next section.

Given this, in this study, we will carry out comprehensive researches in order to experimentally demonstrate ECE with helical wavefront in the millimeter-wave regime. Since cyclotron motion is also a type of spiral motion, Electron Cyclotron Emission, or ECE, should also have vortex properties. In addition, an ECE is a common phenomenon in nature. For example, it is found in the interaction between the solar wind and the magnetosphere, the magnetic reconnection in solar flare, and the radiation from a magnetic confinement fusion plasma. Studying the ECE with helical wavefront greatly contributes to underatanding the physics of the origin of the radiation as well.

In order to demonstrate the ECE with helical wavefront, we designed and developed an experimental device that generates the ECE with helical wavefront in multi-electron system. In this experiment, we attempt to control the rotation phase of electrons with cyclotron motion by externally applied circularly polarized wave so that the coherent radiation can be generated. This experiment is equivalent to the principle of Electron Cyclotron Resonance Heating (ECRH) in fusion plasma. In the fusion plasma, the ECRH plays an important role to produce and maintain the high temperature plasma electron. Then, electrons in the plasma are in the state where the rotation phase of each electron

is locally controlled by externally applied electromagnetic wave. And then, such electrons produce the coherent ECE with helical wavefront as well. By thermalizing the resonantly accelerated electrons, that are being randomized for the rotation phase of each electron, the helical wavefront of ECE should be cancelled out. Therefore, time scale of appearance and disappearance for the helical wavefront provides an indication of the coherent acceleration and the thermalization of the electrons. In this basic experiment, producing a group of electrons with as coherent gyro-phase as possible and measuring of ECE in millimeter-wave regime with helical wavefront greatly contribute to the understanding of plasma heating physics in fusion research.

1.6.1 Electron Cyclotron Emission

Cyclotron radiation is one of the radiation mechanisms from a charged particle which is affected by Lorentz force in the magnetic field. When the charged particle is an electron, this motion is called an electron cyclotron motion, and the electron emits an electromagnetic field whose frequency is proportional to the magnetic field strength. This is, specially, called an Electron Cyclotron Emission (ECE). The electron cyclotron frequency ω_{ce} is represented as follows

$$\omega_{\mathrm{ce}} = \frac{|e|B}{m_e} \tag{1.13}$$

where e, B, and m_e are elementary charge, magnetic field strength, and electron rest mass. In addition, the cyclotron radiation which is found in nature or fusion plasma is low power radiation, but ECE with helical wavefront can be obtained. Because producing the helical wavefront does not depend on relativistic effect. Retardation effect is a primary factor for producing the helical wavefront.

1.7 Vortex Radiation from the Gyrotron

In recent years, Sawant *et al.* have reported vortex radiation from the gyrotron [23]. The gyrotron is a cyclotron maser in millimater-wave regime which utilizes electron cyclotron emission in the cavity. However, note that the reported radiation from the gyrotron is not active radiation from the electron cyclotron motion. The radiation obtained in the study is radiation from a waveguide where a whispering gallery mode is excited as shown in Fig.1.10. Considering geometrical optics, this mode is cyclotron radiation propagates through a cylindrical cavity like a spiral stage. As a result, the whispering gallery mode makes radiation with helical wavefront.

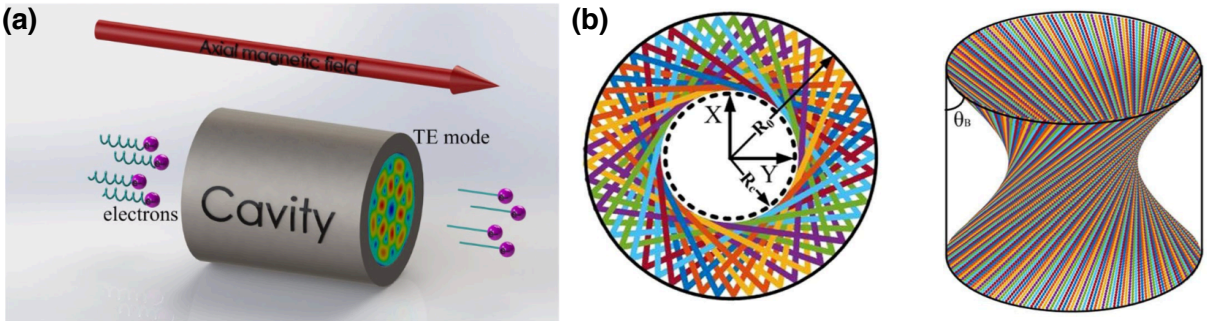

Figure 1.10: The radiation with helical wavefront from the gyrotron cavity in millimeter-wave regime. The vortex radiation is produced by the whispering gallery mode [23].

1.8 Composition of this Dissertation

This dissertation is composed of seven chapters. In Chap. 2, the basic theory of electromagnetism and theory of radiation with helical wavefront is briefly described. In Chap. 3, calculation results of ECE with helical wavefront in case static magnetic field and magnetic mirror field are discussed. In Chap. 4, experimental devices for demonstrating ECE with helical wavefront are discussed. In Chap. 5, development of the grating mirror for separating fundamental radiation without helical wavefront into second harmonic radiation with helical wavefront are discussed. In Chap. 6, development of the measurement system for vortex beam using a triangular aperture is discussed. The summary of this research is provided in Chap. 7.

Bibliography

[1] J. F. Nye and M. V. Berry, "Dislocations in Wave Trains," Proc. Royal Soc. A **336**, 165–190 (1974).

[2] G. Vallone, A. Sponselli, V. D'ambrosio, L. Marrucci, F. Sciarrino, and P. Villoresi, "Birth and evolution of an optical vortex," Opt. Lett., **24**, 15 (2016).

[3] L. Allen, M. W. Beijersbergen, R. J. C. Spreeuw, and J. P. Woerdman, "Orbital angular momentum of light and the transformation of Laguerre-Gaussiean laser modes," Phys. Rev. A, **45**, 8185 (1992).

[4] S. Sasaki and I. McNulty, "Proposal for Generating Brilliant X-Ray Beams Carrying Orbital Angular Momentum," Phys. Rev. Lett., **100**, 124801 (2008).

[5] J. Bahrdt, K. Holdack, P. Kuske, R. Muller, M. Scheer, and P. Schmid, "First Observation of Photons Carrying Orbital Angular Momentum in Undulator Radiation," Phys. Rev. Lett., **111**, 034801 (2013).

[6] M. Katoh, M. Fujimoto, H. Kawaguchi, K. Tsuchiya, K. Ohmi, T. Kaneyasu, Y. Taira, M. Hosaka, A. Mochihashi, and Y. Takashima, "Angular Momentum of Twisted Radiation from an Electron in Spiral Motion," Phys. Rev. Lett., **118**, 094801 (2017).

[7] M. Katoh, M. Fujimoto, N. S. Mirian, T. Konomi, Y. Taira, T. Kaneyasu, M. Hosaka, N. Yamamoto, A. Mochihashi, Y. Takahashi, K. Kuroda, A. Miyamoto, K. Miyamoto, and S. Sasaki, "Helical Phase Structure of Radiation from an Electron in Circular Motion," Sci. Rep., **7**, 6130 (2017).

[8] J. Courtial and K. O'Holleran, "Experiments with twisted light," Eur. Phys. J. Special Topics **145**, 35-47 (2007).

[9] M. Padgett, J. Courtial, L. Allen, "Light's Orbital Angular Momentum," Phys. Today, 57(5), 35-40, (2004).

[10] L. Marrucci, C. Manzo, and D. Paparo, "Optical Spin-to-Orbital Angular Momentum Conversion in Inhomogeneous Anisotropic Media," Phys. Rev. Lett., **96**, 163905 (2006).

[11] L. Marrucci, "The q-plate and its future," J. Nanophotonics, **7**, 078598 (2013).

[12] K. Toyoda, K. Miyamoto, N. Aoki, R. Morita, and T. Metal, "Using Optical Vortex To Control the Chirality of Twisted Metal Nanostructures," Nano Lett. **12**, 3645-3649 (2012).

[13] Y. Yan, G. Xie, M. P.J. Lavery, H. Huang, N. Ahmed, C. Bao, Y. Ren, Y. Cao, L. Li, Z. Zhao, A. F. Molisch, M. Tur, M. J. Padgett, and A. E. Willner, "High-capacity millimetre-wave communications with orbital angular momentum multiplexing," Nat. Commun., **5**, 4876, (2014).

[14] N. Bozinovic, Y. Yue, Y. Ren, M. Tur, P. Kristensen, H. Huang, A. E. Willner, and S. Ramachandran, "Terabit-Scale Orbital Angular Momentum Mode Division Multiplexing in Fibers," Science, **340**, 4876, (2013).

[15] X. Hui, S. Zheng, Y. Chen, Y. Hu, X. Jin, H. Chi, and X. Zhang, "Multiplexed Millimeter Wave Communication with Dual Orbital Angular Momentum (OAM) Mode Antennas," Sci. Rep., **5**, 10148, (2015).

[16] S. Yu, L. Li, and G. Shi, "Dual-polarization and dual-mode orbital angular momentum radio vortex beam generated by using reflective metasurface," Appl. Phys. Express, **9**, 082202, (2016).

[17] S. Yu, L. Li, G. Shi, C. Zhu, and Y. Shi, "Generating multiple orbital angular momentum vortex beams using a metasurface in radio frequency domain," Appl. Phys. Lett., **108**, 241901, (2016).

[18] H. Wu, J. Tang, Z. Yu, J. Yi, S. Chen, J. Xiao, C. Zhao, Y. Li, L. Chena, and S. Wen, "Electrically optical phase controlling for millimeter wave orbital angular momentum multi-modulation communication," Opt. Commun., **393**, 49-55 (2017).

[19] F. Tamburini, E. Mari, B. Thidé, C. Barbieri, and F. Romanato, "Experimental verification of photon angular momentum and vorticity with radio techniques," Appl. Phys. Express, **99**, 204102, (2011).

[20] A, E. Willner, Y. Ren, G. Xie, Y. Yan, L. Li, Z. Zhao, J. Wang, M. Tur, A. F. Molisch, and S. Ashrafi, "Recent advances in high-capacity free-space optical and radio-frequency communications using orbital angular momentum multiplexing," Phil. Trans. R. Soc. A, **375**, 20150439, (2017).

[21] Y. Taira, T. Hayakawa, and M. Katoh, "Gamma-ray vortices from nonlinear inverse Thomson scattering of circularly polarized light," Sci. Rep., **7**, 5018 (2017).

[22] Y. Taira and M. Katoh, "Generation of Optical Vortices by Nonlinear Inverse Thomson Scattering at Arbitrary Angle Interactions," Astrophys. J., **860**, 11 (2018).

[23] A. Sawant, M. S. Choe, M. Thumm, and E. Choi, "Orbital Angular Momentum (OAM) of Rotating Modes Driven by Electrons in Electron Cyclotron Masers," Sci. Rep., **7**, 3372 (2017).

Chapter 2

Basic Theory

2.1 Charged Particle Motion

2.1.1 Cyclotron Motion in the Externally Applied Electromagnetic Field

The relativistic equation of motion regarding a charged particle in the electromagnetic field is represented by [1]:

$$\begin{aligned} \frac{\mathrm{d}\{\gamma m_q \boldsymbol{v}(t)\}}{\mathrm{d}t} &= q\{\boldsymbol{E}_{\mathrm{in}}(\boldsymbol{r},t) + \boldsymbol{v}(t) \times (\boldsymbol{B}_{\mathrm{in}}(\boldsymbol{r},t) + \boldsymbol{B}_{\mathrm{ex}})\} \\ &= \boldsymbol{F}_{\boldsymbol{E}_{\mathrm{in}}} + \boldsymbol{F}_{\boldsymbol{B}_{\mathrm{in}}} + \boldsymbol{F}_{\boldsymbol{B}_{\mathrm{ex}}} \end{aligned} \tag{2.1}$$

where m_q, $\boldsymbol{v}(t)$, and q are represented by the rest mass of a charged particle, the velocity of the charged particle, and the elementary charge, respectively. $\boldsymbol{B}_{\mathrm{ex}}$ is the static external magnetic field. In addition, the $\boldsymbol{E}_{\mathrm{in}}(\boldsymbol{r},t)$ and $\boldsymbol{B}_{\mathrm{in}}(\boldsymbol{r},t)$ are the electromagnetic fields applied from outside to the charged particle. Lorentz force is defined as $\boldsymbol{F}_{\boldsymbol{E}_{\mathrm{in}}}$, $\boldsymbol{F}_{\boldsymbol{B}_{\mathrm{in}}}$, and $\boldsymbol{F}_{\boldsymbol{B}_{\mathrm{ex}}}$ on the last equal sign below,

$$\boldsymbol{F}_{\boldsymbol{E}_{\mathrm{in}}} \equiv q\boldsymbol{E}_{\mathrm{in}}(\boldsymbol{r},t) \tag{2.2}$$

$$\boldsymbol{F}_{\boldsymbol{B}_{\mathrm{in}}} \equiv q\boldsymbol{v}(t) \times \boldsymbol{B}_{\mathrm{in}}(\boldsymbol{r},t) \tag{2.3}$$

$$\boldsymbol{F}_{\boldsymbol{B}_{\mathrm{ex}}} \equiv q\boldsymbol{v}(t) \times \boldsymbol{B}_{\mathrm{ex}}(\boldsymbol{r}). \tag{2.4}$$

The γ is the relativistic factor as follows:

$$\gamma \equiv \frac{1}{\sqrt{1 - |\boldsymbol{\beta}|^2}} \tag{2.5}$$

where the beta is velocity normalized to the speed of light c defined by

$$\boldsymbol{\beta} \equiv \frac{\boldsymbol{v}(t)}{c} \tag{2.6}$$

Although the γ and the $\boldsymbol{\beta}$ are dependent on time, we have omitted the variable for simplification. From now, we will expand and deform the LHS of eq.(2.1), $\boldsymbol{F}_{\boldsymbol{E}_{\rm in}}$, $\boldsymbol{F}_{\boldsymbol{B}_{\rm in}}$, and $\boldsymbol{F}_{\boldsymbol{B}_{\rm ex}}$.

(i) LHS of eq.(2.1)
By expanding the left side of eq.(2.1), we can obtain

$$\frac{\mathrm{d}\{\gamma m_q \boldsymbol{v}(t)\}}{\mathrm{d}t} = \gamma m_q c \left(\boldsymbol{I} + \gamma^2(\boldsymbol{\beta}\otimes\boldsymbol{\beta})\right)\cdot\dot{\boldsymbol{\beta}} \tag{2.7}$$

where $\dot{\boldsymbol{\beta}}$ and $\boldsymbol{I}$ are the acceleration of the normalized velocity and the unit matrix. In addition, the symbol $\otimes$ means dyadic, which is defined by using two vectors $\boldsymbol{A} = (A_x, A_y, A_z)$ and $\boldsymbol{B} = (B_x, B_y, B_z)$ as follows

$$\boldsymbol{A}\otimes\boldsymbol{B} \equiv \begin{pmatrix} A_xB_x & A_xB_y & A_xB_z \\ A_yB_x & A_yB_y & A_yB_z \\ A_zB_x & A_zB_y & A_zB_z \end{pmatrix}. \tag{2.8}$$

Also we use the identity below to obtain the relationship eq.(2.7),

$$(\boldsymbol{\beta}\cdot\dot{\boldsymbol{\beta}})\boldsymbol{\beta} = (\boldsymbol{\beta}\otimes\boldsymbol{\beta})\cdot\dot{\boldsymbol{\beta}}. \tag{2.9}$$

(ii) $\boldsymbol{F}_{\boldsymbol{E}_{\rm in}}$
We can rewrite by using unit matrix $\boldsymbol{I}$ below

$$\boldsymbol{F}_{\boldsymbol{E}_{\rm in}} = q\boldsymbol{I}\cdot\boldsymbol{E}_{\rm in}(\boldsymbol{r},t). \tag{2.10}$$

(iii) $\boldsymbol{F}_{\boldsymbol{B}_{\rm in}}$
In Maxwell's equations for the curl of an electric field, $\boldsymbol{E}_{\rm in}(\boldsymbol{r},t)$ and $\boldsymbol{B}_{\rm in}(\boldsymbol{r},t)$ are related to each other,

$$\nabla\times\boldsymbol{E}_{\rm in}(\boldsymbol{r},t) = -\frac{\partial\boldsymbol{B}_{\rm in}(\boldsymbol{r},t)}{\partial \mathrm{t}}. \tag{2.11}$$

Fourier transformation regarding $\boldsymbol{E}_{\rm in}(\boldsymbol{r},t)$ and $\boldsymbol{B}_{\rm in}(\boldsymbol{r},t)$ are represented by

$$\boldsymbol{E}_{\rm in}(\boldsymbol{r},t) = \frac{1}{(2\pi)^3}\int_{-\infty}^{\infty}\mathrm{d}\boldsymbol{k}\tilde{\boldsymbol{E}}_{\rm in}(\boldsymbol{k},t)e^{i(\boldsymbol{k}\cdot\boldsymbol{r}-\omega_{\boldsymbol{k}}t)} \tag{2.12}$$

$$\boldsymbol{B}_{\rm in}(\boldsymbol{r},t) = \frac{1}{(2\pi)^3}\int_{-\infty}^{\infty}\mathrm{d}\boldsymbol{k}\tilde{\boldsymbol{B}}_{\rm in}(\boldsymbol{k},t)e^{i(\boldsymbol{k}\cdot\boldsymbol{r}-\omega_{\boldsymbol{k}}t)}. \tag{2.13}$$

By substituting eq.(2.12) and eq.(2.13) into eq.(2.11), we can obtain the relationship of Fourier component between $\tilde{\boldsymbol{E}}_{\rm in}(\boldsymbol{k},t)$ and $\tilde{\boldsymbol{B}}_{\rm in}(\boldsymbol{k},t)$ as follows,

$$\tilde{\boldsymbol{B}}_{\rm in}(\boldsymbol{k},t) = \frac{\boldsymbol{k}}{\omega_{\boldsymbol{k}}} \times \tilde{\boldsymbol{E}}_{\rm in}(\boldsymbol{k},t). \tag{2.14}$$

Furthermore, by substituting eq.(2.13) with eq.(2.14) into eq.(2.3), $\boldsymbol{F}_{\boldsymbol{B}_{\rm in}}$ is deformed as follows,

$$\begin{aligned} \boldsymbol{F}_{\boldsymbol{B}_{\rm in}} &= \boldsymbol{v}(t) \times \frac{q}{(2\pi)^3} \int_{-\infty}^{\infty} {\rm d}\boldsymbol{k} \frac{\boldsymbol{k}}{\omega_{\boldsymbol{k}}} \times \tilde{\boldsymbol{E}}_{\rm in}(\boldsymbol{k},t) e^{i(\boldsymbol{k}\cdot\boldsymbol{r}-\omega_{\boldsymbol{k}}t)} \\ &= q\boldsymbol{v}(t) \times \frac{\boldsymbol{n}}{c} \times \boldsymbol{E}_{\rm in}(\boldsymbol{k},t) \end{aligned} \tag{2.15}$$

where $\boldsymbol{n}$ is the unit vector with $(0,0,1)$. That is, $\boldsymbol{n}$ represents the propagation direction for the electromagnetic wave with the relationship below,

$$\boldsymbol{k} = \frac{\omega_{\boldsymbol{k}}}{c}\boldsymbol{n}. \tag{2.16}$$

Furthermore, eq.(2.15) is rewritten with an inner product of $\tilde{\boldsymbol{E}}_{\rm in}(\boldsymbol{k},t)$ by vector identity

$$\begin{aligned} \boldsymbol{v}(t) \times \frac{\boldsymbol{n}}{c} \times \boldsymbol{E}_{\rm in}(\boldsymbol{r},t) &= (\boldsymbol{n} \otimes \boldsymbol{\beta}) \cdot \boldsymbol{E}_{\rm in}(\boldsymbol{r},t) \\ &\quad -((\boldsymbol{n}\cdot\boldsymbol{\beta})\boldsymbol{I}) \cdot \boldsymbol{E}_{\rm in}(\boldsymbol{r},t) \end{aligned} \tag{2.17}$$

that is,

$$\boldsymbol{F}_{\boldsymbol{B}_{\rm in}} = ((-\boldsymbol{\beta}\cdot\boldsymbol{n})\boldsymbol{I} + \boldsymbol{n} \otimes \boldsymbol{\beta}) \cdot \boldsymbol{E}_{\rm in}. \tag{2.18}$$

(iv) $\boldsymbol{F}_{\boldsymbol{B}_{\rm ex}}$

We can rewrite as follows,

$$\boldsymbol{F}_{\boldsymbol{B}_{\rm ex}} = \frac{|q|}{q} m_q c \omega_{\rm cq} (\boldsymbol{\beta} \times \hat{\boldsymbol{b}}_{\rm n}) \tag{2.19}$$

where we normalized the magnetic field by $B_{\rm max}$, which is the magnetic field strength at the origin, as follows,

$$\boldsymbol{B}_{\rm ex}(\boldsymbol{r}) = B_{\rm max}\hat{\boldsymbol{b}}_{\rm n}(\boldsymbol{r}) \tag{2.20}$$

with

$$\hat{\boldsymbol{b}}_{\rm n}(\boldsymbol{r}) \equiv \left(\frac{B_x(\boldsymbol{r})}{B_{\rm max}}, \frac{B_y(\boldsymbol{r})}{B_{\rm max}}, \frac{B_z(\boldsymbol{r})}{B_{\rm max}} \right). \tag{2.21}$$

And the cyclotron angular frequency is defined by

$$\omega_{\rm cq} \equiv \frac{|q| B_{\rm max}}{m_q}. \tag{2.22}$$

By substituting eq.(2.7), eq.(2.10), eq.(2.18), and eq.(2.19) into eq.(2.1), and multiplying the inverse matrix for $(\boldsymbol{I} + \gamma^2(\boldsymbol{\beta} \otimes \boldsymbol{\beta}))$ by both sides, we can obtain

$$\begin{aligned} \dot{\boldsymbol{\beta}} = \frac{q}{m_q c \gamma} \left(\boldsymbol{I} + \gamma^2(\boldsymbol{\beta} \otimes \boldsymbol{\beta}) \right)^{-1} \cdot ((1 - \boldsymbol{\beta} \cdot \boldsymbol{n})\boldsymbol{I} + \boldsymbol{n} \otimes \boldsymbol{\beta}) \cdot \boldsymbol{E}_{\rm in} \\ + \left(\boldsymbol{I} + \gamma^2(\boldsymbol{\beta} \otimes \boldsymbol{\beta}) \right)^{-1} \cdot \frac{|q|}{q} \frac{\omega_{\rm cq}}{\gamma} (\boldsymbol{\beta} \times \hat{\boldsymbol{b}}_{\boldsymbol{n}}). \end{aligned} \tag{2.23}$$

The inverse matrix is solved by cofactor expansion, therefore

$$\left(\boldsymbol{I} + \gamma^2(\boldsymbol{\beta} \otimes \boldsymbol{\beta}) \right)^{-1} = \boldsymbol{I} - \boldsymbol{\beta} \otimes \boldsymbol{\beta}. \tag{2.24}$$

Furthermore, the second term of eq.(2.23) is calculated by

$$(\boldsymbol{I} - \boldsymbol{\beta} \otimes \boldsymbol{\beta}) \cdot (\boldsymbol{\beta} \times \hat{\boldsymbol{b}}_{\boldsymbol{n}}) = \boldsymbol{\beta} \times \hat{\boldsymbol{b}}_{\boldsymbol{n}}. \tag{2.25}$$

Therefore, the motion of the charged particle is represented by the relativistic equation of motion as follows

$$\dot{\boldsymbol{\beta}} = \frac{q}{m_q c \gamma} (\boldsymbol{I} - \boldsymbol{\beta} \otimes \boldsymbol{\beta}) ((1 - \boldsymbol{\beta} \cdot \boldsymbol{n})\boldsymbol{I} + \boldsymbol{n} \otimes \boldsymbol{\beta}) \cdot \boldsymbol{E}_{\rm in} + \frac{|q|}{q} \frac{\omega_{\rm cq}}{\gamma} (\boldsymbol{\beta} \times \hat{\boldsymbol{b}}_{\rm n}). \tag{2.26}$$

This equation shows that if the external electric field satisfies with $\boldsymbol{E}_{\rm in} = 0$, this equation represents pure cyclotron motion. The orbit is distorted by the external electric field. When the static magnetic field $\boldsymbol{B}_{\rm ex} = (0, 0, B_{\rm ex})$ is applied and the charged particle is an electron, eq.(2.26) becomes

$$\dot{\boldsymbol{\beta}} = \frac{-e}{m_q e \gamma} (\boldsymbol{I} - \boldsymbol{\beta} \otimes \boldsymbol{\beta}) ((1 - \boldsymbol{\beta} \cdot \boldsymbol{n})\boldsymbol{I} + \boldsymbol{n} \otimes \boldsymbol{\beta}) \cdot \boldsymbol{E}_{\rm in} - \frac{\omega_{\rm ce}}{\gamma} (\boldsymbol{\beta} \times \hat{\boldsymbol{e}}_z) \tag{2.27}$$

where the $\hat{\boldsymbol{e}}_z$ indicates the unit vector along the z-direction.

2.2 Radiation Theory

2.2.1 Maxwell's Equation

Maxwell's equations are the fundamental equations for describing the electromagnetic field,

$$\nabla \times \boldsymbol{E}(\boldsymbol{r},t) = -\frac{\partial \boldsymbol{B}(\boldsymbol{r},t)}{\partial t} \tag{2.28}$$

$$\nabla \times \boldsymbol{H}(\boldsymbol{r},t) = \boldsymbol{j}(\boldsymbol{r},t) + \frac{\partial \boldsymbol{D}(\boldsymbol{r},t)}{\partial t} \tag{2.29}$$

$$\nabla \cdot \boldsymbol{D}(\boldsymbol{r},t) = \rho(\boldsymbol{r},t) \tag{2.30}$$

$$\nabla \cdot \boldsymbol{B}(\boldsymbol{r},t) = 0 \tag{2.31}$$

where $\boldsymbol{E}(\boldsymbol{r},t)$, $\boldsymbol{D}(\boldsymbol{r},t)$, $\boldsymbol{H}(\boldsymbol{r},t)$, and $\boldsymbol{B}(\boldsymbol{r},t)$ are electric field, electric flux, magnetic field, and magnetic field flux, respectively. $\rho(\boldsymbol{r},t)$ and $\boldsymbol{j}(\boldsymbol{r},t)$ are charge density and current density. In this chapter, since we also treat an electromagnetic wave in a vacuum, set $\rho(\boldsymbol{r},t)$ and $\boldsymbol{j}(\boldsymbol{r},t)$ to 0. Then,

$$\nabla \times \boldsymbol{E}(\boldsymbol{r},t) = -\frac{\partial \boldsymbol{B}(\boldsymbol{r},t)}{\partial t} \tag{2.32}$$

$$\nabla \times \boldsymbol{B}(\boldsymbol{r},t) = \varepsilon_0 \mu_0 \frac{\partial \boldsymbol{E}(\boldsymbol{r},t)}{\partial t} \tag{2.33}$$

$$\nabla \cdot \boldsymbol{E}(\boldsymbol{r},t) = 0 \tag{2.34}$$

$$\nabla \cdot \boldsymbol{B}(\boldsymbol{r},t) = 0 \tag{2.35}$$

where ε_0 and μ_0 are the permittivity of the vacuum and the permeability of the vacuum. Here we used the relationship below:

$$\boldsymbol{D}(\boldsymbol{r},t) = \varepsilon_0 \boldsymbol{E}(\boldsymbol{r},t) \tag{2.36}$$

$$\boldsymbol{B}(\boldsymbol{r},t) = \mu_0 \boldsymbol{H}(\boldsymbol{r},t). \tag{2.37}$$

Hereafter, we refer to $\boldsymbol{B}(\boldsymbol{r},t)$ as "magnetic field" for convenience. By Maxwell's equations in a vacuum, the wave equation for electric field and the magnetic field are given below.

$$\nabla^2 \boldsymbol{E}(\boldsymbol{r},t) = \frac{1}{c^2}\frac{\partial^2 \boldsymbol{E}(\boldsymbol{r},t)}{\partial t^2} \tag{2.38}$$

$$\nabla^2 \boldsymbol{B}(\boldsymbol{r},t) = \frac{1}{c^2}\frac{\partial^2 \boldsymbol{B}(\boldsymbol{r},t)}{\partial t^2} \tag{2.39}$$

where

$$c^2 = \frac{1}{\varepsilon_0 \mu_0}. \tag{2.40}$$

As can be seen, these wave equations have the same formation and are independent for each component, which is composed of six scalar wave equations.

2.2.2 Gauge Transformation

Maxwell's equations are again

$$\nabla \times \boldsymbol{E}(\boldsymbol{r},t) = -\frac{\partial \boldsymbol{B}(\boldsymbol{r},t)}{\partial t} \tag{2.41}$$

$$\nabla \times \boldsymbol{H}(\boldsymbol{r},t) = \boldsymbol{j}(\boldsymbol{r},t) + \frac{\partial \boldsymbol{D}(\boldsymbol{r},t)}{\partial t} \tag{2.42}$$

$$\nabla \cdot \boldsymbol{D}(\boldsymbol{r},t) = \rho(\boldsymbol{r},t) \tag{2.43}$$

$$\nabla \cdot \boldsymbol{B}(\boldsymbol{r},t) = 0. \tag{2.44}$$

Here we represent $\boldsymbol{B}(\boldsymbol{r},t)$ as follows

$$\boldsymbol{B}(\boldsymbol{r},t) = \nabla \times \boldsymbol{A}(\boldsymbol{r},t), \tag{2.45}$$

then eq.(2.45) is satisfied with eq.(2.44) automatically. Here $\boldsymbol{A}(\boldsymbol{r},t)$ represents vector potential, and this is a differentiable function. Also, substituting eq.(2.45) into eq.(2.41), we obtain

$$\nabla \times \left\{ \boldsymbol{E}(\boldsymbol{r},t) + \frac{\partial \boldsymbol{A}(\boldsymbol{r},t)}{\partial t} \right\} = 0. \tag{2.46}$$

Eq.(2.46) must be satisfied with the relationship below

$$\boldsymbol{E}(\boldsymbol{r},t) + \frac{\partial \boldsymbol{A}(\boldsymbol{r},t)}{\partial t} = -\nabla \phi(\boldsymbol{r},t). \tag{2.47}$$

Here, $\phi(\boldsymbol{r},t)$ represents scalar potential. Therefore, $\boldsymbol{E}(\boldsymbol{r},t)$ and $\boldsymbol{B}(\boldsymbol{r},t)$ are represented by $\boldsymbol{A}(\boldsymbol{r},t)$ and $\phi(\boldsymbol{r},t)$

$$\boldsymbol{E}(\boldsymbol{r},t) = -\frac{\partial \boldsymbol{A}(\boldsymbol{r},t)}{\partial t} - \nabla \phi(\boldsymbol{r},t) \tag{2.48}$$

$$\boldsymbol{B}(\boldsymbol{r},t) = \nabla \times \boldsymbol{A}(\boldsymbol{r},t). \tag{2.49}$$

Next we must find the equation to determine $\boldsymbol{A}(\boldsymbol{r},t)$ and $\phi(\boldsymbol{r},t)$. By substituting eq.(2.48) and eq.(2.49) into eq.(2.42)

$$\nabla \left\{ \nabla \cdot \boldsymbol{A}(\boldsymbol{r},t) + \frac{1}{c^2} \frac{\partial \phi(\boldsymbol{r},t)}{\partial t} \right\} - \left(\nabla^2 \boldsymbol{A}(\boldsymbol{r},t) - \frac{1}{c^2} \frac{\partial^2 \boldsymbol{A}(\boldsymbol{r},t)}{\partial t^2} \right) = \mu_0 \boldsymbol{j}(\boldsymbol{r},t). \tag{2.50}$$

Also, by substituting eq.(2.48) and eq.(2.49) into eq.(2.41)

$$\frac{\partial}{\partial t} \left\{ \nabla \cdot \boldsymbol{A}(\boldsymbol{r},t) + \frac{1}{c^2} \frac{\partial \phi(\boldsymbol{r},t)}{\partial t} \right\} + \left(\nabla^2 - \frac{1}{c^2} \frac{\partial^2}{\partial t^2} \right) \phi(\boldsymbol{r},t) = -\frac{\rho(\boldsymbol{r},t)}{\varepsilon_0}. \tag{2.51}$$

Therefore, we can determine $\boldsymbol{A}(\boldsymbol{r},t)$ and $\boldsymbol{\phi}(\boldsymbol{r},t)$ by solving eq.(2.50) and eq.(2.51). Then, by substituting these results into eq.(2.48) and eq.(2.49), respectively, we can obtain $\boldsymbol{E}(\boldsymbol{r},t)$ and $\boldsymbol{B}(\boldsymbol{r},t)$. However, even when $\boldsymbol{A}_G(\boldsymbol{r},t)$ and $\phi_G(\boldsymbol{r},t)$ are made by adding arbitrary functions to $\boldsymbol{A}(\boldsymbol{r},t)$ and $\phi(\boldsymbol{r},t)$, the $\boldsymbol{E}(\boldsymbol{r},t)$ and $\boldsymbol{B}(\boldsymbol{r},t)$ remains unchanged by substituting $\boldsymbol{A}_G(\boldsymbol{r},t)$ and $\phi_G(\boldsymbol{r},t)$.

$$\boldsymbol{A}_{\mathrm{G}}(\boldsymbol{r},t) = \boldsymbol{A}(\boldsymbol{r},t) + \nabla u(\boldsymbol{r},t) \tag{2.52}$$

$$\phi_{\mathrm{G}}(\boldsymbol{r},t) = \phi(\boldsymbol{r},t) - \frac{\partial u(\boldsymbol{r},t)}{\partial t}. \tag{2.53}$$

That is, by substituting eq.(2.52) and eq.(2.53) into eq.(2.45) and eq.(2.48)

$$\boldsymbol{B}(\boldsymbol{r},t) = \nabla \times \boldsymbol{A}_{\mathrm{G}}(\boldsymbol{r},t) \tag{2.54}$$

$$\boldsymbol{E}(\boldsymbol{r},t) = -\frac{\partial \boldsymbol{A}_{\mathrm{G}}(\boldsymbol{r},t)}{\partial t} - \nabla\phi_{\mathrm{G}}(\boldsymbol{r},t) \tag{2.55}$$

This arbitrariness of $\boldsymbol{A}(\boldsymbol{r},t)$ and $\phi(\boldsymbol{r},t)$ is called Gauge freedom, and the relationship between eq.(2.52) and eq.(2.53) is called Gauge transformation. Since $u(\boldsymbol{r},t)$ is an arbitrary function, $\boldsymbol{A}_{\mathrm{G}}(\boldsymbol{r},t)$ and $\phi_{\mathrm{G}}(\boldsymbol{r},t)$ have Gauge uncertainty. To put a restriction on Gauge freedom (called Gauge fixing), we explain two classical Gauge fixings, Lorentz Gauge and Coulomb Gauge. We will then show the radiation Gauge, which is a special case of these Gauges.

2.2.2.1 Lorentz Gauge

The Lorentz Gauge condition is represented by

$$\nabla \cdot \boldsymbol{A}_{\mathrm{L}}(\boldsymbol{r},t) + \frac{1}{c^2}\frac{\partial \phi_{\mathrm{L}}(\boldsymbol{r},t)}{\partial t} = 0, \tag{2.56}$$

then

$$\left(\nabla^2 - \frac{1}{c^2}\frac{\partial^2}{\partial t^2}\right)\boldsymbol{A}_{\mathrm{L}}(\boldsymbol{r},t) = -\mu_0 \boldsymbol{i}(\boldsymbol{r},t) \tag{2.57}$$

$$\left(\nabla^2 - \frac{1}{c^2}\frac{\partial^2}{\partial t^2}\right)\boldsymbol{\phi}_{\mathrm{L}}(\boldsymbol{r},t) = -\frac{\rho(\boldsymbol{r},t)}{\varepsilon_0} \tag{2.58}$$

$$\boldsymbol{E}(\boldsymbol{r},t) = -\frac{\partial \boldsymbol{A}_{\mathrm{L}}(\boldsymbol{r},t)}{\partial t} - \nabla\phi_{\mathrm{L}}(\boldsymbol{r},t) \tag{2.59}$$

$$\boldsymbol{B}(\boldsymbol{r},t) = \nabla \times \boldsymbol{A}_{\mathrm{L}}(\boldsymbol{r},t) \tag{2.60}$$

where $\boldsymbol{A}_{\mathrm{L}}(\boldsymbol{r},t)$ and $\phi_{\mathrm{L}}(\boldsymbol{r},t)$ are vector and scalar potentials in Lorentz Gauge. However, these equations from eq.(2.57) to eq.(2.58) have to be unchanged by Gauge transformation

as follows

$$\boldsymbol{A}'_{\mathrm{L}}(\boldsymbol{r},t) = \boldsymbol{A}_{\mathrm{L}}(\boldsymbol{r},t) + \nabla u_{\mathrm{L}}(\boldsymbol{r},t) \tag{2.61}$$

$$\phi'_{\mathrm{L}}(\boldsymbol{r},t) = \phi_{\mathrm{L}}(\boldsymbol{r},t) - \frac{\partial u_{\mathrm{L}}(\boldsymbol{r},t)}{\partial t} \tag{2.62}$$

where $u_{\mathrm{L}}(\boldsymbol{r},t)$ is arbitrary function. Eq.(2.57) and eq.(2.58) are equivalent to setting the first term of eq.(2.50) and eq.(2.51) equal to 0. Since the translated $\boldsymbol{A}'_{\mathrm{L}}(\boldsymbol{r},t)$ and $\boldsymbol{\phi}'_{\mathrm{L}}(\boldsymbol{r},t)$ have to be satisfied with this gauge condition, we need to determine the $u_{\mathrm{L}}(\boldsymbol{r},t)$. The equation which determines $u_{\mathrm{L}}(\boldsymbol{r},t)$ properly is given by substituting eq.(2.61) and eq.(2.62) into (2.56),

$$\nabla^2 u_{\mathrm{L}}(\boldsymbol{r},t) - \frac{1}{c^2}\frac{\partial^2 u_{\mathrm{L}}(\boldsymbol{r},t)}{\partial t^2} = -\left\{\nabla\cdot\boldsymbol{A}_{\mathrm{L}}(\boldsymbol{r},t) + \frac{1}{c^2}\frac{\partial \phi_{\mathrm{L}}(\boldsymbol{r},t)}{\partial t}\right\}. \tag{2.63}$$

Therefore, we can obtain the electric field and the magnetic field by solving eq.(2.57), eq.(2.58), and eq.(2.63) in the Lorentz Gauge.

2.2.2.2 Coulomb Gauge

The Coulomb Gauge condition is represented by

$$\nabla\cdot\boldsymbol{A}_{\mathrm{C}}(\boldsymbol{r},t) = 0 \tag{2.64}$$

then

$$\left(\nabla^2 - \frac{1}{c^2}\frac{\partial^2}{\partial t^2}\right)\boldsymbol{A}_{\mathrm{C}}(\boldsymbol{r},t) = -\mu_0\boldsymbol{i}(\boldsymbol{r},t) + \frac{1}{c^2}\frac{\partial(\nabla\phi_{\mathrm{C}}(\boldsymbol{r},t))}{\partial t} \tag{2.65}$$

$$\nabla^2\phi_{\mathrm{C}}(\boldsymbol{r},t) = -\frac{\rho(\boldsymbol{r},t)}{\varepsilon_0} \tag{2.66}$$

$$\boldsymbol{E}(\boldsymbol{r},t) = -\frac{\partial\boldsymbol{A}_{\mathrm{C}}(\boldsymbol{r},t)}{\partial t} - \nabla\phi_{\mathrm{C}}(\boldsymbol{r},t) \tag{2.67}$$

$$\boldsymbol{B}(\boldsymbol{r},t) = \nabla\times\boldsymbol{A}_{\mathrm{C}}(\boldsymbol{r},t) \tag{2.68}$$

where $\boldsymbol{A}_{\mathrm{C}}(\boldsymbol{r},t)$ and $\phi_{\mathrm{C}}(\boldsymbol{r},t)$ are vector and scalar potentials in Coulomb Gauge. However, these equations from eq.(2.65) to eq.(2.66) must be unchanged by Gauge transformation as follows

$$\boldsymbol{A}'_{\mathrm{C}}(\boldsymbol{r},t) = \boldsymbol{A}_{\mathrm{C}}(\boldsymbol{r},t) + \nabla u_{\mathrm{C}}(\boldsymbol{r},t) \tag{2.69}$$

$$\phi'_{\mathrm{C}}(\boldsymbol{r},t) = \phi_{\mathrm{C}}(\boldsymbol{r},t) - \frac{\partial u_{\mathrm{C}}(\boldsymbol{r},t)}{\partial t}. \tag{2.70}$$

Similarly, in order to determine the arbitrary function $u_{\mathrm{C}}(\boldsymbol{r},t)$, we substitute eq.(2.69) into (2.64), then,

$$\nabla^2 u_{\mathrm{C}}(\boldsymbol{r},t) = -\nabla\cdot\boldsymbol{A}_{\mathrm{C}}(\boldsymbol{r},t). \tag{2.71}$$

In the Coulomb Gauge, we can consider two possible situations because the Coulomb Gauge condition can be understood such that $\frac{\partial \phi_{\mathrm{L}}(\boldsymbol{r},t)}{\partial t} = 0$ or $\phi_{\mathrm{L}}(\boldsymbol{r},t) = 0$ in the Lorentz Gauge condition. The former condition represents the static electric field, while the latter condition represents vacuum space without charge.

2.2.2.3 Radiation Gauge

In the case where the current density and the charge density are both zero, Lorentz Gauge and Coulomb Gauge lead to the same Gauge condition, which is called radiation Gauge. In the Lorentz Gauge, we can choose the new vector potential as $\boldsymbol{A}'_{\mathrm{L}}(\boldsymbol{r},t) = 0$. In this case, we also determine the $u_{\mathrm{L}}(\boldsymbol{r},t)$ as the solution of the equation below

$$\frac{\partial u_{\mathrm{L}}(\boldsymbol{r},t)}{\partial t} = \phi_{\mathrm{L}}(\boldsymbol{r},t). \tag{2.72}$$

Since the solution of eq.(2.72) is satisfied with eq.(2.63), Maxwell's equation in the Lorentz Gauge becomes as follows

$$\begin{aligned}
\nabla \cdot \boldsymbol{A}(\boldsymbol{r},t) &= 0 && (2.73)\\
\left(\nabla^2 - \frac{1}{c^2}\frac{\partial^2}{\partial t^2}\right)\boldsymbol{A}(\boldsymbol{r},t) &= 0 && (2.74)\\
\boldsymbol{E}(\boldsymbol{r},t) &= -\frac{\partial \boldsymbol{A}(\boldsymbol{r},t)}{\partial t} && (2.75)\\
\boldsymbol{B}(\boldsymbol{r},t) &= \nabla \times \boldsymbol{A}(\boldsymbol{r},t). && (2.76)
\end{aligned}$$

The same result can be obtained from the Coulomb Gauge without the current density and the charge density.

2.2.3 Liénard Wiechert Potential

In this section, we consider the radiation field created by moving charged particle along the arbitrary orbit [2]. To begin with, we consider the radiation from the charges distributed in space with intense oscillation. In this case, the fundamental equations are Maxwell's equations in Lorentz Gauge with non-zero current density and charge density, which exist in the infinitesimal space. To obtain the potentials $\boldsymbol{A}(\boldsymbol{r},t)$ and $\phi(\boldsymbol{r},t)$ created by these

sources, we consider the Fourier transformation regarding time as follows

$$\boldsymbol{A}(\boldsymbol{r},t) = \int_{-\infty}^{\infty} \mathrm{d}\omega \tilde{\boldsymbol{A}}(\boldsymbol{r},\omega)e^{-i\omega t} \tag{2.77}$$

$$\phi(\boldsymbol{r},t) = \int_{-\infty}^{\infty} \mathrm{d}\omega \tilde{\phi}(\boldsymbol{r},\omega)e^{-i\omega t} \tag{2.78}$$

$$\boldsymbol{i}(\boldsymbol{r},t) = \int_{-\infty}^{\infty} \mathrm{d}\omega \tilde{\boldsymbol{i}}(\boldsymbol{r},\omega)e^{-i\omega t} \tag{2.79}$$

$$\rho(\boldsymbol{r},t) = \int_{-\infty}^{\infty} \mathrm{d}\omega \tilde{\rho}(\boldsymbol{r},\omega)e^{-i\omega t} \tag{2.80}$$

where $\tilde{\boldsymbol{A}}(\boldsymbol{r},\omega)$, $\tilde{\phi}(\boldsymbol{r},\omega)$, $\tilde{\boldsymbol{i}}(\boldsymbol{r},\omega)$, and $\tilde{\rho}(\boldsymbol{r},\omega)$ are Fourier compoments, respectively. By substituting from eq.(2.77) to eq.(2.80) into eq.(2.57) and eq.(2.58), we can obtain the nonhomogeneous Helmholtz equations regarding $\tilde{\boldsymbol{A}}(\boldsymbol{r},\omega)$ and $\tilde{\phi}(\boldsymbol{r},\omega)$

$$\left(\nabla^2 + \frac{\omega^2}{c^2}\right)\tilde{\boldsymbol{A}}(\boldsymbol{r},\omega) = -\mu_0\tilde{\boldsymbol{i}}(\boldsymbol{r},\omega) \tag{2.81}$$

$$\left(\nabla^2 + \frac{\omega^2}{c^2}\right)\tilde{\phi}(\boldsymbol{r},\omega) = -\frac{1}{\varepsilon_0}\tilde{\rho}(\boldsymbol{r},\omega). \tag{2.82}$$

In order to solve the equations eq.(2.81) and eq.(2.82), we consider the Green function $G(\boldsymbol{r})$ which is satisfied with the equation below

$$\left(\nabla^2 + \frac{\omega^2}{c^2}\right)G(\boldsymbol{r}) = -\delta(\boldsymbol{r}). \tag{2.83}$$

Once Green function is found, $\tilde{\boldsymbol{A}}(\boldsymbol{r},\omega)$ and $\tilde{\phi}(\boldsymbol{r},\omega)$ are represented by using the Green function as follows

$$\tilde{\boldsymbol{A}}(\boldsymbol{r},\omega) = \mu_0\int_V \mathrm{d}\boldsymbol{r}G(\boldsymbol{r}-\boldsymbol{r}')\tilde{\boldsymbol{i}}(\boldsymbol{r}',\omega) \tag{2.84}$$

$$\tilde{\phi}(\boldsymbol{r},\omega) = \frac{1}{\varepsilon_0}\int_V \mathrm{d}\boldsymbol{r}G(\boldsymbol{r}-\boldsymbol{r}')\tilde{\rho}(\boldsymbol{r}',\omega). \tag{2.85}$$

It is well known that the solution of eq.(2.83) is as follows

$$G(\boldsymbol{r}) = \frac{1}{4\pi}\frac{e^{\pm i\frac{\omega}{c}|\boldsymbol{r}|}}{|\boldsymbol{r}|}. \tag{2.86}$$

By substituting eq.(2.84) with eq.(2.86) into eq.(2.77), we can obtain

$$\begin{aligned}
\boldsymbol{A}(\boldsymbol{r},t) &= \mu_0 \int_{-\infty}^{\infty} \mathrm{d}\omega e^{-i\omega t} \int_V \mathrm{d}\boldsymbol{r}' G(\boldsymbol{r}-\boldsymbol{r}') \tilde{\boldsymbol{i}}(\boldsymbol{r}',\omega) \\
&= \mu_0 \int_{-\infty}^{\infty} \mathrm{d}\omega e^{-i\omega t} \int_V \mathrm{d}\boldsymbol{r}' G(\boldsymbol{r}-\boldsymbol{r}') \frac{1}{2\pi} \int_{-\infty}^{\infty} \mathrm{d}t' \boldsymbol{i}(\boldsymbol{r}',t') e^{i\omega t'} \\
&= \frac{\mu_0}{4\pi} \int_V \mathrm{d}\boldsymbol{r}' \frac{1}{|\boldsymbol{r}-\boldsymbol{r}'|} \int_{-\infty}^{\infty} \mathrm{d}t' \boldsymbol{i}(\boldsymbol{r}',t') \frac{1}{2\pi} \int_{-\infty}^{\infty} \mathrm{d}\omega e^{-i\left(\omega(t-t') \mp \frac{\omega}{c}|\boldsymbol{r}-\boldsymbol{r}'|\right)} \\
&= \frac{\mu_0}{4\pi} \int_V \mathrm{d}\boldsymbol{r}' \int_{-\infty}^{\infty} \mathrm{d}t' \frac{\delta\left(t-t' \mp \frac{|\boldsymbol{r}-\boldsymbol{r}'|}{c}\right)}{|\boldsymbol{r}-\boldsymbol{r}'|} \boldsymbol{i}(\boldsymbol{r}',t') \qquad (2.87)
\end{aligned}$$

where we have used properties of Dirac delta function

$$\begin{aligned}
\delta(x) &= \frac{1}{2\pi} \int_{-\infty}^{\infty} \mathrm{d}\omega e^{i\omega x} \qquad (2.88) \\
\delta(x) &= \delta(-x), \qquad (2.89)
\end{aligned}$$

and also inverse Fourier transformation of the eq.(2.79)

$$\tilde{\boldsymbol{i}}(\boldsymbol{r},\omega) = \frac{1}{2\pi} \int_{-\infty}^{\infty} \mathrm{d}t' \boldsymbol{i}(\boldsymbol{r},t') e^{i\omega t'}. \qquad (2.90)$$

Likewise for the $\phi(\boldsymbol{r},t)$,

$$\begin{aligned}
\phi(\boldsymbol{r},t) &= \frac{1}{\varepsilon_0} \int_{-\infty}^{\infty} \mathrm{d}\omega e^{-i\omega t} \int_V \mathrm{d}\boldsymbol{r}' G(\boldsymbol{r}-\boldsymbol{r}') \tilde{\rho}(\boldsymbol{r}',\omega) \\
&= \frac{1}{\varepsilon_0} \int_{-\infty}^{\infty} \mathrm{d}\omega e^{-i\omega t} \int_V \mathrm{d}\boldsymbol{r}' G(\boldsymbol{r}-\boldsymbol{r}') \frac{1}{2\pi} \int_{-\infty}^{\infty} \mathrm{d}t' \rho(\boldsymbol{r}',t') e^{i\omega t'} \\
&= \frac{1}{4\pi\varepsilon_0} \int_V \mathrm{d}\boldsymbol{r}' \frac{1}{|\boldsymbol{r}-\boldsymbol{r}'|} \int_{-\infty}^{\infty} \mathrm{d}t' \rho(\boldsymbol{r}',t') \frac{1}{2\pi} \int_{-\infty}^{\infty} \mathrm{d}\omega e^{-i\left(\omega(t-t') \mp \frac{\omega}{c}|\boldsymbol{r}-\boldsymbol{r}'|\right)} \\
&= \frac{1}{4\pi\varepsilon_0} \int_V \mathrm{d}\boldsymbol{r}' \int_{-\infty}^{\infty} \mathrm{d}t' \frac{\delta\left(t-t' \mp \frac{|\boldsymbol{r}-\boldsymbol{r}'|}{c}\right)}{|\boldsymbol{r}-\boldsymbol{r}'|} \rho(\boldsymbol{r}',t'), \qquad (2.91)
\end{aligned}$$

where we have used properties of Dirac delta function eq.(2.88) and eq.(2.89), and inverse Fourier transformation of the eq.(2.80)

$$\tilde{\rho}(\boldsymbol{r},\omega) = \frac{1}{2\pi} \int_{-\infty}^{\infty} \mathrm{d}t' \rho(\boldsymbol{r},t') e^{i\omega t'}. \qquad (2.92)$$

Therefore, by time integrating of eq.(2.87) and eq.(2.91), $\boldsymbol{A}(\boldsymbol{r},t)$ and $\phi(\boldsymbol{r},t)$ are represented as follows

$$\boldsymbol{A}(\boldsymbol{r},t) = \frac{\mu_0}{4\pi}\int_V \mathrm{d}\boldsymbol{r}'\frac{\boldsymbol{i}(\boldsymbol{r}',t')}{|\boldsymbol{r}-\boldsymbol{r}'|} \tag{2.93}$$

$$\phi(\boldsymbol{r},t) = \frac{1}{4\pi\varepsilon_0}\int_V \mathrm{d}\boldsymbol{r}'\frac{\rho(\boldsymbol{r}',t')}{|\boldsymbol{r}-\boldsymbol{r}'|} \tag{2.94}$$

where the t' in eq.(2.93) and eq.(2.94) is

$$t' = t \mp \frac{|\boldsymbol{r}-\boldsymbol{r}'|}{c}. \tag{2.95}$$

In eq.(2.93) and eq.(2.94), these potentials with the negative signs are called retarded potential. On the other hand, the potentials with a plus sign are called advanced potential. The retarded potential means that the observer position at $|\boldsymbol{r}-\boldsymbol{r}'|$ observes the electromagnetic field with delayed time $t' + \frac{|\boldsymbol{r}-\boldsymbol{r}'|}{c}$ when the electromagnetic field is generated by the source $\boldsymbol{r}'$ at t'. While the advanced potential means that in order to observe the electromagnetic field on the observer position at $t' - \frac{|\boldsymbol{r}-\boldsymbol{r}'|}{c}$, the source has to have existed in past time.

From now on, we consider the radiation from the current density and charge density represented by the Dirac delta function. This means we can calculate the electromagnetic field created by charged particle. Then, the current density and the charge density are represented as:

$$\rho(\boldsymbol{r},t) = q\delta(\boldsymbol{r}-\boldsymbol{r}_q(\boldsymbol{r})) \tag{2.96}$$

$$\boldsymbol{i}(\boldsymbol{r},t) = q\frac{\mathrm{d}\boldsymbol{r}(t)}{\mathrm{d}t}\delta(\boldsymbol{r}-\boldsymbol{r}_q(\boldsymbol{r})). \tag{2.97}$$

For the convenience of calculation, we start from eq.(2.87) and eq.(2.91) by substituting eq.(2.96) and eq.(2.97) into them. Then

$$\boldsymbol{A}(\boldsymbol{r},t) = \frac{\mu_0 q}{4\pi}\int_V \mathrm{d}\boldsymbol{r}'\int_{-\infty}^{\infty}\mathrm{d}t'\frac{\delta\left(t-t'-\frac{|\boldsymbol{r}-\boldsymbol{r}'|}{c}\right)}{|\boldsymbol{r}-\boldsymbol{r}'|}\frac{\mathrm{d}\boldsymbol{r}_q(t')}{\mathrm{d}t'}\delta(\boldsymbol{r}'-\boldsymbol{r}_q(t')) \tag{2.98}$$

$$\phi(\boldsymbol{r},t) = \frac{q}{4\pi\varepsilon_0}\int_V \mathrm{d}\boldsymbol{r}'\int_{-\infty}^{\infty}\mathrm{d}t'\frac{\delta\left(t-t'-\frac{|\boldsymbol{r}-\boldsymbol{r}'|}{c}\right)}{|\boldsymbol{r}-\boldsymbol{r}'|}\delta(\boldsymbol{r}'-\boldsymbol{r}_q(t')). \tag{2.99}$$

Integration over $\boldsymbol{r}'$ can be easily performed. Then

$$\boldsymbol{A}(\boldsymbol{r},t) = \frac{\mu_0 q}{4\pi}\int_{-\infty}^{\infty}\mathrm{d}t'\frac{\delta\left(t-t'-\frac{|\boldsymbol{r}-\boldsymbol{r}_q(t')|}{c}\right)}{|\boldsymbol{r}-\boldsymbol{r}_q(t')|}\frac{\mathrm{d}\boldsymbol{r}_q(t')}{\mathrm{d}t'} \tag{2.100}$$

$$\phi(\boldsymbol{r},t) = \frac{q}{4\pi\varepsilon_0}\int_{-\infty}^{\infty}\mathrm{d}t'\frac{\delta\left(t-t'-\frac{|\boldsymbol{r}-\boldsymbol{r}_q(t')|}{c}\right)}{|\boldsymbol{r}-\boldsymbol{r}_q(t')|}. \tag{2.101}$$

The integration concerning t' is complicated due to $\boldsymbol{r}(t')$, but the integration can be performed by change of variable. As a result, we can obtain

$$\boldsymbol{A}(\boldsymbol{r},t) = \frac{\mu_0 q}{4\pi}\frac{1}{|\boldsymbol{r}-\boldsymbol{r}_q(t')| - \frac{1}{c}\frac{\mathrm{d}\boldsymbol{r}_q(t')}{\mathrm{d}t'}\cdot(\boldsymbol{r}-\boldsymbol{r}_q(t'_0))}\frac{\mathrm{d}\boldsymbol{r}_q(t')}{\mathrm{d}t'} \tag{2.102}$$

$$\phi(\boldsymbol{r},t) = \frac{q}{4\pi\varepsilon_0}\frac{1}{|\boldsymbol{r}-\boldsymbol{r}_q(t')| - \frac{1}{c}\frac{\mathrm{d}\boldsymbol{r}_q(t')}{\mathrm{d}t'}\cdot(\boldsymbol{r}-\boldsymbol{r}_q(t'))} \tag{2.103}$$

where

$$t' = t - \frac{\boldsymbol{r}-\boldsymbol{r}_q(t')}{c}. \tag{2.104}$$

Eq.(2.102) and eq.(2.103) are called Liénard-Wiechert potential, which describes the electromagnetic field created by a charged particle with arbitrary motion. Furthermore, by differentiating by using eq.(2.59) and eq.(2.60), the electric field and the magnetic field at the observer position can be calculated. Then

$$\boldsymbol{E}(\boldsymbol{r},t) = \frac{q}{4\pi\varepsilon_0}\left\{\frac{(\boldsymbol{n}-\boldsymbol{\beta}(t'))(1-|\boldsymbol{\beta}(t')|^2)}{(1-\boldsymbol{n}\cdot\boldsymbol{\beta}(t'))^3|\boldsymbol{R}|^2} + \frac{\boldsymbol{n}\times(\boldsymbol{n}-\boldsymbol{\beta}(t'))\times\dot{\boldsymbol{\beta}}(t')}{c(1-\boldsymbol{n}\cdot\boldsymbol{\beta}(t'))^3|\boldsymbol{R}|}\right\} \tag{2.105}$$

$$\begin{aligned}\boldsymbol{B}(\boldsymbol{x},t) = \frac{q}{4\pi\varepsilon_0 c}\Bigg\{&\frac{(\boldsymbol{\beta}(t')\times\boldsymbol{n})(1-|\boldsymbol{\beta}(t')|^2)}{(1-\boldsymbol{n}\cdot\boldsymbol{\beta}(t'))^3|\boldsymbol{R}|^2} \\ &+\frac{(\boldsymbol{\beta}(t')\times\boldsymbol{n})(\boldsymbol{n}\cdot\boldsymbol{\beta}(t')) + (\dot{\boldsymbol{\beta}}(t')\times\boldsymbol{n})(1-\boldsymbol{n}\cdot\boldsymbol{\beta}(t'))}{c(1-\boldsymbol{n}\cdot\boldsymbol{\beta}(t'))^3|\boldsymbol{R}|}\Bigg\}\end{aligned} \tag{2.106}$$

where

$$\boldsymbol{R} \equiv \boldsymbol{r} - \boldsymbol{r}_q(t'), \tag{2.107}$$

$$\boldsymbol{n} \equiv \frac{\boldsymbol{R}}{|\boldsymbol{R}|}. \tag{2.108}$$

2.3 Diffraction Theory

2.3.1 Huygens-Fresnel Principle

In 1678, an important principle describing the propagation of the wave was proposed by the Dutch physicist Christiaan Huygens. A wavefront at a given time produces wavelets at each point on the wavefront as a wave source, then the wavelets propagate as a spherical

wave. And the envelope in contact with the wavefronts of the wavelet becomes a new wavefront at the next time step (See Fig.2.1). This is called the Huygens' principle [2]. The Huygens' principle well explained the propagation of the wave in a uniform material and the reflection and the refraction of the wave at the interface of different materials. However, Huygens's principle had two difficulties. In Huygens' principle, the backward wave is also generated outside the traveling wave. The other difficulty is that the diffraction phenomenon that occurs when the wave injects an opaque material cannot be explained.

In 1818, the French physicist Augustin-Jean Fresnel modified Huygens' principle to compensate for difficulties that could not be explained by Huygens' principle. According to Fresnel, the amplitude of the wavelets sent out from each point on the wavefront of the primary wave differs depending on the traveling direction. When the traveling direction of the primary wave and the second wave are the same, the amplitude is maximum, while when the traveling direction is the opposite direction to each other, the amplitude of the wavelets is zero. Furthermore, the angle between the traveling direction of the primary wave and the wavelets increases, and the amplitude of the wavelets decreases. These wavelets interfere with each other by superposition. Huygens' principle modified by Fresnel is called the Huygens-Fresnel principle. In 1882, Kirchhoff mathematically proved the Huygens-Fresnel principle, which will be derived in the next section.

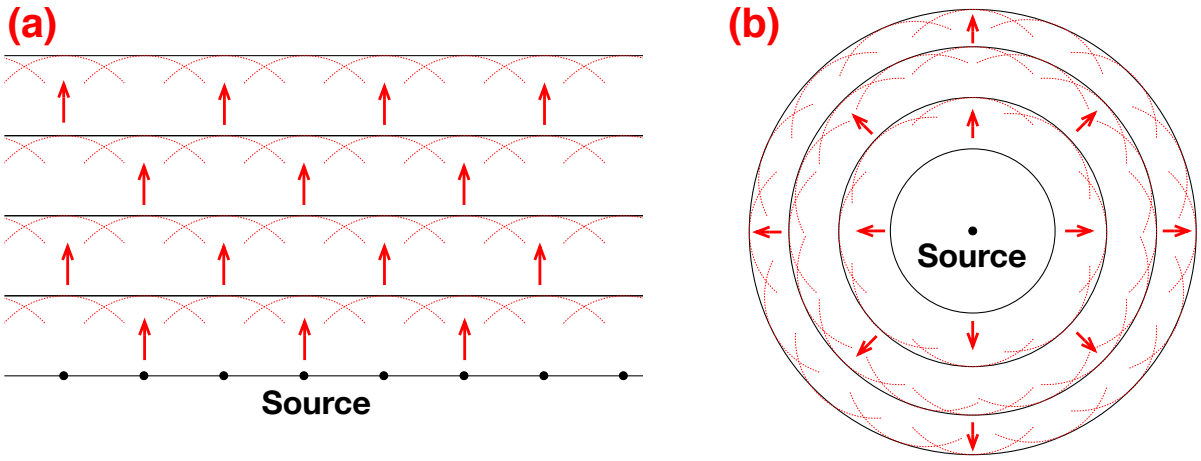

Figure 2.1: Huygens-Fresnel Principle. (a): In the case of plane wave. (b): In the case of spherical wave. A wavefront at a given time produces wavelets at each point on the wavefront as a wave source, then the wavelets propagate as a spherical wave. And the envelope in contact with the wavefronts of the wavelet becomes a new wavefront at the next time step.

2.3.2 Kirchhoff's Diffraction Formula

Kirchhoff's Diffraction Formula is a mathematically strict representation of the Huygens-Fresnel principle. To begin with, we consider the propagation for an electromagnetic wave in a vacuum without any charges, which is related to the radiation Gauge. The general solution of the wave equation eq.(2.74) regarding $\boldsymbol{A}(\boldsymbol{r},t)$ can be represented as Fourier transformation as follows

$$\boldsymbol{A}(\boldsymbol{r},t)=\int_{-\infty}^{\infty}\mathrm{d}\boldsymbol{k}\left\{\tilde{\boldsymbol{A}}(\boldsymbol{k})e^{i(\boldsymbol{k}\cdot\boldsymbol{r}-\omega t)}+\tilde{\boldsymbol{A}}^{*}(\boldsymbol{k})e^{-i(\boldsymbol{k}\cdot\boldsymbol{r}-\omega t)}\right\} \tag{2.109}$$

where $\tilde{\boldsymbol{A}}(\boldsymbol{k})$ and $\tilde{\boldsymbol{A}}^{*}(\boldsymbol{k})$ are the Fourier component and the complex conjugate of the Fourier component. Generally speaking, homogeneous wave equation can be solved exactly when $\boldsymbol{A}(\boldsymbol{r},t')$ and $\frac{\mathrm{d}\boldsymbol{A}(\boldsymbol{r},t)}{\mathrm{d}t}\Big|_{t=t'}$ are given initially. Thus, we adopt the initial condition as follows

$$\boldsymbol{A}(\boldsymbol{r},t') = \boldsymbol{f}(\boldsymbol{r},t') \tag{2.110}$$

$$\left.\frac{\partial\boldsymbol{A}(\boldsymbol{r},t)}{\partial t}\right|_{t=t'} = \boldsymbol{g}(\boldsymbol{r},t'). \tag{2.111}$$

First, we multiply both sides of eq.(2.109) by $e^{-i\boldsymbol{k}'\cdot\boldsymbol{r}}$, and integrate over wavenumber space. Then we can obtain

$$\tilde{\boldsymbol{A}}(\boldsymbol{k})e^{-i\omega t}+\tilde{\boldsymbol{A}}^{*}(-\boldsymbol{k})e^{i\omega t}=\frac{1}{(2\pi)^3}\int_{-\infty}^{\infty}\mathrm{d}\boldsymbol{k}\boldsymbol{A}(\boldsymbol{r},t)e^{-i\boldsymbol{k}\cdot r}. \tag{2.112}$$

Here, we have used the property of the Dirac delta function in eq.(2.88). Also, the time derivative of $\boldsymbol{A}(\boldsymbol{r},t)$ is

$$\frac{\partial\boldsymbol{A}(\boldsymbol{r},t)}{\partial t}=\int_{-\infty}^{\infty}\mathrm{d}\boldsymbol{k}\left\{-i\omega\tilde{\boldsymbol{A}}(\boldsymbol{k})e^{i(\boldsymbol{k}\cdot\boldsymbol{r}-\omega t)}+i\omega\tilde{\boldsymbol{A}}^{*}(\boldsymbol{k})e^{-i(\boldsymbol{k}\cdot\boldsymbol{r}-\omega t)}\right\}. \tag{2.113}$$

Likewise, by multiplying both sides of eq.(2.113) by $e^{-i\boldsymbol{k}'\cdot\boldsymbol{r}}$, and integrating over wavenumber space

$$\tilde{\boldsymbol{A}}(\boldsymbol{k})e^{-i\omega t}-\tilde{\boldsymbol{A}}^{*}(-\boldsymbol{k})e^{i\omega t}=\frac{i}{(2\pi)^3}\frac{1}{\omega}\int_{-\infty}^{\infty}\mathrm{d}\boldsymbol{k}\frac{\partial\boldsymbol{A}(\boldsymbol{r},t)}{\partial t}e^{-i\boldsymbol{k}\cdot r}. \tag{2.114}$$

By adding eq.(2.112) and eq.(2.114)

$$\tilde{\boldsymbol{A}}(\boldsymbol{k})=\frac{1}{2(2\pi)^3}\int_{-\infty}^{\infty}\mathrm{d}\boldsymbol{r}'\left\{\boldsymbol{A}(\boldsymbol{r}',t)+\frac{i}{\omega}\frac{\partial\boldsymbol{A}(\boldsymbol{r}',t)}{\partial t}\right\}e^{-i(\boldsymbol{k}\cdot\boldsymbol{r}'-\omega t)}. \tag{2.115}$$

By subtracting eq.(2.112) and eq.(2.114)

$$\tilde{\boldsymbol{A}}^*(\boldsymbol{k}) = \frac{1}{2(2\pi)^3}\int_{-\infty}^{\infty} \mathrm{d}\boldsymbol{r}' \left\{ \boldsymbol{A}(\boldsymbol{r}',t) - \frac{i}{\omega}\frac{\partial \boldsymbol{A}(\boldsymbol{r}',t)}{\partial t} \right\} e^{i(\boldsymbol{k}\cdot\boldsymbol{r}'-\omega t)}. \tag{2.116}$$

Therefore, we can obtain the general solution of eq.(2.74) by substituting eq.(2.115) and eq.(2.116) with initial condition

$$\begin{aligned}
\boldsymbol{A}(\boldsymbol{r},t) &= \int_{-\infty}^{\infty}\mathrm{d}\boldsymbol{k}\frac{1}{2(2\pi)^3}\int_{-\infty}^{\infty}\mathrm{d}\boldsymbol{r}'\left\{\boldsymbol{f}(\boldsymbol{r}',t') + \frac{i}{\omega}\boldsymbol{g}(\boldsymbol{r}',t')\right\}e^{i(\boldsymbol{k}\cdot\boldsymbol{r}'-\omega t')} \\
&\quad + \int_{-\infty}^{\infty}\mathrm{d}\boldsymbol{k}\frac{1}{2(2\pi)^3}\int_{-\infty}^{\infty}\mathrm{d}\boldsymbol{r}'\left\{\boldsymbol{f}(\boldsymbol{r}',t') - \frac{i}{\omega}\boldsymbol{g}(\boldsymbol{r}',t')\right\}e^{-i(\boldsymbol{k}\cdot\boldsymbol{r}'-\omega t')} \\
&= \frac{1}{2(2\pi)^3}\int_{-\infty}^{\infty}\mathrm{d}\boldsymbol{r}'\boldsymbol{f}(\boldsymbol{r}',t)\int_{-\infty}^{\infty}\mathrm{d}\boldsymbol{k}\left\{e^{i\boldsymbol{k}\cdot(\boldsymbol{r}-\boldsymbol{r}')-i\omega(t-t')} + e^{-i\boldsymbol{k}\cdot(\boldsymbol{r}-\boldsymbol{r}')+i\omega(t-t')}\right\} \\
&\quad + \frac{1}{2(2\pi)^3}\int_{-\infty}^{\infty}\mathrm{d}\boldsymbol{r}'\boldsymbol{g}(\boldsymbol{r}',t)\int_{-\infty}^{\infty}\mathrm{d}\boldsymbol{k}\frac{1}{\omega}\left\{e^{i\boldsymbol{k}\cdot(\boldsymbol{r}-\boldsymbol{r}')-i\omega(t-t')} + e^{-i\boldsymbol{k}\cdot(\boldsymbol{r}-\boldsymbol{r}')+i\omega(t-t')}\right\}.
\end{aligned} \tag{2.117}$$

Here we define the function $D(\boldsymbol{r},t)$, which describes the characteristics of the propagation for an electromagnetic wave in a vacuum.

$$D(\boldsymbol{r},t) \equiv \frac{i}{2(2\pi)^3}\int_{-\infty}^{\infty}\mathrm{d}\boldsymbol{k}\frac{1}{\omega}\left\{e^{i(\boldsymbol{k}\cdot\boldsymbol{r}-\omega t)} - e^{-i(\boldsymbol{k}\cdot\boldsymbol{r}-\omega t)}\right\}. \tag{2.118}$$

Finally, $\boldsymbol{A}(\boldsymbol{r},t)$ is represented more simply as follows

$$\boldsymbol{A}(\boldsymbol{r},t) = \int_{-\infty}^{\infty}\mathrm{d}\boldsymbol{x}'\left\{\frac{\partial D(\boldsymbol{r}-\boldsymbol{r}',t-t')}{\partial t}\boldsymbol{f}(\boldsymbol{r}',t) + D(\boldsymbol{r}-\boldsymbol{r}',t-t')\boldsymbol{g}(\boldsymbol{r}',t')\right\} \tag{2.119}$$

$D(\boldsymbol{r},t)$ function can be integrated at $\boldsymbol{k}$ space and will be represented by Dirac delta function as follows

$$D(\boldsymbol{r},t) = \frac{1}{4\pi c}\frac{1}{|\boldsymbol{r}|}\left\{\delta(|\boldsymbol{r}|-ct) - \delta(|\boldsymbol{r}|+ct)\right\} \tag{2.120}$$

In particular, $D(\boldsymbol{r},t)$ function can be written by retarded part and advanced part

$$D(\boldsymbol{r}-\boldsymbol{r}',t-t') = D_{\mathrm{ret}}(\boldsymbol{r}-\boldsymbol{r}',t-t') - D_{\mathrm{adv}}(\boldsymbol{r}-\boldsymbol{r}',t-t') \tag{2.121}$$

where

$$D_{\mathrm{ret}}(\boldsymbol{r}-\boldsymbol{r}',t-t') \equiv \frac{1}{4\pi c}\frac{1}{|\boldsymbol{r}-\boldsymbol{r}'|}\delta(|\boldsymbol{r}-\boldsymbol{r}'|-c(t-t')) \tag{2.122}$$

$$D_{\mathrm{adv}}(\boldsymbol{r}-\boldsymbol{r}',t-t') \equiv \frac{1}{4\pi c}\frac{1}{|\boldsymbol{r}-\boldsymbol{r}'|}\delta(|\boldsymbol{r}-\boldsymbol{r}'|+c(t-t')). \tag{2.123}$$

$D_{\mathrm{ret}}(\boldsymbol{r}-\boldsymbol{r}',t-t')$ is the function which describes the propagation of the wave at current time t when the initial values are given at the past time t', while $D_{\mathrm{adv}}(\boldsymbol{r}-\boldsymbol{r}',t-t')$ is the function which describes the propagation of the wave at current time t when the initial values are given at the future time t'.

Since we have been able to describe the propagation of electromagnetic waves in a vacuum, we are finally ready to derive Kirchhoff's diffraction formula. In order to derive Kirchhoff's diffraction formula, we consider the two arbitrary functions $\psi(\boldsymbol{r},t)$ and $\phi(\boldsymbol{r},t)$, which are defined in space V surrounded by closed surface S. In addition, $\psi(\boldsymbol{r},t)$ is regarded as one of the scalar field components. Here we consider Green's theorem for these two functions

$$\oint_S \left\{\phi(\boldsymbol{r},t)\frac{\partial\psi(\boldsymbol{r},t)}{\partial\boldsymbol{n}} - \psi(\boldsymbol{r},t)\frac{\partial\phi}{\partial\boldsymbol{n}}\right\}\mathrm{d}S = \int_V \left\{\phi(\boldsymbol{r},t)\nabla^2\psi(\boldsymbol{r},t) - \psi(\boldsymbol{r},t)\nabla^2\phi(\boldsymbol{r},t)\right\} \tag{2.124}$$

where the partial derivative for $\boldsymbol{n}$ means directional derivative along $\boldsymbol{n}$, and defined by as follows

$$\frac{\partial\psi(\boldsymbol{r},t)}{\partial\boldsymbol{n}} = \boldsymbol{n}\cdot\nabla\psi(\boldsymbol{r},t). \tag{2.125}$$

Here, we integrate eq.(2.124) by the time t' from t_0 to t_1, which is satisfied with $t_1 > t' > t_0$

$$\begin{aligned}&\int_{t_0}^{t_1}\mathrm{d}t'\int_V \mathrm{d}\boldsymbol{r}'\left\{\phi(\boldsymbol{r}',t')\nabla^2\psi(\boldsymbol{r}',t') - \psi(\boldsymbol{r}',t')\nabla^2\phi(\boldsymbol{r}',t')\right\}\\ &\quad= \int_{t_0}^{t_1}\mathrm{d}t'\oint_{S'}\mathrm{d}S'\left\{\phi(\boldsymbol{r}',t')\frac{\partial\psi(\boldsymbol{r}',t')}{\partial\boldsymbol{n}} - \psi(\boldsymbol{r}',t')\frac{\partial\phi}{\partial\boldsymbol{n}}\right\}.\end{aligned} \tag{2.126}$$

As mentioned, since the $\psi(\boldsymbol{r},t)$ is one of the scalar field components, $\psi(\boldsymbol{r},t)$ have to be satisfied with the wave equation below

$$\left(\nabla^2 - \frac{1}{c^2}\frac{\partial^2}{\partial t^2}\right)\psi(\boldsymbol{r},t) = 0. \tag{2.127}$$

Furthermore, $\phi(\boldsymbol{r},t)$ is considered as follows

$$\phi(\boldsymbol{r}',t) = D_{\mathrm{ret}}(\boldsymbol{r}-\boldsymbol{r}',t-t') \tag{2.128}$$

where $t_1 > t > t_0$, and $\boldsymbol{r}$ is a point in the space V. Here again, D_{ret} is the function that describes the propagation of the wave at current time t when the propagation of the wave at past time t' is known. So D_{ret} is represented by D

$$D_{\mathrm{ret}}(\boldsymbol{r},t) = \theta(t)D(\boldsymbol{r},t) \tag{2.129}$$

where the $\theta(t)$ is the Heaviside step function defined by

$$\theta(t) = \begin{cases} 1 & (t > 0) \\ 0 & (t < 0) \end{cases} \tag{2.130}$$

with

$$\frac{\mathrm{d}\theta(t)}{\mathrm{d}t} = \delta(t). \tag{2.131}$$

Then, we have found that the eq.(2.129) has to be satisfied with the relationship below

$$\left(\nabla^2 - \frac{1}{c^2}\frac{\partial^2}{\partial t^2}\right) D_{\mathrm{ret}}(\boldsymbol{r}, t) = -\frac{1}{c^2}\delta(t)\delta(\boldsymbol{r}). \tag{2.132}$$

By substitution eq.(2.128) into eq.(2.126),

$$\begin{aligned} & \int_{t_0}^{t_1} \mathrm{d}t' \int_V \mathrm{d}\boldsymbol{x}' \left\{ D_{\mathrm{ret}}(\boldsymbol{x} - \boldsymbol{x}', t - t')\nabla'^2\psi(\boldsymbol{x}', t') - \psi(\boldsymbol{x}', t')\nabla'^2 D_{\mathrm{ret}}(\boldsymbol{x} - \boldsymbol{x}', t - t') \right\} \\ = & \int_{t_0}^{t_1} \mathrm{d}t' \oint_S \mathrm{d}S' \left\{ D_{\mathrm{ret}}(\boldsymbol{x} - \boldsymbol{x}', t - t')\frac{\partial\psi(\boldsymbol{x}', t')}{\partial \boldsymbol{n}'} - \psi(\boldsymbol{x}', t')\frac{\partial}{\partial \boldsymbol{n}'} D_{\mathrm{ret}}(\boldsymbol{x} - \boldsymbol{x}', t - t') \right\}. \end{aligned} \tag{2.133}$$

Finally, by carefully performing the integration regarding t', we can obtain the equation below

$$\begin{aligned} \psi(\boldsymbol{x}, t) = & \int_V \mathrm{d}\boldsymbol{x}' \left\{ D_{\mathrm{ret}}(\boldsymbol{x} - \boldsymbol{x}', t - t')\frac{\partial\psi(\boldsymbol{x}', t')}{\partial t'} - \psi(\boldsymbol{x}', t')\frac{\partial}{\partial t} D_{\mathrm{ret}}(\boldsymbol{x} - \boldsymbol{x}', t - t') \right\} \\ & + \frac{1}{4\pi}\oint_s \mathrm{d}\boldsymbol{S}' \cdot \left(\frac{\nabla' E(r', \phi', z', t')}{R} + \frac{\boldsymbol{R}}{R^3} E(r', \phi', z', t') - \frac{\boldsymbol{R}}{cR^2}\frac{\partial E(r', \phi', z', t')}{\partial t'} \right)_{t' = t - \frac{R}{c}}. \end{aligned} \tag{2.134}$$

The first term on the right hand of the eq.(2.134) has the same form of the solution of an initial value problem for the wave equation. And the D_{ret} function includes $\delta(|\boldsymbol{r} - \boldsymbol{r}'| - c(t - t'))$, thus the only points in the space V contribute to the integration of $\boldsymbol{r}'$. Therefore, the diffracted wave at the observer position $\boldsymbol{r}$ produced by the elementary wave on the closed surface V is represented by the second term on the right hand of the eq.(2.134) as follows

$$\begin{aligned} D(r, \phi, z, t) = \frac{1}{4\pi}\oint_s \mathrm{d}\boldsymbol{S}' \cdot \Bigg(& \frac{\nabla' E(r', \phi', z', t')}{R} + \frac{\boldsymbol{R}}{R^3} E(r', \phi', z', t') \\ & - \frac{\boldsymbol{R}}{cR^2}\frac{\partial E(r', \phi', z', t')}{\partial t'} \Bigg)_{t' = t - \frac{R}{c}} \end{aligned} \tag{2.135}$$

Bibliography

[1] Y. Goto, S. Kubo, and T. I. Tsujimura, "Cyclotron Emission with a Helical Wavefront from an Electron Accelerated by the Circularly Polarized Wave," submitted for review to J. Adv. Simulat. Sci. Eng.

[2] S. Sunakawa, "Riron Denjikigaku" 3rd ed. [in Japanese] (Theoretical Electromagnetism), Kinokuniya, Tokyo, (2010).

[3] J. D. Jackson, "Classical Electrodynamics" 3rd ed., Wiley, (1998).

Chapter 3

Calculations of ECE with Helical Wavefront

3.1 Outline for the Calculations

In the calculation, we consider a situation in which Right Handed Circularly Polarized (RHCP) wave is applied into an electron with cyclotron motion in the magnetic field. In Sec.3.2, we will discuss the case where an electron with cyclotron motion in a uniform magnetic field is accelerated by RHCP wave, and in Sec.3.3, we will discuss the case where an electron with cyclotron motion in a magnetic mirror field is accelerated by RHCP wave. At this time, this RHCP wave applied from the outside plays an important role to control the electron's cyclotron motion. As a result, we can obtain the coherent radiation from such rotation phase-controlled electrons in the multi-electron system because the electron's rotation phase is followed by the phase of the externally applied electric field. The electron motion in a magnetic field when the electromagnetic wave is externally applied can be calculated by the eq.(2.26). In this calculation, the ordinary differential equation is numerically solved to obtain the electron trajectory. After that, the trajectory information is substituted into the Liénard-Wiechert potential to calculate the radiation field. Fig.3.1 shows the details of the calculation flow. First, the trajectory information can be calculated by eq.(2.26) when an electron with cyclotron motion in a magnetic field is accelerated by RHCP wave applied from the outside. What the required trajectory information for calculation of radiation field is three components of position, three components of velocity, and three components of acceleration. We use the GNU Scientific Library (GSL) for this numerical calculation. GSL provides a fourth-order Runge-Kutta method to solve the initial value problem of ordinary differential equations. This calculation is designed so that the calculation step is controlled within the acceptable error. The uniform magnetic field is set to 2.954 T which corresponds to the magnetic field strength of the cyclotron frequency with 82.7 GHz, and then the electron cyclotron period T_{ce} is

12 p sec. In this calculation, calculation time step $\Delta t = 150$ f sec. is sufficiently smaller than $T_{\rm ce}$. In the case of the magnetic mirror field, the time step is the same with the case of the uniform magnetic field. However, the magnetic field strength is set to the resonant magnetic field strength which corresponds to the Doppler-shifted frequency of the RHCP wave seen from the reference frame of the electron. Once the trajectory information is obtained, radiation field can be calculated by substituting trajectory information into Liénard-Wiechert potential. The radiation field is observed on the upper hemisphere. In the case of a uniform magnetic field, the calculation of radiation field is performed at a position where the distance from the origin is $|\boldsymbol{R}| = 15$ m, and in the case of a magnetic mirror field, the calculation of radiation field is performed at a position where $|\boldsymbol{R}| = 3$ m. Since the radiation field includes higher harmonics radiation other than the fundamental wave, the observed radiation signal is spectrally decomposed by Fast Fourier Transform (FFT). Before FFT, it is necessary to equalize the sample step by spline interpolation regarding the result of the calculated radiation field. This is because when the radiation field is calculated by Liénard-Wiechert potential, the time step becomes not uniform due to considering the retarded time. Thus, an equalized data set are required in the FFT. The inverse FFT is not necessary when we observe the time variation of the spectrum at a given point in space. The vortex property can be confirmed by comparing the phase difference at the two spatial points after FFT. However, when observing the radiation with intensity distribution and phase structure for the fundamental radiation and higher harmonics radiation at all points on the upper hemisphere, it is necessary to perform inverse FFT. GSL is also used for FFT, inverse FFT, and spline interpolation.

3.2 In the Case of a Static Magnetic Field

We consider a situation where the RHCP wave is applied into an electron with cyclotron motion in a static magnetic field [1]. As shown in Fig.3.2, an electron is injected from $z = -415$ mm with perpendicular velocity that corresponds to 20 keV. Then, the momentum of the electron only has the x-y plane, that is, the electron initially rotates on the x-y plane. In addition, the electromagnetic wave applied from the outside is considered as Gaussian beam with right-handed circular polarization as follows

$$\boldsymbol{E}_{\rm in} = E_0 \frac{\omega_0}{\omega_z} \exp\left(\frac{r^2}{\omega_z^2}\right) \exp\left\{i(kz - \omega t + \frac{kr^2}{2R} + \zeta)\right\} \boldsymbol{e}_+ \tag{3.1}$$

with

$$\boldsymbol{e}_+ = \boldsymbol{e}_x + i\boldsymbol{e}_y \tag{3.2}$$

where E_0 is the amplitude of the electric field; r and z are parameters in the cylindrical coordinate system; w_0, w_z, k, R, and ζ are waist size, spot size, wave-number, radius of

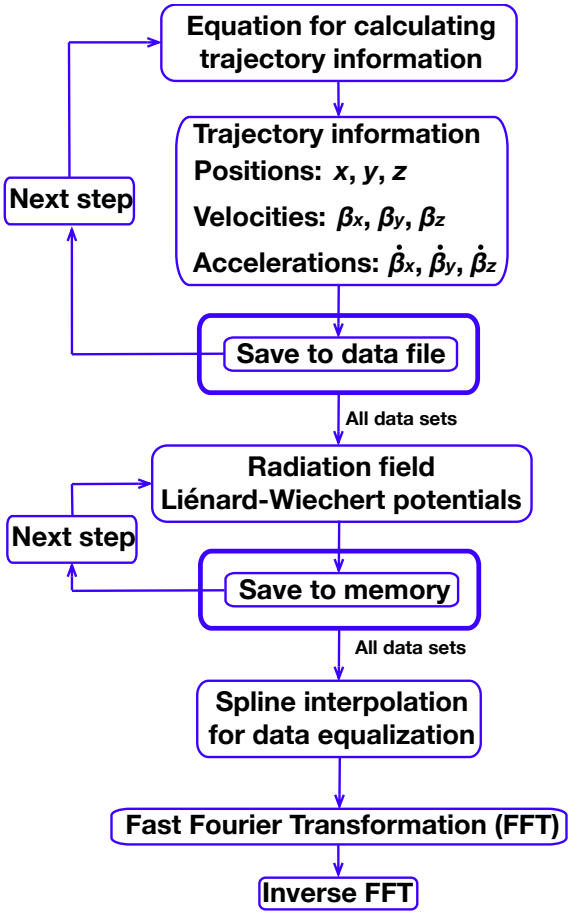

Figure 3.1: Calculation flow. First, solve the eq.(2.26) for obtaining the trajectory information, and then calculate the radiation by substituting the trajectory information into Liénard-Wiechert potential.

curvature, and Gouy phase shift, respectively. ω and t are angular frequency and time. The waist size is 30 mm, and is located at the origin. The frequency of the RHCP wave is 82.7 GHz. The power can be changed from 100 kW to 1000 kW by 100 kW. In table 3.1, the initial condition of the electron, beam parameters, and information related to the magnetic field are listed.

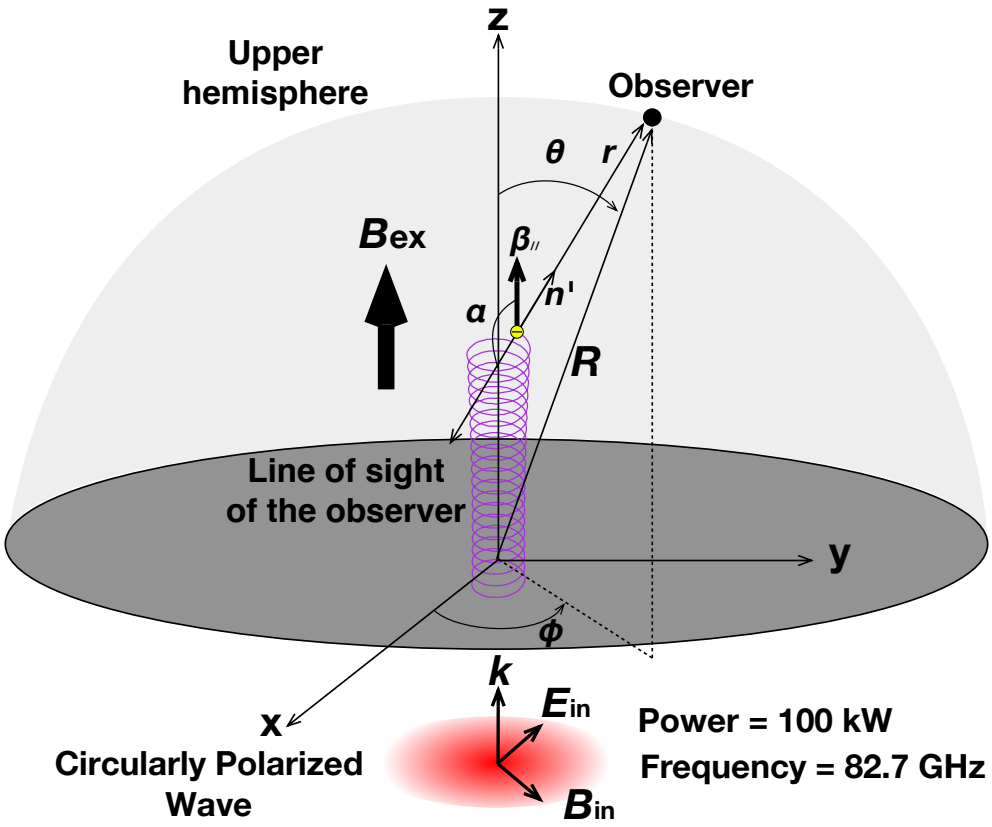

Figure 3.2: Coordinate system of the calculation where an electron with cyclotron motion in magnetic field is accelerated by the RHCP wave. The angle α between the line of sight of the observer and the propagation direction of the electron is also defined.

3.2.1 Electron Trajectory in the Electromagnetic Wave

An electron trajectory can be calculated by eq.(2.27) shown again below when the electromagnetic wave is applied to an electron with cyclotron motion.

$$\dot{\boldsymbol{\beta}} = \frac{-e}{mc\gamma}\left(\boldsymbol{I} - \boldsymbol{\beta}\otimes\boldsymbol{\beta}\right)\left((1-\boldsymbol{\beta}\cdot\boldsymbol{n})\boldsymbol{I} + \boldsymbol{n}\otimes\boldsymbol{\beta}\right)\cdot\boldsymbol{E}_{\mathrm{in}} - \frac{\omega_{\mathrm{ce}}}{\gamma}(\boldsymbol{\beta}\times\hat{\boldsymbol{e}}_z) \tag{2.27}$$

This is the relativistic equation of motion describing what happens when the electromagnetic wave is applied from the outside. As can be seen, if $\boldsymbol{E}_{\mathrm{in}} = 0$, this equation represents just a cyclotron motion. When $\boldsymbol{E}_{\mathrm{in}}$ is not equal to 0, the equation produces a result where the Larmor radius gradually increases due to resonant acceleration until the relativistic effect becomes dominant.

Fig.3.3 shows the trajectory and some parameters of the electron. Fig.3.3 (a) shows the part of the electron trajectory. It can be seen that the Larmor radius gradually becomes larger with time. However, the increase of the Larmor radius does not continue

Initial Conditions		
Position	x	0 mm
	y	0 mm
	z	-415 mm
Energy	20 keV	
Momentum	x-y direction	
Beam Parameters		
Frequency	82.7 GHz	
Power	100 kW	
Waist size	30 mm	
Polarization	RHCP wave	
Others		
Magnetic field	Uniform static 2.954 T	
Electron cyclotron frequency	82.7 GHz	
Electron cyclotron period	12 p sec.	
Calculation step	150 f sec.	

Table 3.1: Initial condition of the electron with cyclotron motion in static uniform magnetic field, beam parameters applied from the outside, and some parameters.

constantly. The Larmor radius settles to a certain value with time. This is a phenomenon caused by a phase relationship between the electron and the externally applied RHCP wave. Fig.3.3 (g) purple line shows the phase relationship between the velocity of the electron in the x-y direction $\boldsymbol{\beta}_\perp$ and the electric field $\boldsymbol{E}_{\rm in}$. Furthermore, Fig.3.3 (g) green line shows the phase relationship between the velocity of the electron in the x-y direction $\boldsymbol{\beta}_\perp$ and the magnetic field $\boldsymbol{B}_{\rm in}$. These are defined as follows

$$\cos\phi_{\boldsymbol{E}} = \frac{\boldsymbol{E}_{\rm in}\cdot\boldsymbol{\beta}_\perp}{|\boldsymbol{E}_{\rm in}||\boldsymbol{\beta}_\perp|} \tag{3.3}$$

$$\sin\phi_{\boldsymbol{B}} = \frac{\boldsymbol{B}_{\rm in}\cdot\boldsymbol{\beta}_\perp}{|\boldsymbol{B}_{\rm in}||\boldsymbol{\beta}_\perp|} \tag{3.4}$$

where $\phi_{\boldsymbol{E}}$ indicates the angle between $\boldsymbol{E}_{\rm in}$ and $\boldsymbol{\beta}_\perp$ and $\phi_{\boldsymbol{B}}$ indicates the angle between $\boldsymbol{B}_{\rm in}$ and $\boldsymbol{\beta}_\perp$. When $\cos\phi_{\boldsymbol{E}}$ changes from -1 to 1, the electron is in the acceleration phase, while $\cos\phi_{\boldsymbol{E}}$ changes from 1 to -1, the electron is in the deceleration phase. In addition, when $\sin\phi_{\boldsymbol{B}}$ negative value, the electron is accelerated in the z-direction by the effect of $\boldsymbol{\beta}_\perp\times\boldsymbol{B}_{\rm in}$, while $\cos\phi_{\boldsymbol{B}}$ positive value, the electron is decelerated in the reverse direction. As shown in Figs.3.3 (b) to (g), the region I of the diagonal line is the acceleration phase in both perpendicular and parallel direction, and the region Ⅱ of gray hatching is

the deceleration phase in both perpendicular and parallel direction. In the acceleration phase, an increase of the Larmor radius and a decrease of the cyclotron frequency can be found with an increase of the kinetic energy as shown in Fig.3.3 (b), (e) and (f). This is because the kinetic energy is changed by the relativistic effect. Here, as shown in the following equation, the relativistic cyclotron frequency is represented by

$$\omega_{\mathrm{ce},\gamma} = \frac{\omega_{\mathrm{ce}}}{\gamma}. \tag{3.5}$$

Also, it can be seen that the electron has a linear motion with a constant velocity, but the motion to z-direction includes small oscillations due to the effect of $\boldsymbol{\beta}_{\perp} \times \boldsymbol{B}_{\mathrm{in}}$. In addition, regarding velocity and acceleration as shown in Fig.3.3 (c) and (d), the velocity in perpendicular direction is increased by the acceleration in same direction, while the velocity in parallel direction (z-direction) is also increased by acceleration in z-direction with positive value. The opposite motion happenes in the deceleration phase. At this time, since the electron is moving with relativistic velocity in the z-direction, the electron sees the RHCP wave with Doppler-shifted frequency ω_D (defined below), which is lower than the original frequency of the RHCP wave [2].

$$\omega_{\mathrm{D}} = \omega_E \sqrt{\frac{1-\beta_{\parallel}}{1+\beta_{\parallel}}} \tag{3.6}$$

where it is assumed that the electron has only z component. Eq.(3.6) describes the Doppler effect of light as seen from the reference frame of a particle (observer) which is traveling with a relativistic velocity. Fig.3.3 (e) green line shows the result of plotting eq.(3.6). As a result, it can be seen that the relativistic electron cyclotron frequency and the frequency of the RHCP wave seen from the reference frame of electron are satisfied with a relationship of $\omega_{\mathrm{ce},\gamma} \simeq \omega_D$. Such a system is called cyclotron auto-resonance acceleration and has been well studied by Kuramitsu *et al.* [3,4]. In other words, when a circularly polarized wave has the same polarization direction as the rotation direction of a charged particle, the electron can be almost always maintained in the resonance state.

In addition, it can be seen that the electron travels a few meters for a short period of time. It is possible to calculate the electron motion for a longer time, but it is inefficient to calculate the propagation of the electron up to several tens of meters in z-direction due to being restricted by the experimental device. In the experiment, the externally applied electromagnetic waves can be applied as continuous wave (CW) for at most a few minutes, thus the sufficient radiation intensity can be obtained if more than one group of electrons is injected into the wave with CW operation.

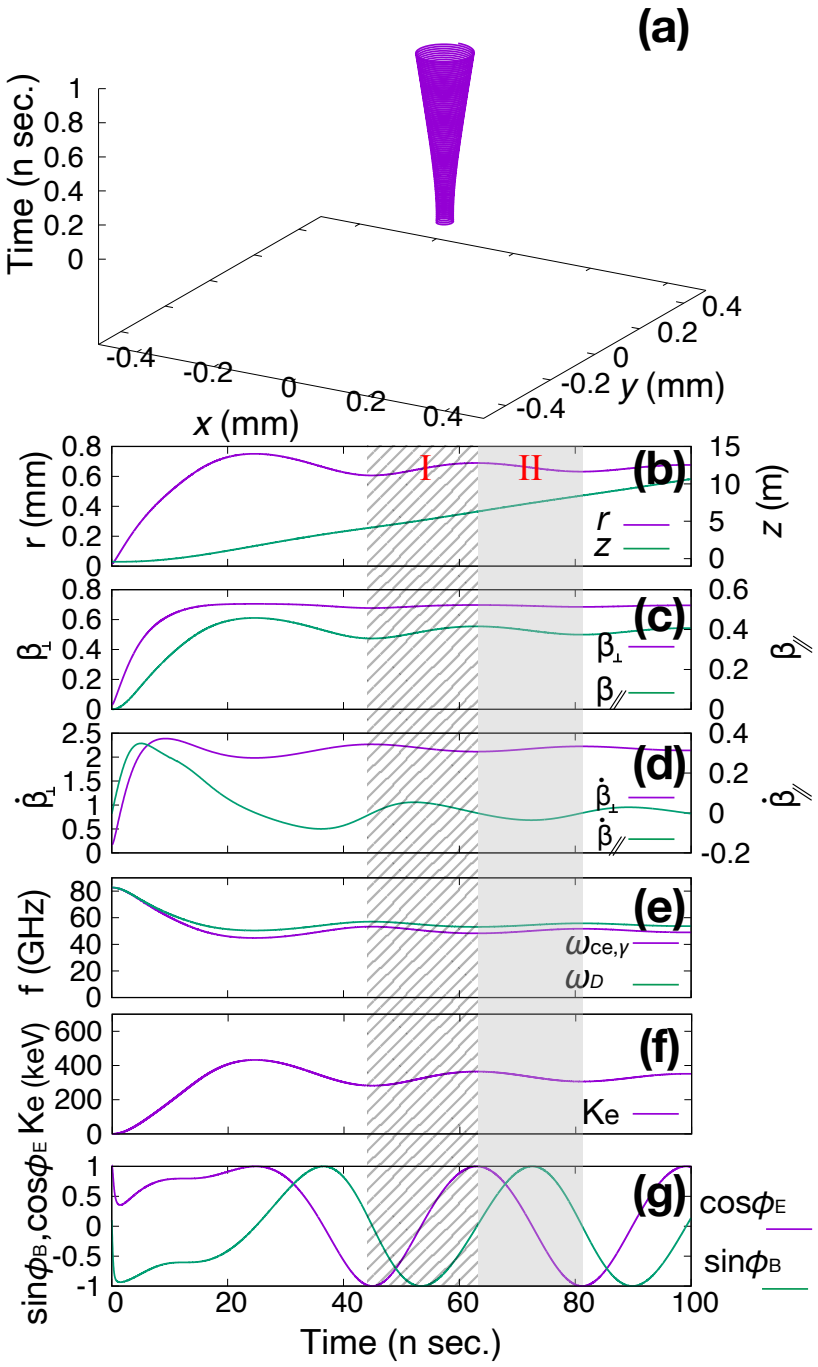

Figure 3.3: Trajectory information and some parameters. (a): Part of the electron trajectory when the RHCP wave is applied into an electron with cyclotron motion in static uniform magnetic field from the outside. (b)-(d): Trajectory information concerning positions, velocities, and accelerations. (e): Relativistic electron cyclotron frequency and Doppler-shifted frequency of RHCP wave seen from the reference frame of electron with relativistic velocity. (f): Kinetic energy of the electron. (g): Phase relationships between the acceleration of the electron in the x-y direction $\dot{\boldsymbol{\beta}}_\perp$and the electric field $\boldsymbol{E}_{\rm in}$, also between the velocity of the electron in the x-y direction $\boldsymbol{\beta}_\perp$ and the magnetic field $\boldsymbol{B}_{\rm in}$, which are defined by eq.(3.3) and eq.(3.4).

3.2.2 Regarding Application to Multi-electron System

As shown in Fig.3.3(g), it was found that electron travels in a magnetic field while repeatedly accelerating and decelerating under the effect of externally applied circularly polarized wave, except for the first irregular state. It can be seen from the eq.(2.26) that this period depends on the power of the electromagnetic wave. This is because if $\boldsymbol{E}_{\rm in}$ is larger, the effect of the second term on the right side of the eq.(2.26) can be relatively small. Fig.3.4 shows the change of frequency for $\cos\phi_{\boldsymbol{E}}$ and $\sin\phi_{\boldsymbol{B}}$ when the power of $\boldsymbol{E}_{\rm in}$ is changed from 100 kW to 1000 kW by 100 kW. As can be seen, the frequency of $\cos\phi_{\boldsymbol{E}}$ and $\sin\phi_{\boldsymbol{B}}$ gradually decreases as the power of the externally applied $\boldsymbol{E}_{\rm in}$ increases. Since the electron cyclotron period is $T_{\rm ce} = 12$ p sec. at the 2.954 T, it can be seen that the greater the power, the better the electron is trapped by the electric field. In addition, the spatial coherence of the electrons can be maintained by the effect of the externally applied wave, as shown in Fig.3.5. Because the electric field vectors of the injected beam have same directions at the given z plane, and if the beam is high power, each phase relationship between the electric field vector and the acceleration vector of the electron is the same everywhere. Thus, the spatial coherence of the electrons can be produced. This calculation is for an electron, but the same phenomena occur in each electron even in a multi-electron system. When a circularly polarized wave is applied to the multi-electron system with cyclotron motion in a uniform magnetic field, the direction of $\dot{\boldsymbol{\beta}}$ for each electron can have the same direction as the $\boldsymbol{E}_{\rm in}$. Thus, the coherent radiation can be obtained from a multi-electron system.

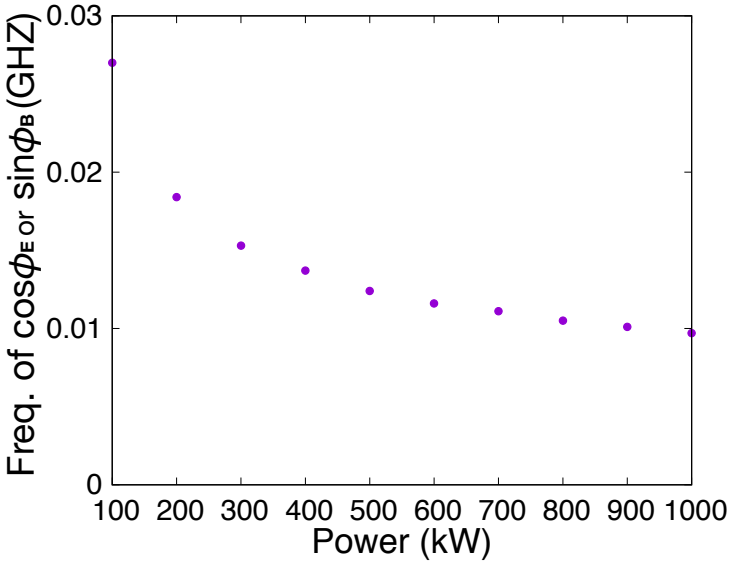

Figure 3.4: Change of frequency for $\cos\phi_{\boldsymbol{E}}$ and $\sin\phi_{\boldsymbol{B}}$ when the power of $\boldsymbol{E}_{\rm in}$ is changed from 100 kW to 1000 kW by 100 kW.

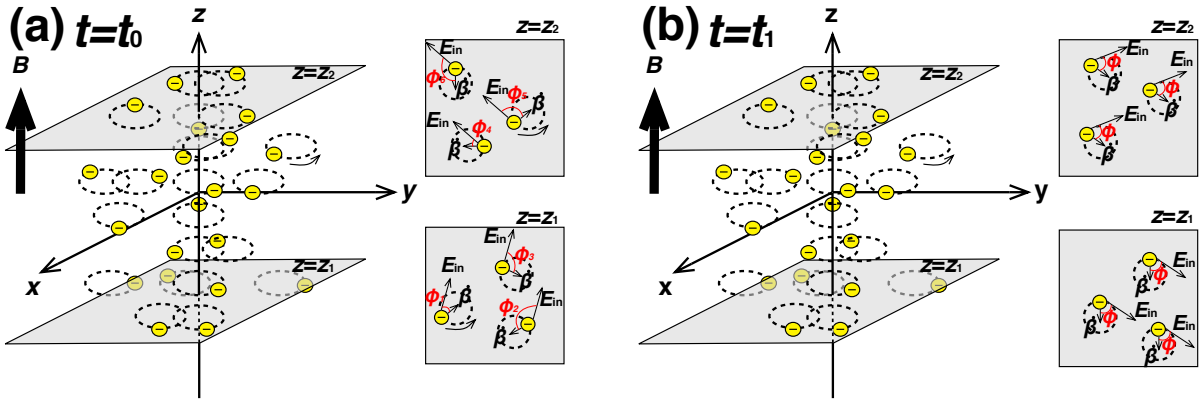

Figure 3.5: Spatial coherence of the electrons. If the injected beam is high power, each phase relationship between the electric field vector and the acceleration vector of the electron is the same at a given z plane.

3.2.3 Observation of the ECE with Helical Wavefront

In the previous subsection, we have obtained the trajectory information of electron when the circularly polarized wave is applied to the electron with cyclotron motion in a uniform magnetic field. Next, we will calculate the radiation using the trajectory information. The calculation was performed at the distance from the origin $|\boldsymbol{R}| = 15$ m, θ is changed from 0 deg. to 90 deg. by 10 deg., and ϕ is at 0 deg. By substituting the trajectory information into Liénard-Wiechert potential, we can calculate the radiation field. Fig.3.6 shows the time variation of the spectrum observed at each θ on $\phi = 0$. As was mentioned in Sec.3.1, the time step of radiation calculated by the Liénard-Wiechert potential is not the same considering the retarded time. Therefore, the time step of radiation is equalized by spline interpolation before performing FFT. Considering the retarded time, the radiation arrives around 50 n sec. As can be seen, only the fundamental radiation appears at $\theta = 0$, while higher harmonics appear at other θ. Since $\theta = 0$ corresponds to the optical axis, this suggests that higher harmonics do not have intensity on the optical axis, which is one of the characteristics of the radiation with a helical wavefront. It can also be seen that these spectra change with time. This is related to the Doppler effect in which electron travels to the observer with relativistic velocity while maintaining cyclotron motion. This will be discussed in the next subsection.

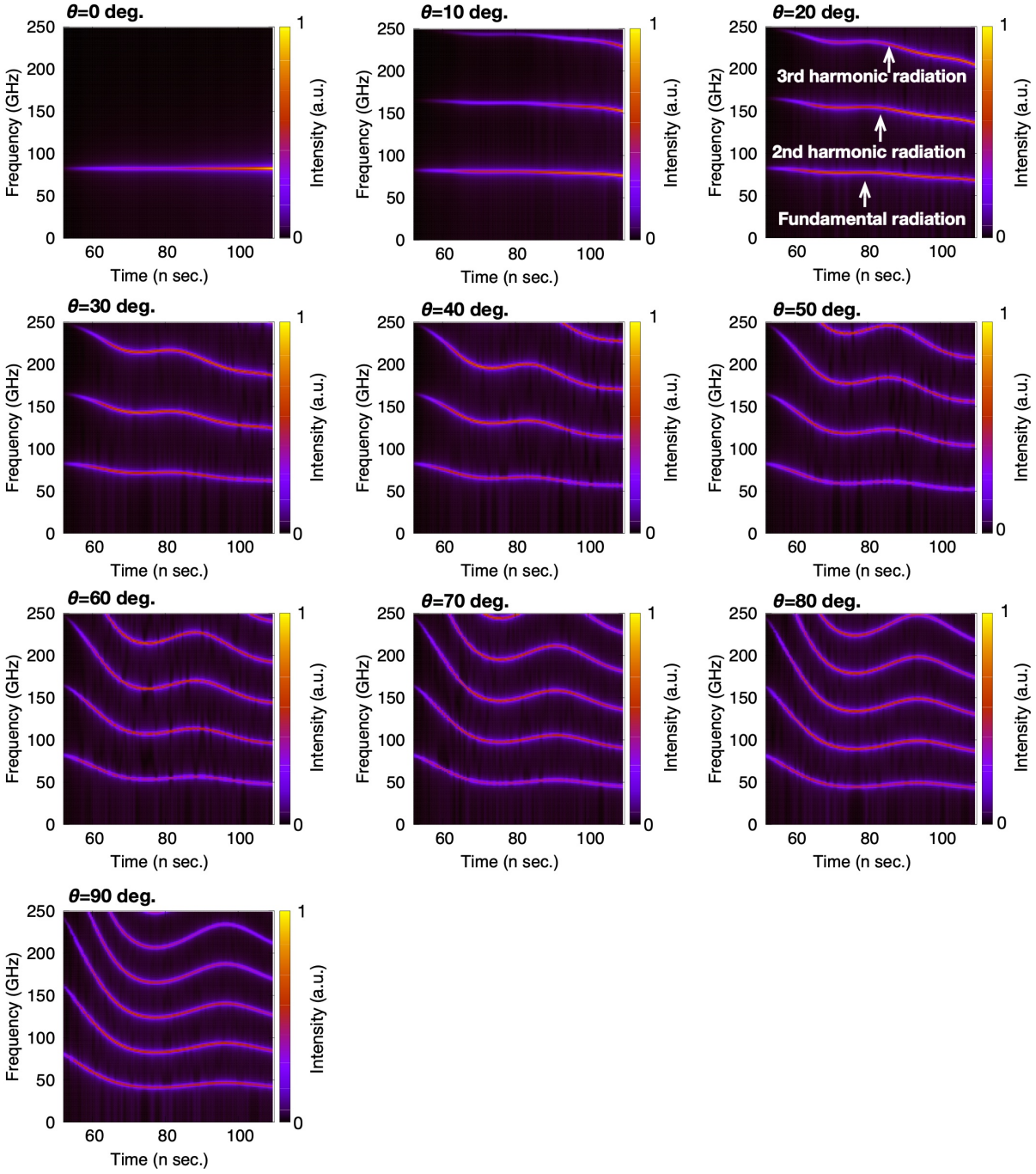

Figure 3.6: Time variation of the spectrum observed on the upper hemisphere at the distance from the origin $|\boldsymbol{R}| = 15$ m, each θ on $\phi = 0$.

3.2.4 Transverse Doppler Shift by Traveling with Relativistic Velocity in Cyclotron Motion

In the Fig.3.6, the radiation whose frequency changes with time is observed. This is related to the Doppler effect caused by electrons traveling with a relativistic velocity around the optical axis (z-axis). The Doppler effect depends on the positional relationship between the observer and the light source. The Doppler effect including the case where there is an observer in the transverse direction is given by the following equation.

$$\omega_{\mathrm{T,D}} = \frac{\omega_{\mathrm{ce},\gamma}}{\gamma_{\parallel}(1+\beta_{\parallel}\cos\alpha)} \tag{3.7}$$

where α is the angle between the line of sight of the observer and the propagation direction as shown in Fig.3.2. Here, it is assumed that $|\boldsymbol{r}| \ll |\boldsymbol{R}|$. When θ is small, the $\cos\alpha$ becomes negative, and the observer receives radiation with blue-shifted frequency larger than $\omega_{\mathrm{ce},\gamma}$. On the other hand, when θ is large, the $\cos\alpha$ becomes positive and the observer receives radiation with red-shifted frequency smaller than $\omega_{\mathrm{ce},\gamma}$. Fig.3.7 shows the result of plotting eq.(3.7). As can be seen, when θ is small, the blue-shifted frequency which is higher than $\omega_{\mathrm{ce},\gamma}$ (Fig.3.3(e)) is observed at the observer position. On the other hand, when θ is large, the red-shifted frequency which is lower than $\omega_{\mathrm{ce},\gamma}$ is observed at the observer position. That is, the time variation of the spectra in the Fig.3.6 can be explained by the transverse Doppler effect.

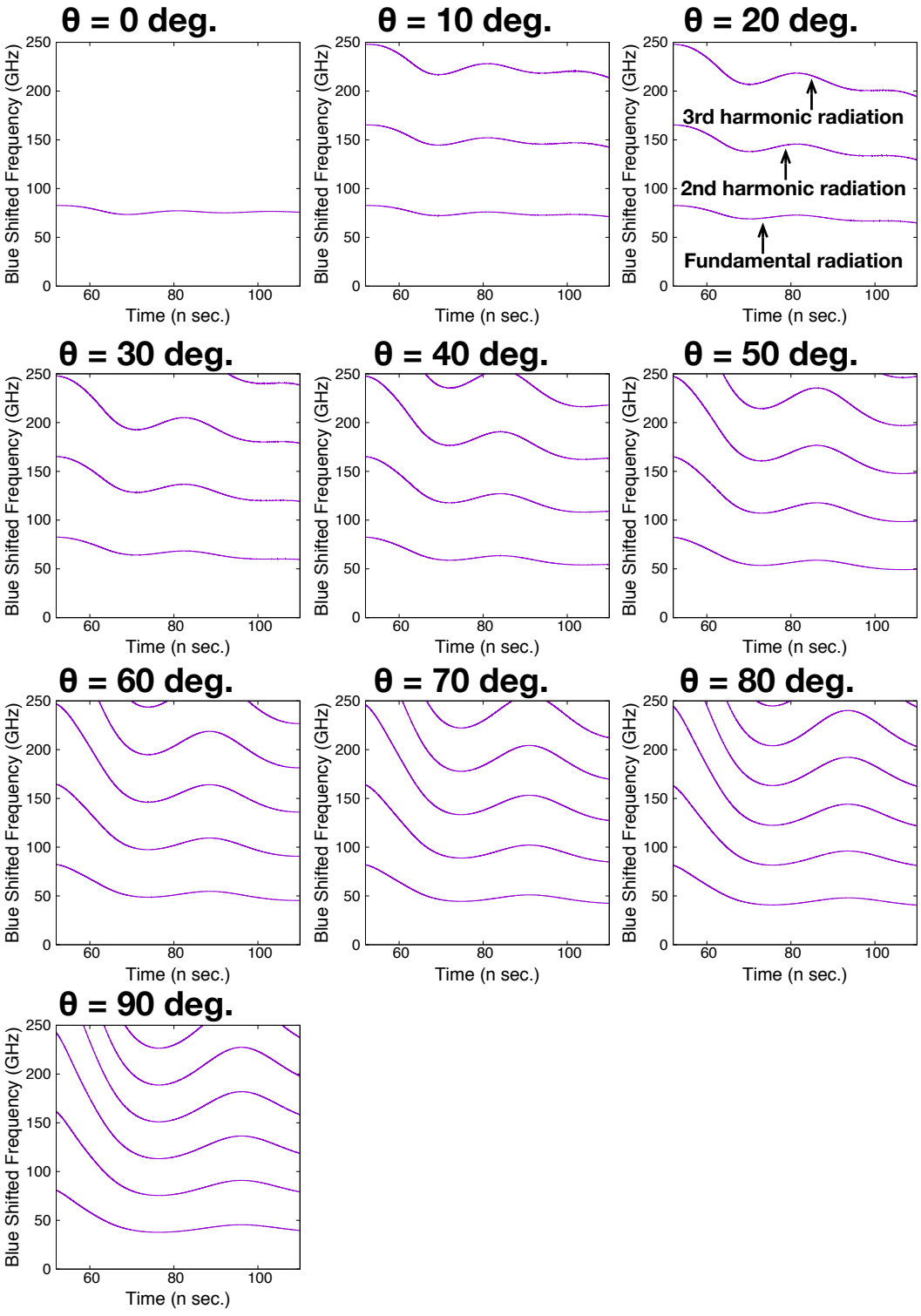

Figure 3.7: Time variation of the frequency calculated by eq.(3.7) observed at each θ. When θ is small, the $\cos\alpha$ becomes negative, and the observer receives radiation with blue-shifted frequency larger than $\omega_{\mathrm{ce},\gamma}$. On the other hand, when θ is large, the $\cos\alpha$ becomes positive and the observer receives radiation with red-shifted frequency smaller than $\omega_{\mathrm{ce},\gamma}$.

3.2.5 Phase Difference Observed at Two Spatial Points

In the previous subsection, we obtained the result that the intensity of higher harmonics does not exist on the optical axis, which is one of the characteristics of the radiation with helical wavefront. In order to demonstrate that this radiation has helical wavefront as well as the donut-shaped intensity distribution, we calculate the phase difference of the measured radiation at two spacial points. Since the beam with helical wavefront has spatial phase structure, we can detect the phase difference between two spatial points. Thus, we compare the phase of the radiation observed between $\phi = 0$ deg. and $\phi = 90$ deg. or $\phi = 180$ deg. If the observed radiation has helical wavefront, that radiation should have a phase difference of $90(n-1)$ deg. or $180(n-1)$ deg., where n is the harmonic number. To find the phase difference between two spatial points, we use the following equation:

$$f_{\mathrm{ph}}(\phi) \equiv \cos\left(\arg.\left(\frac{\mathrm{E}_{\phi}}{\mathrm{E}_{\phi=0}}\right)\right). \tag{3.8}$$

Fig.3.8 and Fig.3.9 show the cosine value of the phase difference calculated by eq.(3.8). As can be seen in both figures, because the spatial location between $\phi = 0$ deg. and $\phi = 90$ deg. at $\theta = 0$ deg. or between $\phi = 0$ deg. and $\phi = 180$ deg. at $\theta = 0$ deg. represents a same location, the phase difference is zero, that is, the cosine value is 1. In other θ, it can be seen that the cosine value also changes along the spectrum of fundamental and harmonics radiation. In the case of fundamental radiation, it can be seen in both figures that the cosine value is 1 at all θ. That is, the phase difference is zero in fundamental radiation. This indicates that the fundamental radiation is merely a Gaussian beam with a planar or spherical equiphase front. In the case of second harmonic radiation, it can be seen that when $f_{\mathrm{ph}}(90)$, which is shown in Fig.3.8, the cosine value is 0 at all θ except for $\theta = 0$ deg., which indicates that the phase difference is 90 deg., while when $f_{\mathrm{ph}}(180)$, which is shown in Fig.3.9, the cosine value is -1 at all θ except for $\theta = 0$ deg., which indicates that the phase difference is 180 deg. That is, the phase in second harmonic radiation changes 360 deg. around the optical axis. In addition, in the case of third harmonic radiation, when $f_{\mathrm{ph}}(90)$, which is shown in Fig.3.8, the cosine value of the third harmonic is -1, which indicates that there is a phase difference of 180 deg., while when $f_{\mathrm{ph}}(180)$, which is shown in Fig.3.9, the cosine value is 1 again at all θ except for $\theta = 0$ deg., which indicates that the phase difference is 360 deg. That is, the phase in third harmonic radiation changes by 720 deg. around the optical axis. In this way, it was shown that the harmonics radiation has the phase difference with $90(n-1)$ between $\phi = 0$ deg. and $\phi = 90$ deg. or $180(n-1)$ between $\phi = 0$ deg. and $\phi = 180$ deg. Therefore, considering the discussion in the previous result where higher harmonics do not appear on the optical axis, the fundamental radiation has no helical wavefront, but only the higher harmonics have a helical wavefront.

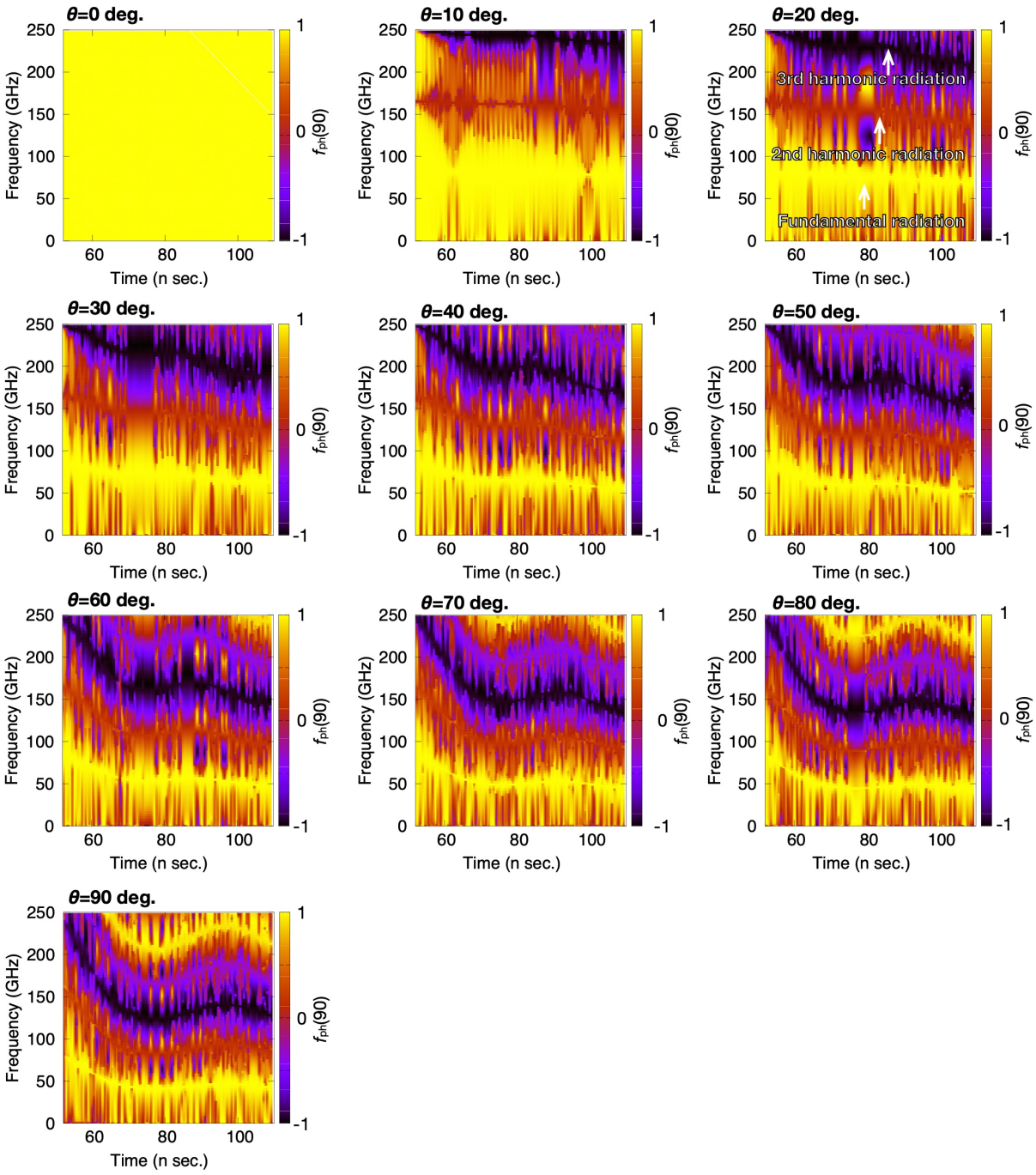

Figure 3.8: Time variation of the cosine value of the phase difference between $\phi = 0$ deg. and $\phi = 90$ deg. calculated by eq.(3.8).

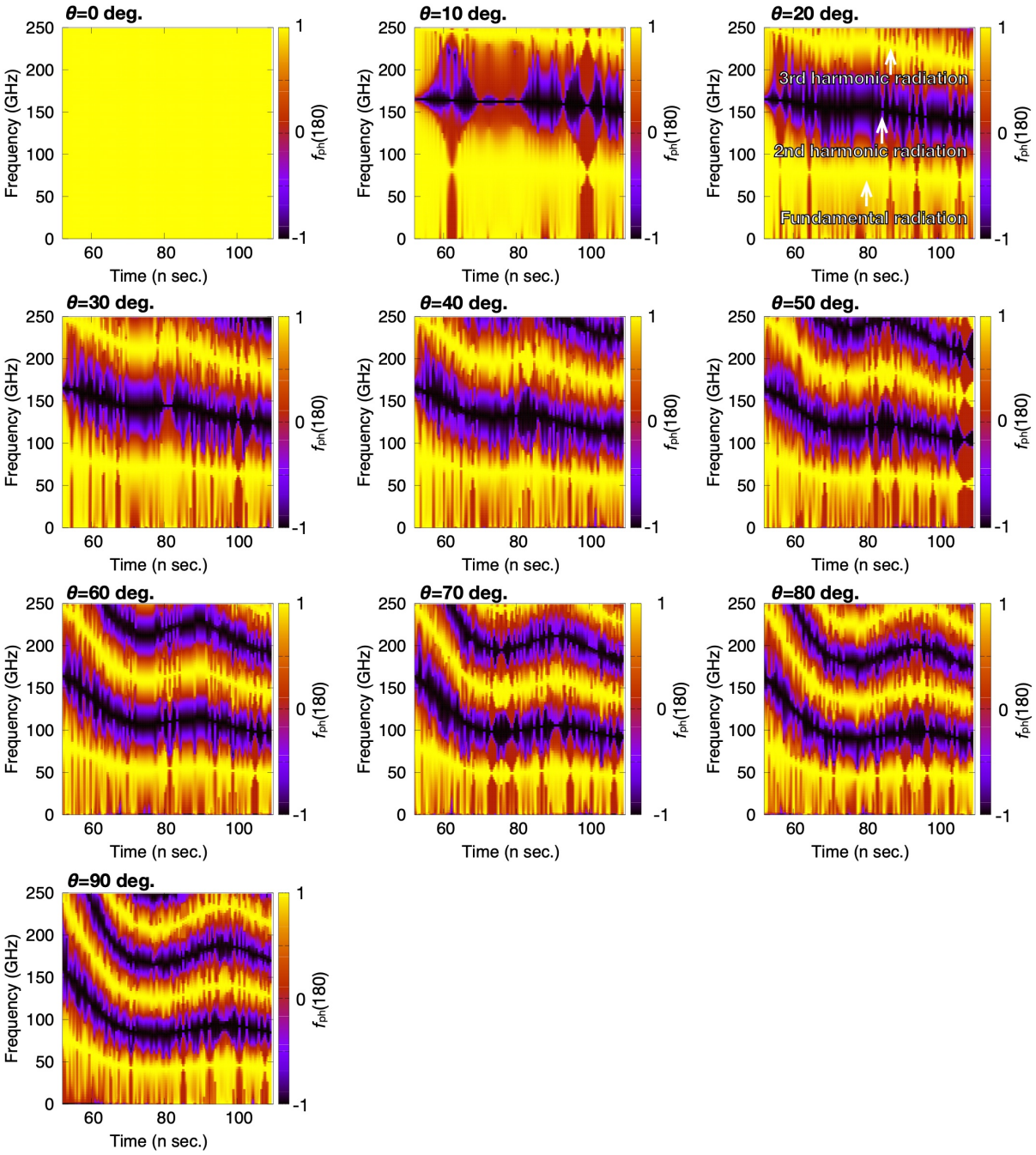

Figure 3.9: Time variation of the cosine value of the phase difference between $\phi = 0$ deg. and $\phi = 180$ deg. calculated by eq.(3.8).

3.2.6 Intensity Distribution and Phase Structure

In this subsection, the intensity distribution and the phase structure of the fundamental and the second harmonic radiation observed on the upper hemisphere at a given time are shown. Fig.3.10 shows the intensity distribution and the phase structure of the fundamental radiation and second harmonic radiation at $t = 70.4$ n sec. Fig.3.10 is the inverse FFT results of the Fig.3.11, which is observed from 70 n sec. The left figure shows the fundamental radiation, and the right figure shows the second harmonics radiation. In both figures, the calculated radiation fields are projected on the x-y plane. The arrows indicate the direction of the electric field at a given time and place, and the color bars indicate the power of the electric field, which is normalized by the maximum value. The powers are time-averaged. As can be seen, in the left figure, the intensity profile of the electric field is Gaussian-shaped with an intensity peak on the beam axis. The electric field is circularly polarized in the paraxial area and is facing the same direction at the same polar angle. This beam is just a Gaussian beam, thus, this is not characteristic of the vortex beam. However, due to the Doppler effect described in the previous subsection, the radiation frequency depends on the polar angle θ. Next in the right figure, the intensity profile of the electric field is donut-shaped with no intensity on the beam axis, and although the electric field is circularly polarized in the paraxial area, the direction is reversed at the symmetric point with respect to the beam axis. However, due to the Doppler effect mentioned above, the radiation frequency depends on the polar angle θ. These are characteristics of the vortex beam. Thus, we have successfully calculated the vortex radiation from cyclotron motion.

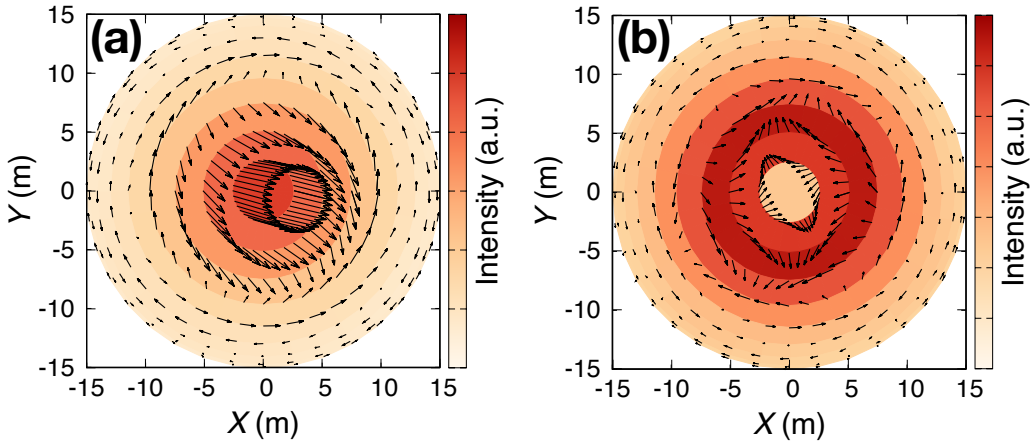

Figure 3.10: Intensity distribution and phase structure of the fundamental radiation and second harmonic radiation at $t = 70.4$ n sec. Both figures are projected on the x-y plane. The arrows indicate the direction of the electric field at a given time and place, and the color bars indicate the power of the electric field, which is normalized by the maximum value. The power is time-averaged.

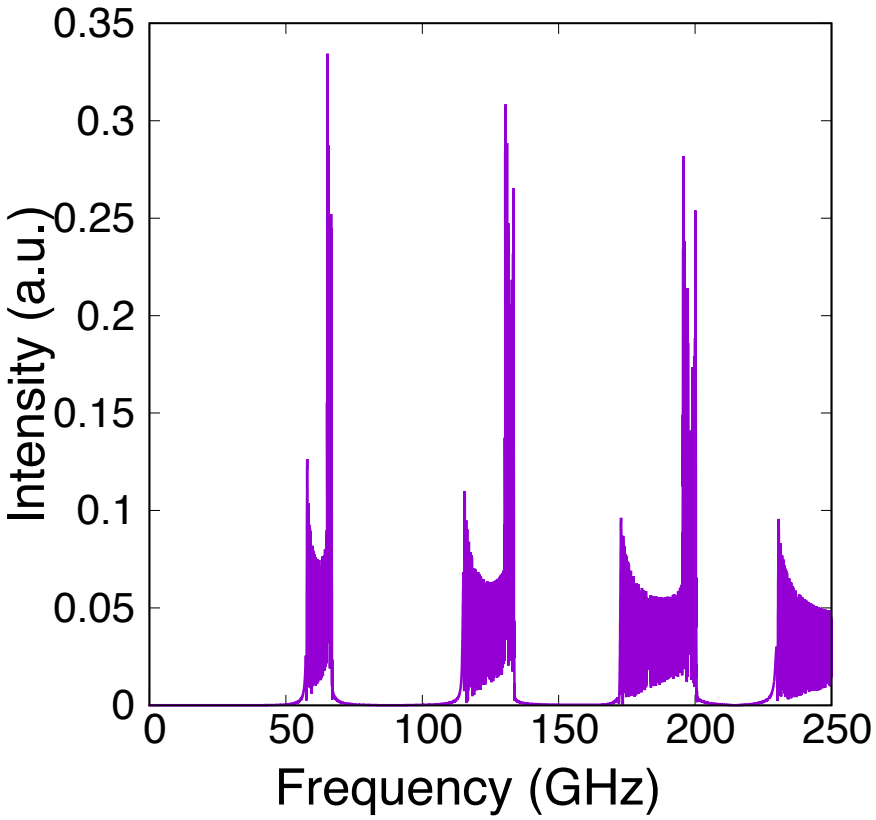

Figure 3.11: FFT results of the Fig.3.11, which is observed from 70 n sec.

3.3 In the Case of a Magnetic Mirror Field

In this subsection, we calculate the trajectory information of an electron with cyclotron motion in the mirror field controlled by the RHCP wave, and then calculate the radiation from such electron. The magnetic mirror field to be externally applied is generated by a torus coil with a radius of 0.13 m as shown in the Fig.3.12. The magnetic field strength on the optical axis at the origin is set to resonant magnetic field strength which corresponds to Doppler-shifted frequency of RHCP wave seen from the reference frame of the electron. In this research, we calculate the radiation on the two cases of the magnetic field strength. One is 2.286 T, the other is 2.909 T. The former is resonant field strength which corresponds to Doppler-shifted frequency of the RHCP wave seen from the reference frame of the electron with parallel velocity which corresponds to extraction voltage of 18 keV. While the latter is resonant field strength which corresponds to Doppler-shifted frequency of the RHCP wave seen from the reference frame of the electron with parallel velocity which corresponds to extraction voltage of 0.1 keV. The perpendicular velocities (momentums) have the velocity as thermal fluctuation which corresponds to 0.1 keV in both cases. Note that when the velocity in the z-direction is slow, an electron is reflected at the mirror point. Thus, it is necessary to give the initial velocity in z-direction. As will be explained in the next chapter, this magnetic mirror field is similar to the magnetic field configuration used in the experiment. The RHCP wave applied from the outside is the same as in the previous section, and has 82.7 GHz, 100 kW, and the waist size of 30 mm at the origin. And the electron is injected from $z = -415$ mm. In table 3.2, the initial condition of the electron, beam parameters, and information related to the magnetic field are listed.

3.3.1 Electron Trajectory in the Electromagnetic Wave

Fig.3.13 shows the trajectory information and some parameters of the electron when the magnetic field is set to 2.286 T, while Fig.3.14 shows the trajectory information and some parameters of the electron when the magnetic field is set to 2.909 T.

In the Fig.3.13, it can be seen as shown in Fig.3.13 (a) and (b) purple line that the electron travels along the magnetic mirror field, and the Larmor radius decreases as the magnetic field increases (Fig.3.13 (e)). However, it can be seen that the Larmor radius suddenly increases just after 5 n sec. This is because the electron passes through the resonance magnetic field as shown in Fig.3.13 (f). Note again that the $\omega_{\mathrm{ce},\gamma}$ is represented by the relativistic electron cyclotron frequency along the electron trajectory with magnetic field as shown in Fig.3.13 (e), while the ω_{D} is represented by the Doppler-shifted frequency of the externally applied RHCP wave seen from the reference frame of the electron. The resonance happens when these frequencies become the same. As shown in Fig.3.13 (g), the kinetic energy of the electron spikes when the electron passes through the resonance field. Meanwhile, the velocities and the accelerations in perpendicular direction and

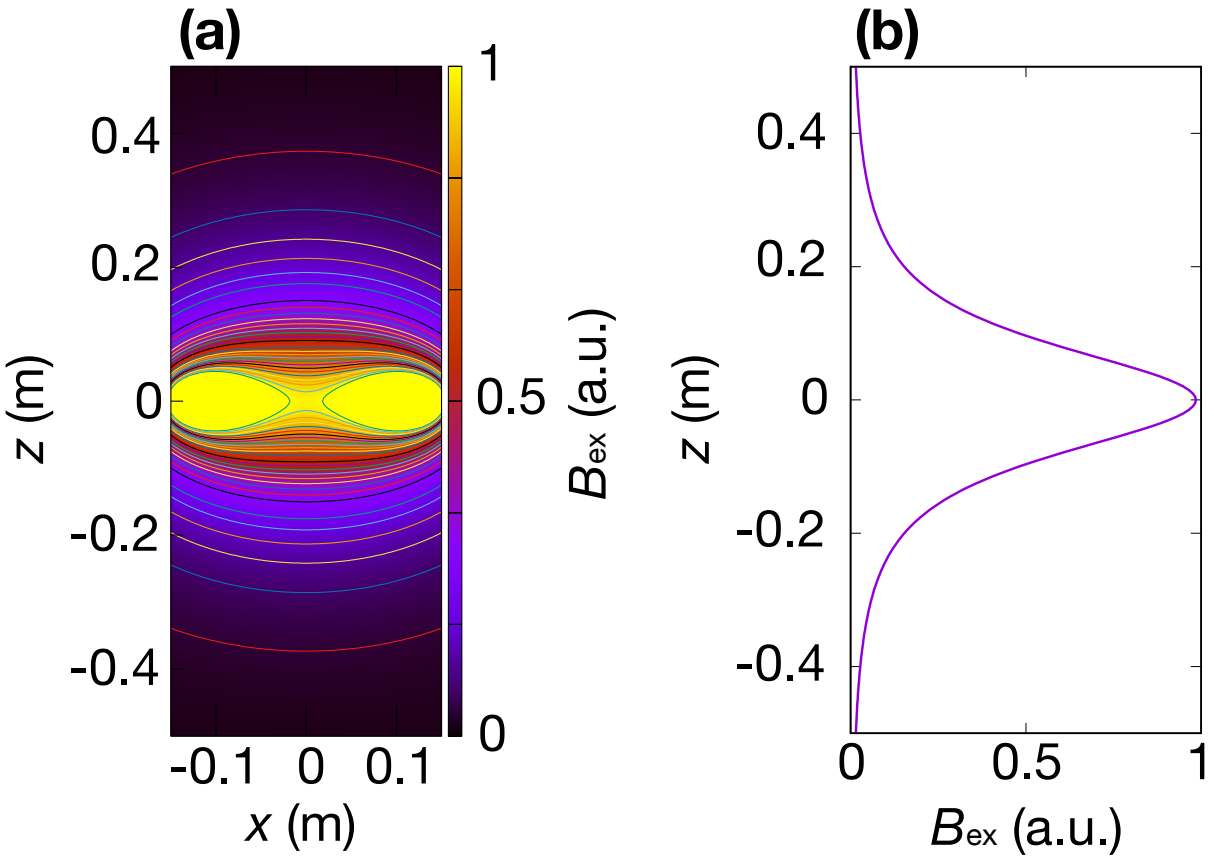

Figure 3.12: Externally applied magnetic mirror field structure used by the calculation with a normalized magnetic field strength by the maximum value on the optical axis at the origin. (a): Spatial distribution on x-z plane. (b): Spatial distribution on the optical axis.

parallel direction also spike as shown in Fig.3.13 (c) and (d). After passing through the resonance field, in the velocities it can be seen that the perpendicular velocity is gradually decreasing with time, while the parallel velocity is gradually increasing with time. This is because the magnetic moment must be conserved in the magnetic mirror field. Following this phenomenon, the accelerations increase/decrease with time. Note that although the acceleration in z-direction appears not to increase, the acceleration is increased averagely. However, in the case of larger velocity in z-direction, the duration time for interaction where the Doppler-shifted frequency of the RHCP wave seen from the reference frame of the electron and the electron cyclotron frequency coincide with each other is very short, thus the resonance time is also short. That is, the energy gain is not large.

While in the Fig.3.14, it can be seen as shown in Fig.3.13 (a) and (b) purple line that the electron travels along the magnetic mirror field, and the Larmor radius decreases

Initial Conditions			
Position	x	0 mm	
	y	0 mm	
	z	-415 mm	
Energy	18 keV in z-direction		0.1 keV in z-direction
Momentum	Thermal fluctuation in x-y direction		
Beam Parameters			
Frequency	82.7 GHz		
Power	100 kW		
Waist size	30 mm		
Polarization	RHCP wave		
Others			
Magnetic field	Mirror static 2.286 T at origin		Mirror static 2.909 T at origin
Calculation step	150 f sec.		

Table 3.2: Initial conditions of the electron with cyclotron motion in the magnetic mirror field, beam parameters applied from the outside, and some parameters.

as the magnetic field increases (Fig.3.14 (e)) as well. However, it can be seen that the Larmor radius suddenly increases just after 68 n sec., and the tendency is much greater than the previous case. This is because the initial energy in z-direction is small and the duration time for resonance is long enough. As shown in Fig.3.14 (f), it can be seen that the resonance time which is satisfied with $\omega_{\mathrm{ce},\gamma} = \omega_{\mathrm{D}}$ is maintained for a few n sec. Meanwhile, the kinetic energy increases sharply by the resonance acceleration, and the cyclotron frequency of the electron decreases on the other hand (Fig.3.14 (f) purple line). Also, the frequency of the externally applied RHCP wave seen from the reference frame of the electron is decreased as well due to increasing the velocity in z-direction. In the case of low energy of electron in z-direction, the kinetic energy of the electron can be increased effectively when the magnetic field strength is set to resonance one because the resonance state can be maintained continuously. The tendency of time change for velocities and the accelerations are the same with the previous case.

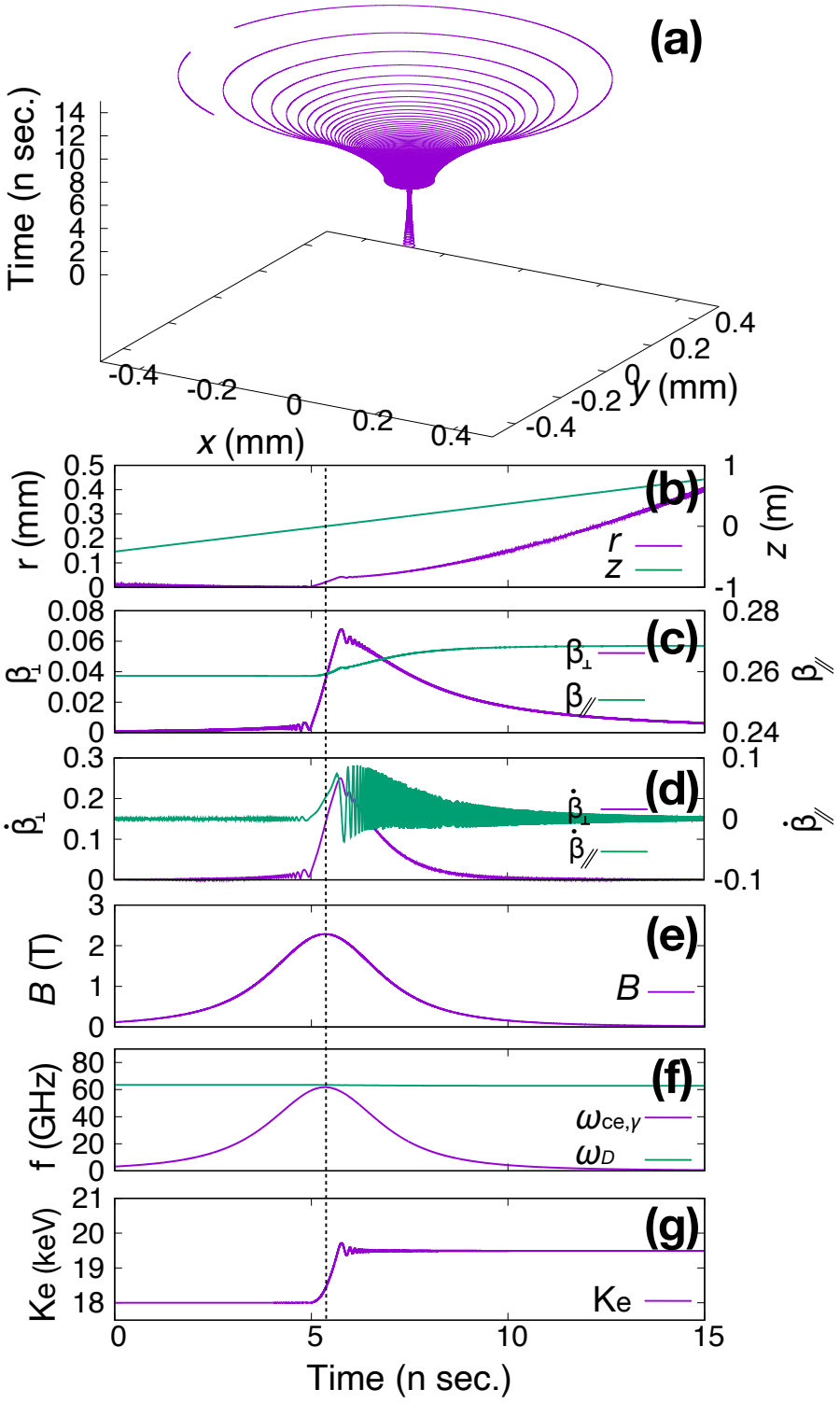

Figure 3.13: Trajectory information and some parameters when the magnetic field is set to 2.286 T and the energy in z-direction has 18 keV. (a): Electron trajectory (b)-(d): Trajectory information concerning positions, velocities, and accelerations. (e): The magnetic field strength along the electron trajectory. (f): Electron cyclotron frequency along the electron trajectory. (g): Kinetic energy of the electron.

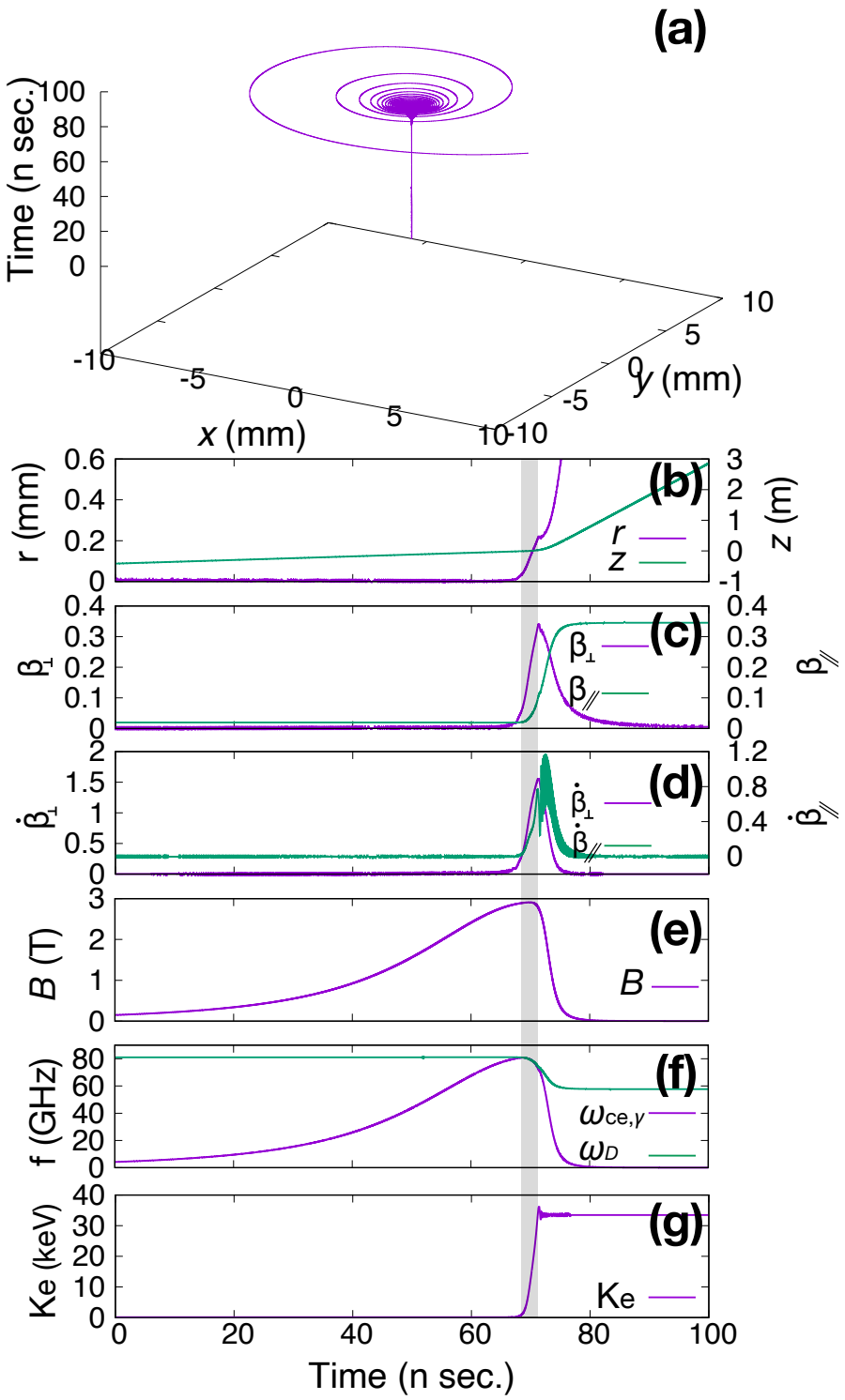

Figure 3.14: Trajectory information and some parameters when the magnetic field is set to 2.909 T and the energy in z-direction has 0.1 keV. (a): Electron trajectory (b)-(d): Trajectory information concerning positions, velocities, and accelerations. (e): The magnetic field strength along the electron trajectory. (f): Electron cyclotron frequency along the electron trajectory. (g): Kinetic energy of the electron.

3.3.2 Observation of the ECE with Helical Wavefront

In the previous subsection, we obtained the trajectory information of electron when RHCP wave is applied to the electron with cyclotron motion in the magnetic mirror field, and then the radiation field can be calculated by using the trajectory information. In this calculation, the radiation will be observed at the distance from the origin $|\boldsymbol{R}| = 3$ m, θ is changed from 0 deg. to 90 deg. by 10 deg., and ϕ is at 0 deg. By substituting the trajectory information into Liénard-Wiechert potential, we can calculate the radiation field.

Fig.3.15 shows the time variation of the spectrum observed at each θ on $\phi = 0$. These results were also equalized by spline interpolation before doing FFT. Considering the retarded time, the radiation arrives to observer around 10 n sec. In the common points in every θ, the spectrum with a focus on 82.7 GHz appears. This is because the electron has trochoidal motion by the effect of externally applied RHCP wave in the weaker magnetic field. That is, although the electron has the cyclotron motion overall, the cyclotron motion is locally controlled by the RHCP wave because the acceleration direction of the electron is mainly decided by the first term on eq.(2.27) in the weaker magnetic field. In addition, it can be seen that many spectra with gap of 10 GHz appear. This is because of the effect of zero padding in the FFT. To obtain the time variation of these spectra, the zero padding is carried out before FFT in order to obtain the high frequency resolution. Each time step is composed of 2^{21} data points, and the zero padding is carried out so that the data points become 2^{24} points. Also, in order to connect smoothly between calculated data points and the padded zero, the window function called Blackman window is multiplied. However, since the connection is not perfectly smooth, many spectra with gap of 10 GHz appeared. That is, these spectra are meaningless physically. In addition, the spectra intensity are measured by log scale for emphasizing the spectra lines.

As can be seen, only the fundamental radiation appears at $\theta = 0$, while higher harmonics appear at other θ as well as in the case of the uniform magnetic field. Since $\theta = 0$ corresponds to the optical axis, this suggests that higher harmonics do not have intensity on the optical axis, which is one of the characteristics of the radiation with a helical wavefront. It can also be seen that these spectra peaks decrease with increase of θ. This is also related to the Doppler effect in which electron travels to the observer with relativistic velocity while maintaining cyclotron motion. This will be discussed in the next subsection.

While in the Fig.3.16, the spectrum with 82.7 GHz also appears due to the same reason as the previous case, while the spectra that appeared caused by FFT did not appear. Because the calculation time by the resonance is longer than the previous case, and the high frequency resolution can be obtained without zero padding.

As can be seen, the characteristics of this radiation spectra are basically the same as the previous case. Only the fundamental radiation appears at $\theta = 0$, while higher harmonics also appear around the resonance area at other θ.

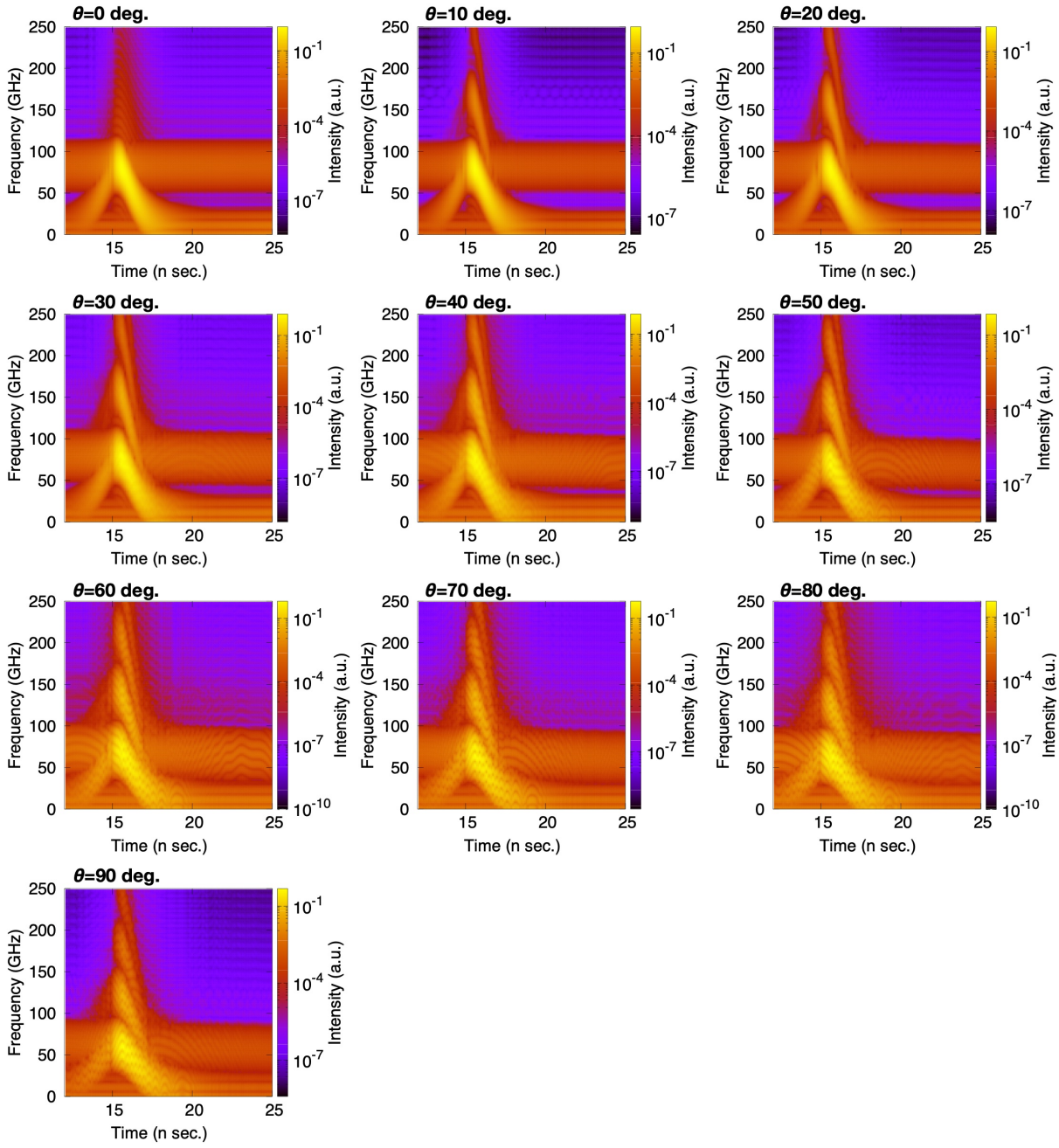

Figure 3.15: Time variation of the spectrum observed on the upper hemisphere at the distance from the origin $|\boldsymbol{R}| = 3$ m, each θ on $\phi = 0$ when the magnetic field is set to 2.286 T and the energy in z-direction has 18 keV. The spectra intensity are measured by log scale.

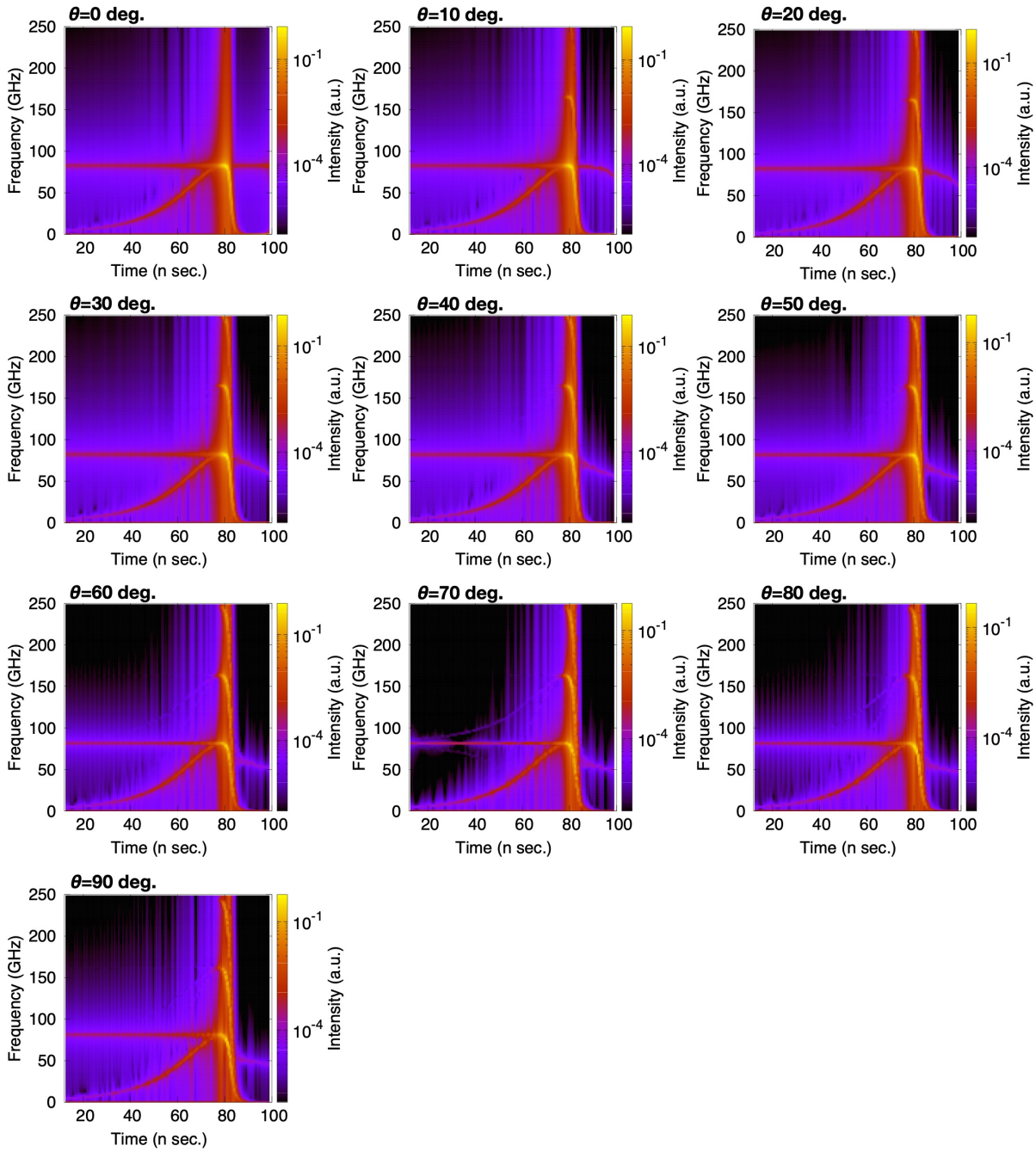

Figure 3.16: Time variation of the spectrum observed on the upper hemisphere at the distance from the origin $|\boldsymbol{R}| = 3$ m, each θ on $\phi = 0$ when the magnetic field is set to 2.909 T and the energy in z-direction has 0.1 keV. The spectra intensity are measured by log scale.

3.3.3 Transverse Doppler Shift by Traveling with Relativistic Velocity in Cyclotron Motion

Fig.3.17 shows the time variation for the Doppler-shifted frequency calculated by eq.(3.7) observed on the upper hemisphere when the magnetic field is set to 2.286 T and the electron has velocity in z-direction that corresponds to 18 keV. In this case, the electron has the relativistic velocity in z-direction, and the observer located on the upper hemisphere receives the Doppler-shifted radiation frequency. As can be seen when θ is small, the observer receives radiation with blue-shifted frequency larger than $\omega_{\mathrm{ce},\gamma}$. On the other hand, when θ is large the observer receives radiation with red-shifted frequency smaller than $\omega_{\mathrm{ce},\gamma}$.

While as shown in Fig.3.18, the observer located on the upper hemisphere does not receive the Doppler-shifted radiation frequency. This is because the electron has no relativistic velocity in z-direction due to low extraction voltage of 0.1 keV.

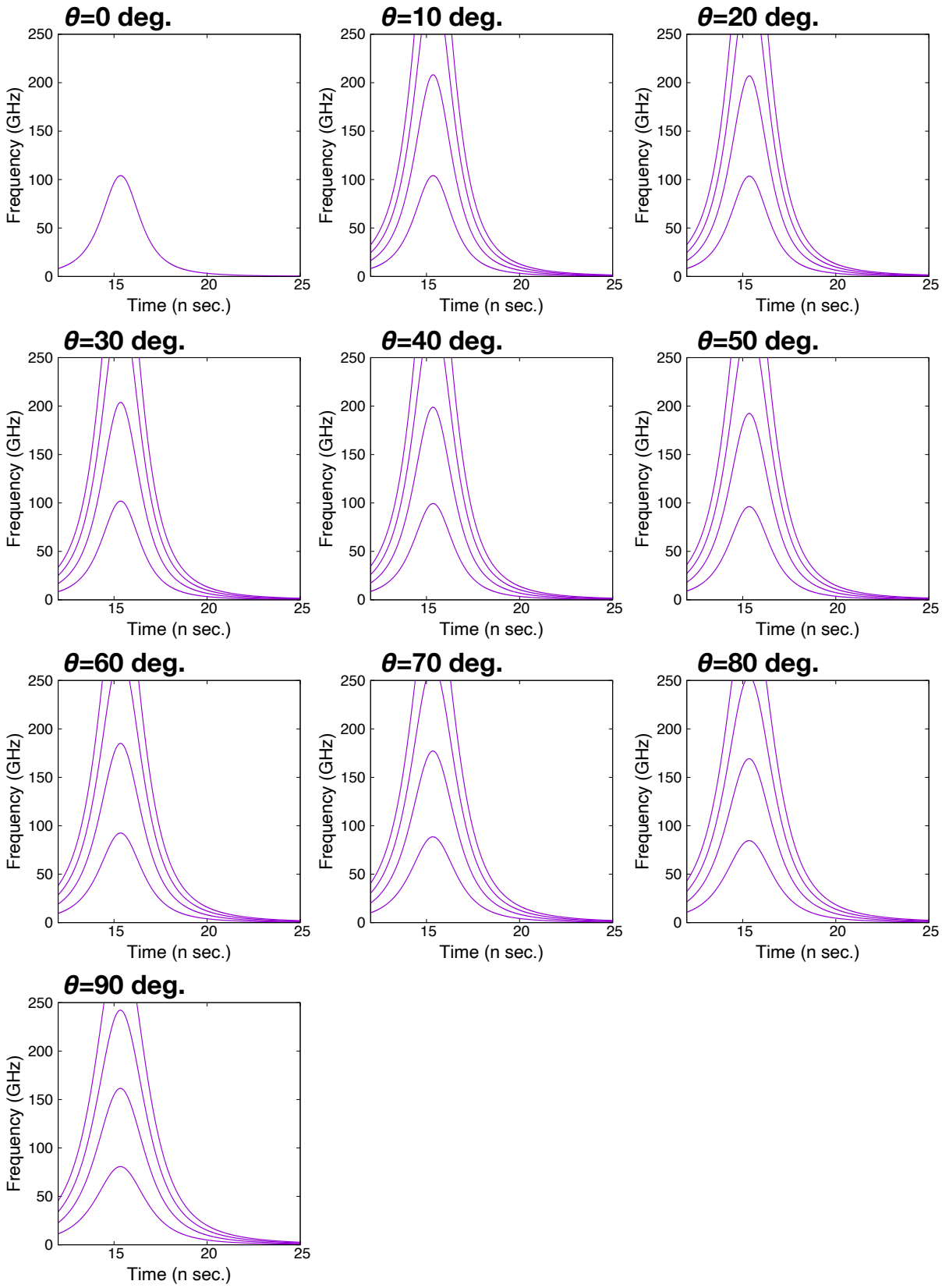

Figure 3.17: Time variation of the frequency calculated by eq.(3.7) observed at each θ when the magnetic field is set to 2.286 T and the energy in z-direction has 18 keV.

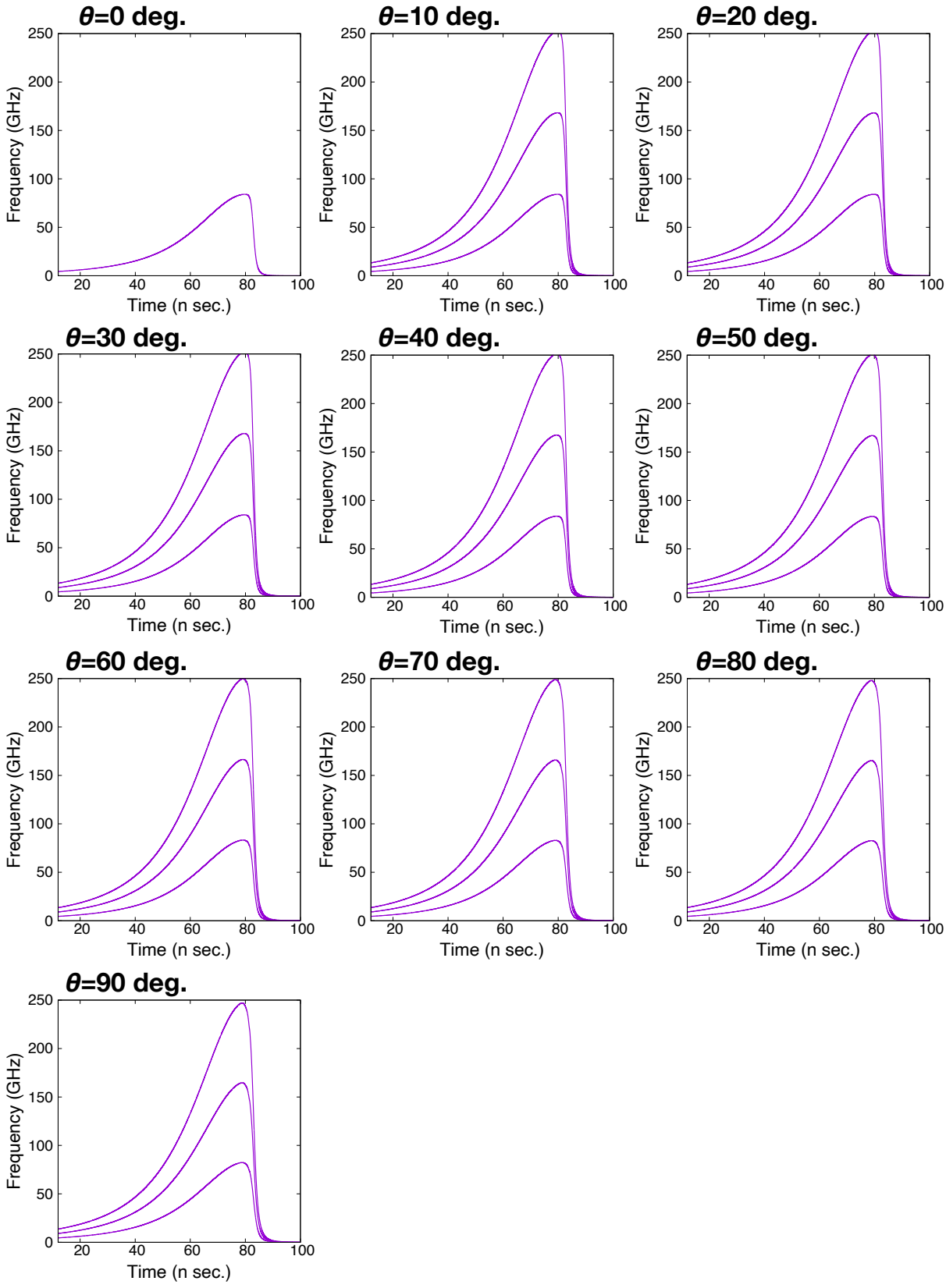

Figure 3.18: Time variation of the frequency calculated by eq.(3.7) observed at each θ when the magnetic field is set to 2.909 T and the energy in z-direction has 0.1 keV.

3.3.4 Phase Difference Observed at Two Spatial Points

In the previous subsection, we obtained the result that the intensity of higher harmonics does not exist on the optical axis even in the radiation from the magnetic mirror field. In order to demonstrate that this radiation has helical wavefront as well as the donut-shaped intensity distribution, we calculate the phase difference of the measured radiation at two spacial points between $\phi = 0$ deg. and $\phi = 90$ deg. or $\phi = 180$ deg. by using eq.(3.8).

Fig.3.19 and Fig.3.20 show the cosine value of the phase difference calculated by eq.(3.8). Note that the phase differences with the frequency gap of 10 GHz appears due to zero padding before FFT. Therefore, the phase differences have no physical meaning. In addition, phase difference with cosine value 1 appears around 82.7 GHz. This is because the electron has trochoidal motion by the effect of externally applied RHCP wave in the weaker magnetic field. And the fundamental radiation is just a beam with plainer or spherical phase front. The intensity is dominant before passing through the resonance field, but the main radiation is much more dominant before resonance acceleration. As can be seen in both figures, because the spatial location between $\phi = 0$ deg. and $\phi = 90$ deg. at $\theta = 0$ deg. or between $\phi = 0$ deg. and $\phi = 180$ deg. at $\theta = 0$ deg. represents a same location, the phase difference is zero, that is, the cosine value is 1. In other θ, it can be seen that the cosine value also changes along the spectrum of fundamental and harmonics radiation. In the case of fundamental radiation, it can be seen in both figures that the cosine value is 1 at all θ. That is, the phase difference is zero in fundamental radiation. This indicates that the fundamental radiation is just a Gaussian beam with a planar or spherical equiphase front. In the case of second harmonic radiation, it can be seen that when $f_{\mathrm{ph}}(90)$, which is shown in Fig.3.19, the cosine value is 0 at all θ except for $\theta = 0$ deg., which indicates that the phase difference is 90 deg., while when $f_{\mathrm{ph}}(180)$, which is shown in Fig.3.20, the cosine value is -1 at all θ except for $\theta = 0$ deg., which indicates that the phase difference is 180 deg. That is, the phase in second harmonic radiation changes 360 deg. around the optical axis. In addition, in the case of third harmonic radiation, when $f_{\mathrm{ph}}(90)$, which is shown in Fig.3.19, the cosine value of the third harmonic is -1, which indicates that there is a phase difference of 180 deg., while when $f_{\mathrm{ph}}(180)$, which is shown in Fig.3.20, the cosine value is 1 again at all θ except for $\theta = 0$ deg., which indicates that the phase difference is 360 deg. That is, the phase in third harmonic radiation changes by 720 deg. around the optical axis. In this way, it was shown that the harmonics radiation has the phase difference with $90(n-1)$ between $\phi = 0$ deg. and $\phi = 90$ deg. or $180(n-1)$ between $\phi = 0$ deg. and $\phi = 180$ deg.

Fig.3.21 and Fig.3.22 also show the cosine value of the phase difference calculated by eq.(3.8). In these cases, the vortex property clearly appears near the resonance field. That is, in the case of fundamental radiation, it can be seen in both figures that the cosine value is 1 at all θ. That is, the phase difference is zero in fundamental radiation. This indicates that the fundamental radiation is just a Gaussian beam with a planar or spherical equiphase front. In the case of second harmonic radiation, it can be seen that when

$f_{\rm ph}(90)$, which is shown in Fig.3.21, the cosine value is 0 at all θ except for $\theta = 0$ deg., which indicates that the phase difference is 90 deg., while when $f_{\rm ph}(180)$, which is shown in Fig.3.22, the cosine value is -1 at all θ except for $\theta = 0$ deg., which indicates that the phase difference is 180 deg. That is, the phase in second harmonic radiation changes 360 deg. around the optical axis. In addition, in the case of third harmonic radiation, when $f_{\rm ph}(90)$, which is shown in Fig.3.21, the cosine value of the third harmonic is -1, which indicates that there is a phase difference of 180 deg., while when $f_{\rm ph}(180)$, which is shown in Fig.3.22, the cosine value is 1 again at all θ except for $\theta = 0$ deg., which indicates that the phase difference is 360 deg. That is, the phase in third harmonic radiation changes by 720 deg. around the optical axis. In this way, it was shown that the harmonics radiation has the phase difference with $90(n-1)$ between $\phi = 0$ deg. and $\phi = 90$ deg. or $180(n-1)$ between $\phi = 0$ deg. and $\phi = 180$ deg.

Therefore, considering the discussion in the previous result where higher harmonics do not appear on the optical axis, the fundamental radiation has no helical wavefront, but only the higher harmonics have a helical wavefront even in the radiation from the magnetic mirror field.

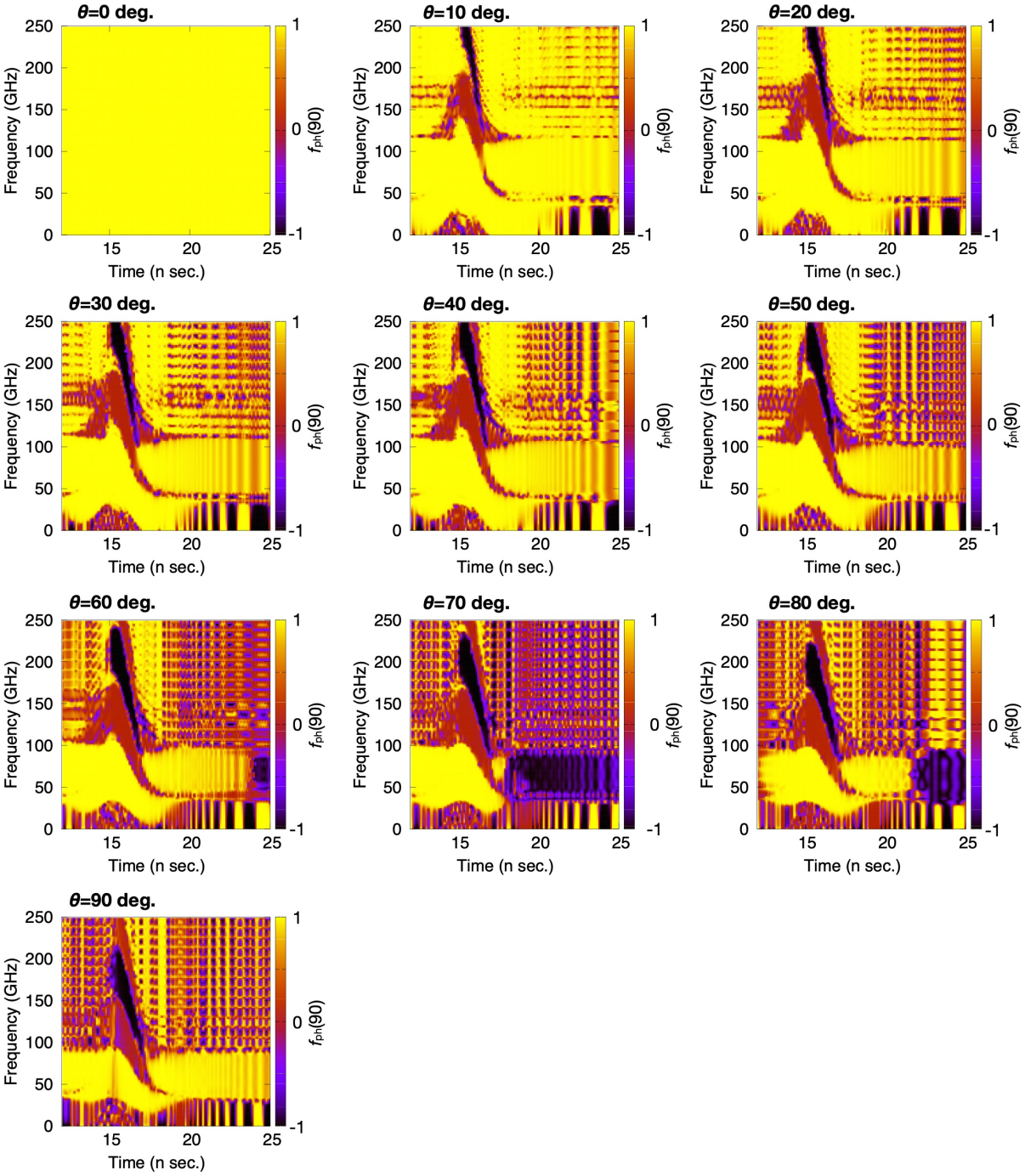

Figure 3.19: Time variation of the cosine value of the phase difference between $\phi = 0$ deg. and $\phi = 90$ deg. calculated by eq.(3.8) when the magnetic field is set to 2.286 T and the energy in z-direction has 18 keV.

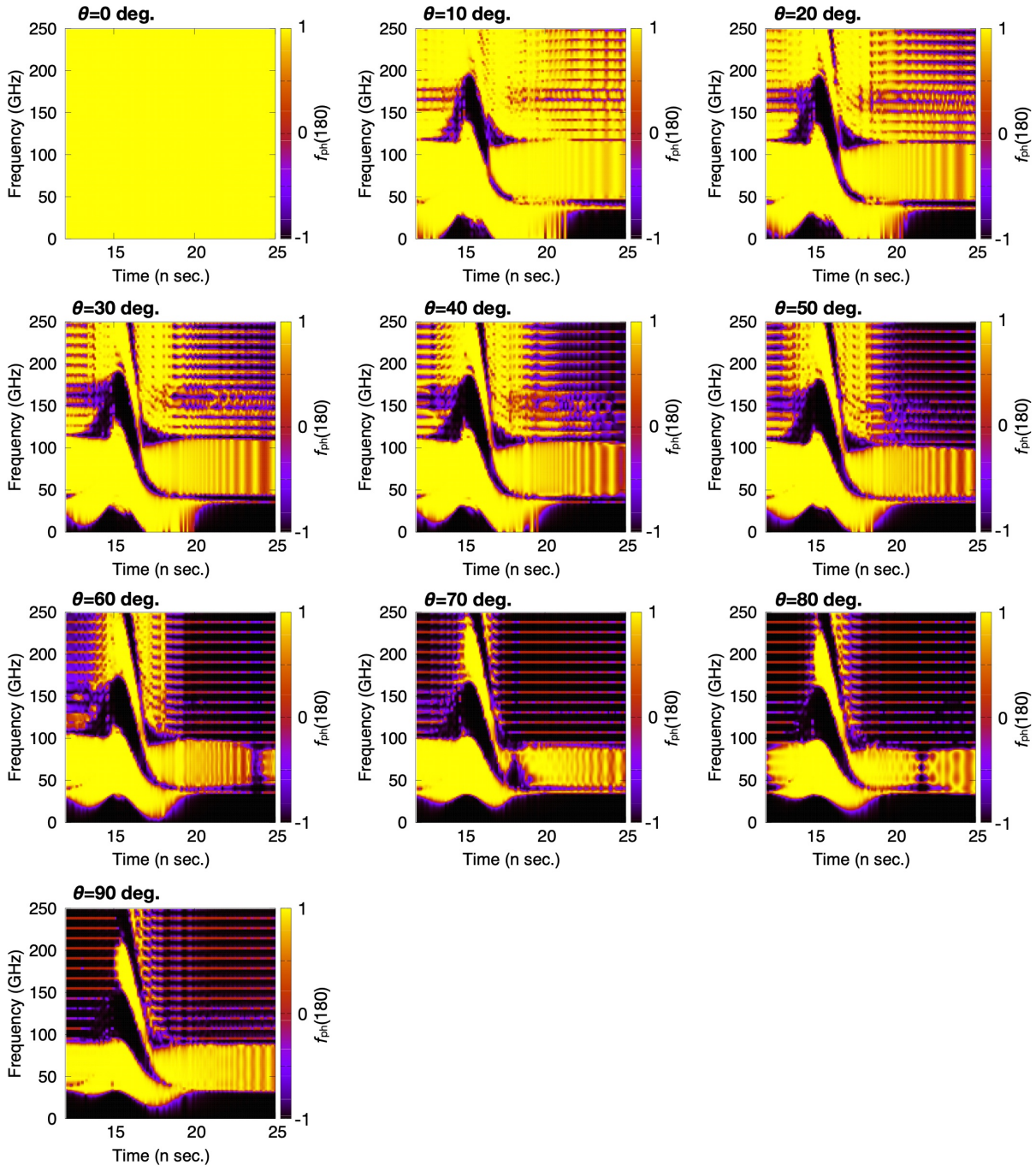

Figure 3.20: Time variation of the cosine value of the phase difference between $\phi = 0$ deg. and $\phi = 180$ deg. calculated by eq.(3.8) when the magnetic field is set to 2.286 T and the energy in z-direction has 18 keV.

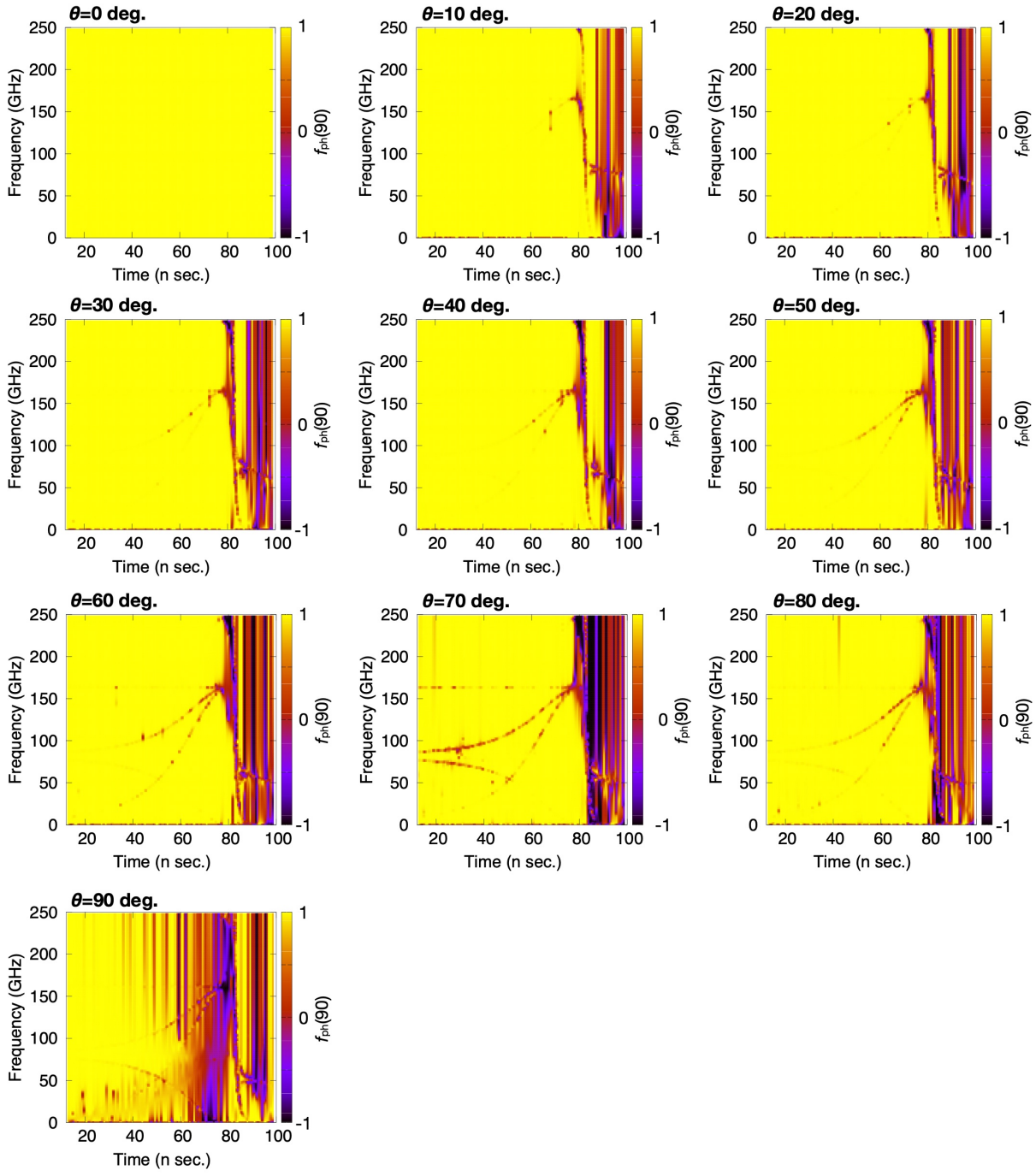

Figure 3.21: Time variation of the cosine value of the phase difference between $\phi = 0$ deg. and $\phi = 90$ deg. calculated by eq.(3.8) when the magnetic field is set to 2.909 T and the energy in z-direction has 0.1 keV.

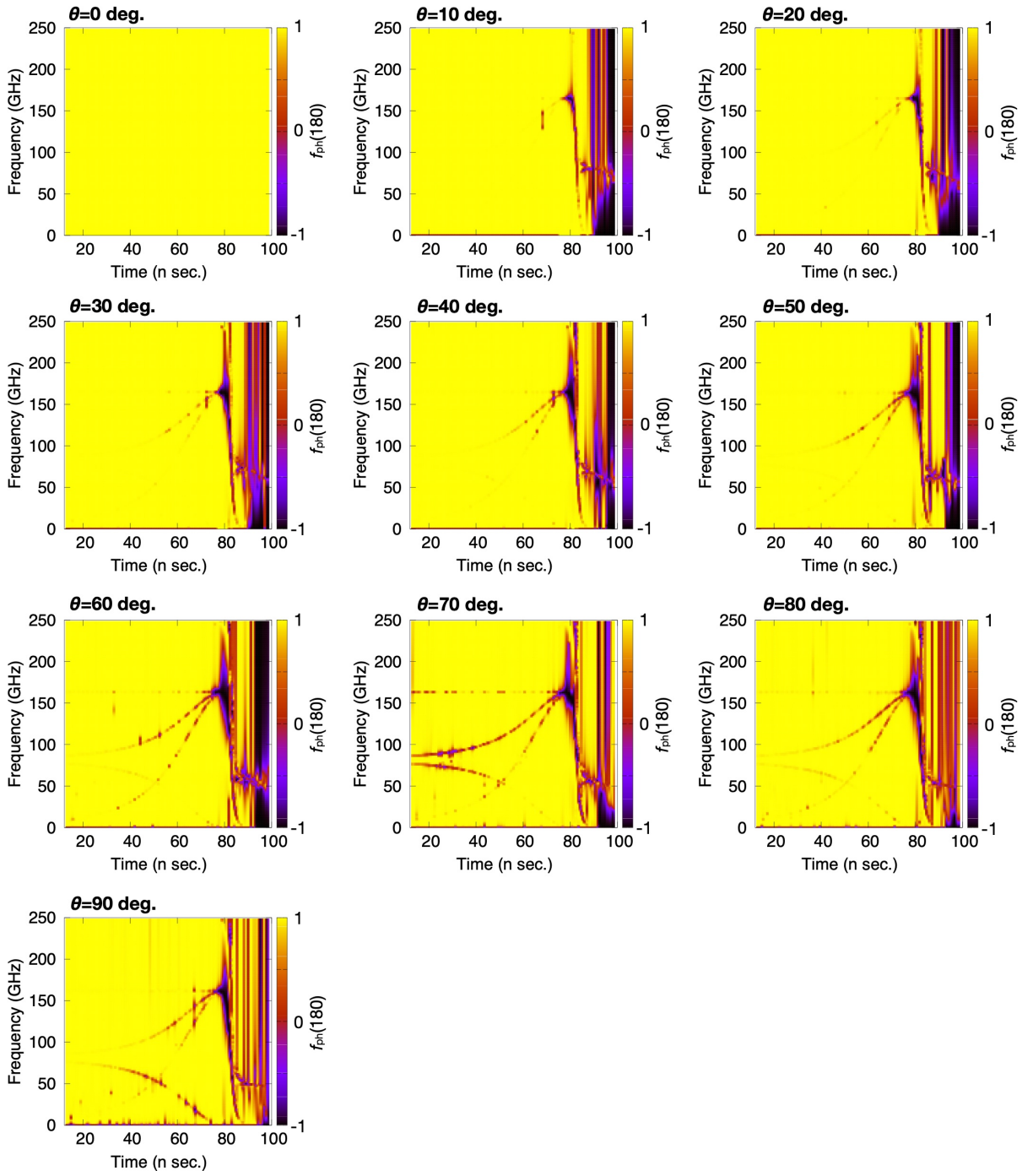

Figure 3.22: Time variation of the cosine value of the phase difference between $\phi = 0$ deg. and $\phi = 180$ deg. calculated by eq.(3.8) when the magnetic field is set to 2.909 T and the energy in z-direction has 0.1 keV.

3.4 Summary

In this chapter, we carried out the numerical calculation regarding ECE with a helical wavefront from an electron accelerated by a circularly polarized wave. In this calculation, a RHCP wave was applied to an electron with cyclotron motion. And a radiation from the rotation phase-controlled electron was performed. Our calculation showed the rotation phase of the electron could be controlled by high power RHCP wave by accelerating the electron with cyclotron motion resonantly and then demonstrate the coherent radiation with a helical wavefront. We calculated two types of external magnetic fields: a static uniform magnetic field, and the magnetic mirror field.

In the case of a static uniform magnetic field, when the RHCP wave was applied to the electron with cyclotron motion, the electron received energy from the incident RHCP wave and the relativistic mass gradually increased. Thus, the Larmor radius increased and the cyclotron frequency decreased. Meanwhile, the electron was accelerated in the z-direction by the Lorentz force $\boldsymbol{\beta}_{\perp} \times \boldsymbol{B}_{\mathrm{in}}$, and reached a relativistic velocity. In this case, the frequency of the RHCP wave seen from the reference frame of electron was observed to be downshifted due to the Doppler effect. The results confirmed a phenomenon called cyclotron auto-resonance, i.e., the relativistic electron cyclotron frequency and the downshifted frequency of RHCP wave seen from the reference frame of the electron are almost equal, and the electron maintains in the resonance state. In addition, it was confirmed that the phase relationship between the electric field vector of the externally applied wave and the acceleration vector of the electron were in the same phase relationship at a given z plane. Although this calculation was performed for a single electron, the same phenomenon occurs for each electron in a multi-electron system. Therefore, by applying RHCP wave to a multi-electron system with an initial random rotational phase, the rotational phase of each electron is controlled and coherent radiation with a helical wavefront can be obtained.

Radiation from the electron in a such a state was calculated using the Liénard-Wiechert potential and observed on the upper hemisphere. As a result, only the fundamental radiation appears in the frequency spectrum on the optical axis, and the spectrum of higher harmonics radiation did not appear. However, a spectrum of radiation including higher harmonics was observed at a position away from the optical axis. The absence of harmonics radiation on the optical axis indicated that the intensity distribution of higher harmonics radiation is donut-shaped. This indicates that active radiation from the charged particle with spiral motion produces helical wavefront - one of the characteristics of the vortex beam. In addition, we calculated the phase difference of the radiation at the symmetric point with respect to the beam axis. The higher harmonics have the phase difference with the relationship of $90(n-1)$ between $\phi = 0$ deg. and $\phi = 90$ deg. or $180(n-1)$ between $\phi = 0$ deg. and $\phi = 180$ deg. while the fundamental radiation has no phase difference. These results suggest that ECE has a helical wavefront from the characteristics of donut-shaped intensity distribution and azimuth-dependent phase structure.

The same calculation was performed for the magnetic mirror field. We confirmed that ECE has a helical wavefront even in the magnetic mirror field, which can be easily realized experimentally. ECE with a helical wavefront will be generated by interaction between the electrons with cyclotron motion in the magnetic mirror field accelerated by the externally applied RHCP wave.

In addition, we can understand that the system where an electron in cyclotron motion under the magnetic field is accelerated by the externally applied circular polarized wave is the same principle with Electron Cyclotron Resonance Heating (ECRH) in fusion plasma. This suggests that when the electrons are heated by circular polarized wave in fusion plasma, electrons are locally phase-controlled and produce the coherent ECE with helical wavefront. By focusing our attention on ECE measurement with helical wavefront in fusion plasma, the decay process of the helical wavefront becomes an index of the thermal relaxation regarding heated plasma electrons in real and velocity spaces.

In this calculation, there is no interaction between electrons because the radiation is calculated from an electron. However, in the experiment, since the radiation is considered from a multi-electron system, calculation considered in the multi-electron system is also important. However, the externally applied electromagnetic wave used in the experiment is high-power millimeter-wave from a gyrotron, and this electric field is considered to be sufficiently larger than the interaction force between electrons under the realistic electron density considered. Therefore, the effect of electron-electron interaction are considered to be ignored even in multi-electron calculations. Nevertheless, we are also attempting to calculate by Particle-in-Cell (PIC) simulation for more precise calculations.

Bibliography

[1] Y. Goto, S. Kubo, and T. I. Tsujimura, "Cyclotron Emission with a Helical Wavefront from an Electron Accelerated by the Circularly Polarized Wave," submitted for review to J. Adv. Simulat. Sci. Eng.

[2] J. D. Jackson, "Classical Electrodynamics" 3rd ed., Wiley, (1998).

[3] Y. Kuramitsu and V. Krasnoselskikh, "Acceleration of charged particles by gyroresonant surfing at quasi-parallel shocks," *Astron. Astrophys.*, **438** (2005), 391-402.

[4] C. S. Roberts and S. J. Buchsbaum, "Motion of a Charged Particle in a Constant Magnetic Field and a Transverse Electromagnetic Wave Propagating along the Field," *Phys. Rev.*, **135**:2A (1964), A381-A389.

Chapter 4

Experimental Devices

4.1 Arrangement

In order to demonstrate the ECE with helical wavefront, we designed and developed the experimental devices. These experimental devices are installed in the heating power equipment room at National Institute for Fusion Science (NIFS). More than seven gyrotrons are installed in this room mainly to heat the plasma electrons. Since the gyrotron is a device that accompanies electron acceleration by a high voltage, the area where the gyrotrons are installed is designated as a radiation control area. Fig.4.1 shows our experimental devices. These experimental devices are composed of 84 GHz gyrotron, MOU, transmission system including polarization box, and interaction vacuum chamber.

4.2 Concept of the Experiment

In order to demonstrate the ECE with helical wavefront, we designed the experimental device for producing ECE with helical wavefront shown in Fig.4.2 [1]. The ultimate purpose of this study is to experimentally demonstrate the thermalization of the resonantly accelerated electrons by measuring ECE with helical wavefront from the electrons with randomization of the rotation phase. Therefore, it is necessary to design and develop the experimental device so that the coherent radiation with helical wavefront can be produced. This experimental device makes it possible to control the rotation phase of electrons with cyclotron motion by externally applied circularly polarized wave. First, this idea of producing a coherent state of electrons by applying the circularly polarized wave to electrons in magnetic mirror field is unique. This is an original idea for obtaining the coherent radiation by producing and maintaining the coherent state of the electrons without canceling out the helical wavefront. In addition, we developed the grating mirror to overcome the issue of how the ECE including the fundamental radiation and the higher harmonics radiation with the same optical axis can be separated into second harmonic

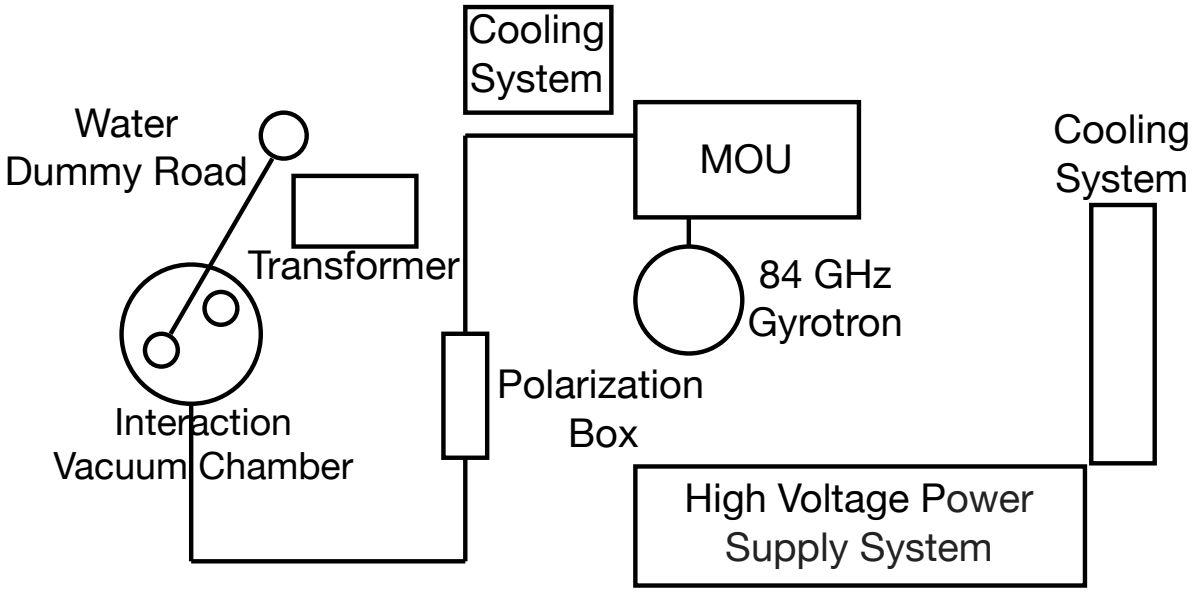

Figure 4.1: Arrangement of the radiation control area where our experimental equipment is installed.

radiation with helical wavefront. Furthermore, the grating mirror developed in this study is designed so that the second harmonic radiation can be reflected/diffracted efficiently, that is, any other diffracted beam disappear.

The mirror field is created by the stacked pancake coils. Electrons are supplied from the electron gun installed behind the reflecting mirror through a small hole along the magnetic mirror field. Electrons travel to the interaction area while maintaining cyclotron motion. Then, from the outside, high power Right-Handed Circularly Polarized (RHCP) wave at 84 GHz is injected in parallel to the magnetic field to the region to control the electrons' motion. The radiation from the group of electrons is coherent radiation because the rotation phase of each electron is controlled by injected beam. Since the helical wavefront has only second or higher harmonics, the radiation has to be separated into the fundamental radiation and the second harmonic radiation by the grating mirror. The separated second harmonic radiation is detected by the detection system.

4.3 Gyrotron

A gyrotron is a high power vacuum tube which generates a millimeter wave by maser action with electron cyclotron motion [2]. The output frequency from the gyrotron can be set between the millimeter wave regime to the sub-millimeter wave regime by changing the magnetic field strength applied in the optimized cavity. High power gyrotrons are used for an Electron Cyclotron Resonance Heating (ECRH) of plasma electron, an Electron

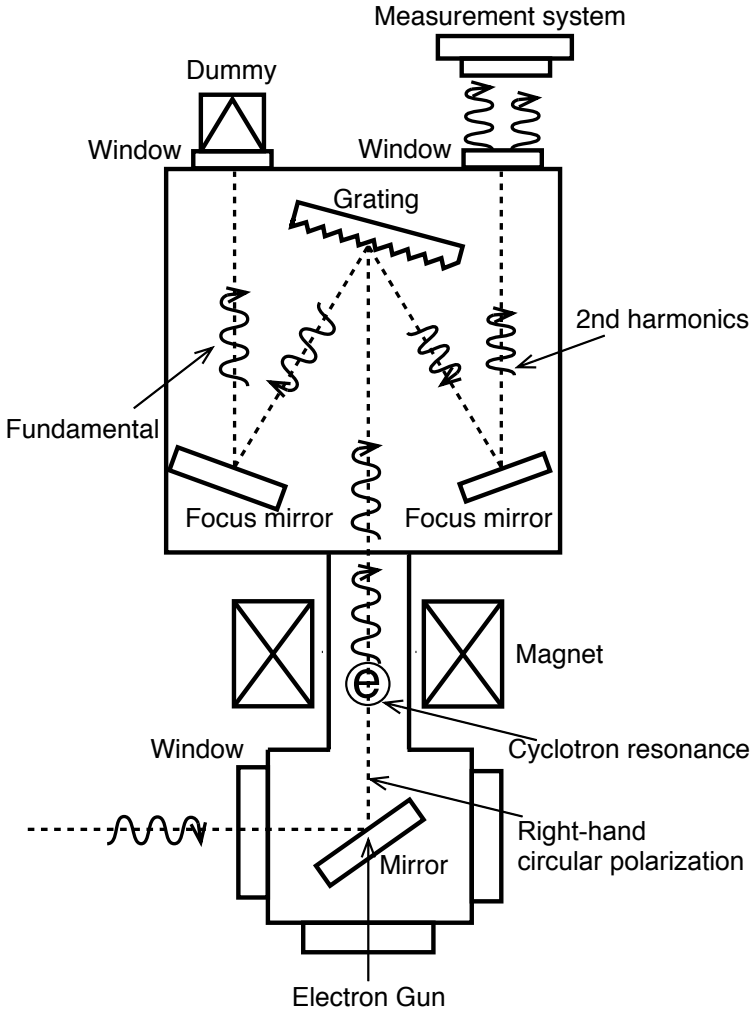

Figure 4.2: Schematic diagram of the experimental device which produces the ECE with helical wavefront.

Cyclotron Current Drive (ECCD) in fusion oriented plasma confinement machine. It is also used as a light source for scattering measurement in plasma in the frequency regime from millimeter wave to sub-terahertz wave. Fig.4.3(a) and (b) show a diagram for gyrotron and a photograph of 84 GHz gyrotron which is used in our experiment. Thermal electrons are extracted by high voltage from the cathode. And electrons travel to the cavity while maintaining cyclotron motion along the magnetic mirror field generated by the superconducting magnet. A part of the energy of the electrons in the perpendicular direction to the magnetic field is efficiently converted into electromagnetic wave by a resonant interaction in the cavity. The emitted electromagnetic wave is in the TE_{mn} mode, and it is converted to almost Gaussian beam with linear polarization by a mode

converter. The window at the output port is used by synthetic diamond made by Chemical Vapor Deposition (CVD), which has low dielectric loss and excellent heat conductivity for cooling and is durable for vacuum. Electrons are decelerated and collected by a reverse electric field applied between the collector and cavity.

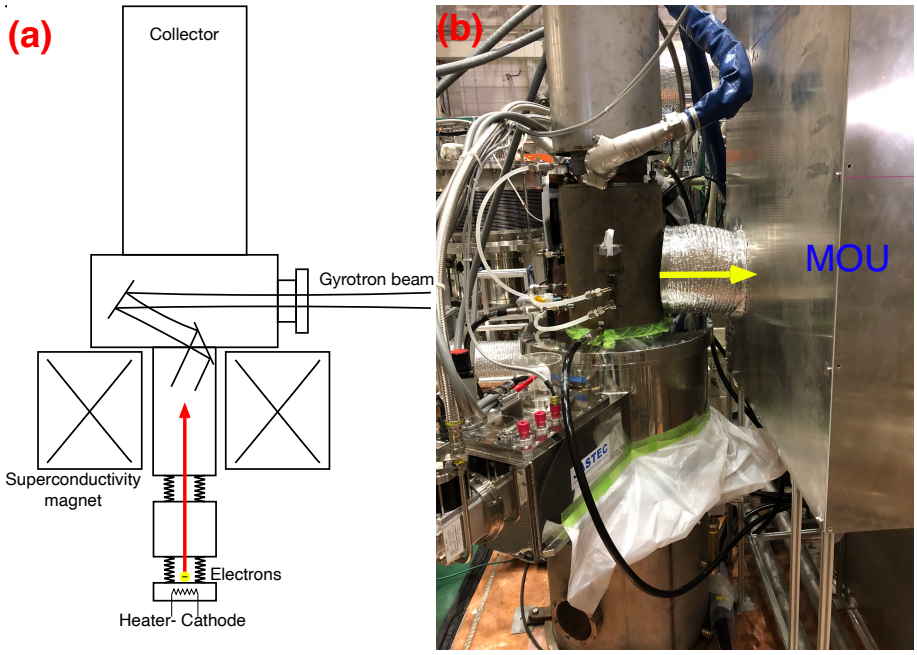

Figure 4.3: (a) and (b) are a diagram for gyrotron and a photograph of 84 GHz gyrotron which is used in the experiment.

4.4 Matching Optics Unit

Matching Optics Unit (MOU) is a transmission system to shape the beam to HE_{11} mode for coupling to the corrugated waveguide [3]. The beam emitted by gyrotron has a flater beam distribution than Gaussian beam distribution because the heat load at the gyrotron window is suppressed. Fig.4.4 and Fig.4.5 show the photograph of the MOU and the diagrams. The MOU is composed of six mirrors. These mirrors are named as MM1 to MM6 in order, respectively. The shaped beam is coupled to the corrugated waveguide. This mirror can slide toward the arrow direction, and the gyrotron beam can be conditioned by being injected into dummy bricks in the MOU when the gyrotron is activated.

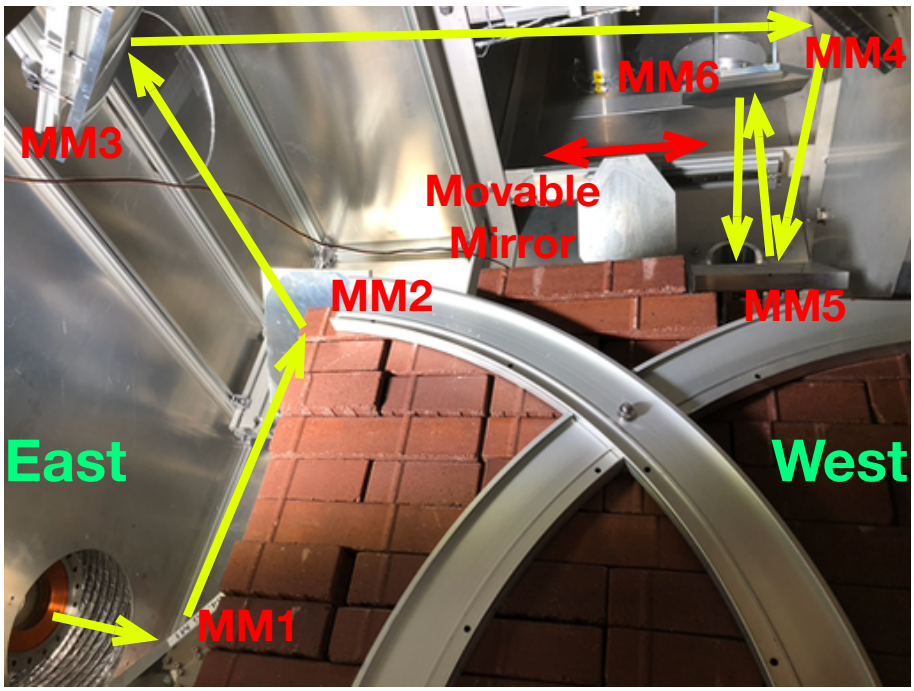

Figure 4.4: Photograph of the mirrors system inside the MOU. The MOU is composed of six mirrors, and the shaped beam is coupled to the corrugated waveguide.

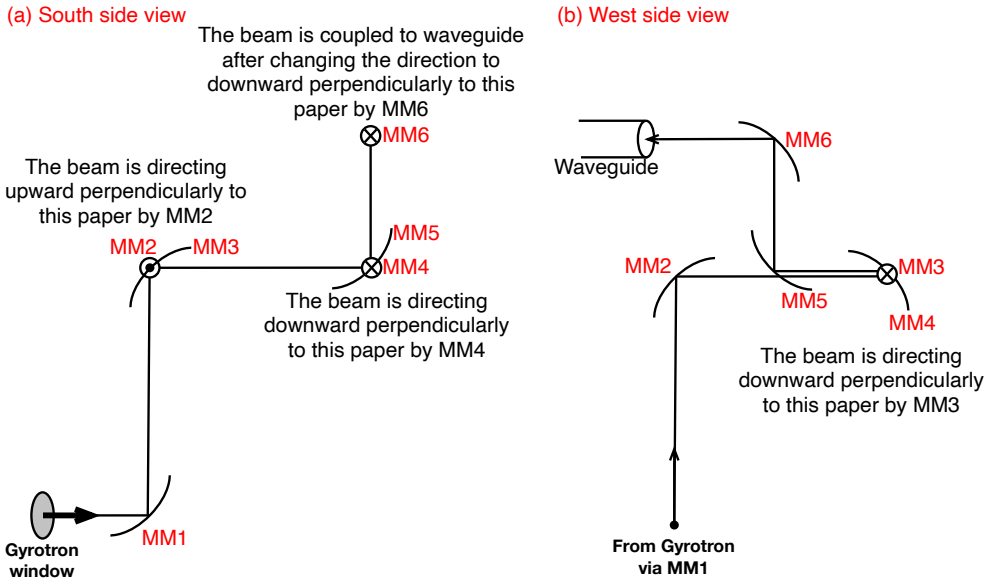

Figure 4.5: Diagram of the mirrors system inside the MOU. (a) shows the south side view and (b) shows the east side view.

4.5 Transmission System

Fig.4.6 and Fig.4.7 show the diagram and photograph of the transmission system. This transmission system is composed of 13 mirrors including the mirrors in the polarizer box and the vacuum chamber. This transmission system is designed so that the waist size of the beam becomes 30 mm at the center of the superconducting coil where the magnetic field strength is strongest on the optical axis. These mirrors are named as M1 to M13 in order, respectively. The beam coupled with the waveguide partially propagates the corrugated waveguide including miter vent with low loss. After that, waveguide propagation shifts to propagation in air. The beam emitted from the horizontal waveguide is changed in the vertical downward direction by the mirror M1, and is injected to the polarizer through the mirror M2. The beam that has passed through the polarizer and turned into a circularly polarized wave is injected to the vacuum chamber via two mirrors, M8 and M9. The beam after injection into the vacuum chamber is described in Sec.4.7.

4.6 Polarizer

The polarizer is one of the key components in the transmission system which converts the linear polarized beam from gyrotron output to the beam with any polarization including two special mirrors with grooved surface [4]. The polarizer is necessary to produce the circularly polarized wave in this study because the rotation phase of the electrons emitted by electron gun has to be controlled by the circularly polarized wave from the outside for obtaining the coherent radiation. In this experiment, polarization box with two grooved surface mirrors have been used as shown in Fig.4.8, which used to be utilized in LHD experiments. When the groove width is $\frac{\lambda}{2}$ or less, the electric field of the parallel component with same direction of the groove cannot penetrate inside the groove. Here, λ is the wavelength of the beam. On the other hand, the electric field of the vertical component can penetrate inside the groove. Then, the reflected electric field components of parallel and perpendicular to the groove can have the phase difference. For the sake of simplicity, let us consider a case in which a beam is injected perpendicularly on a grooved mirror. The phase difference τ produced by the grooved mirror is given as follows

$$\tau = 2 \times \frac{2\pi d_p}{\lambda} \tag{4.1}$$

where d_p is the depth of the groove. When the d_p is $\frac{\lambda}{4}$, either of the phase is reversed, that is, the polarization angle can be changed. When the d_p is $\frac{\lambda}{8}$, either of the phase is shifted by $\frac{\lambda}{4}$, that is, the ellipticity of the polarization can be changed. Thus, by rotating the two grooved mirrors with $\frac{\lambda}{4}$ and $\frac{\lambda}{8}$, it is possible to obtain an arbitrary polarization state.

4.7 Interaction Vacuum Chamber

As shown in Fig.4.2, Interaction Vacuum Chamber is composed of mirrors system, electron gun, superconducting magnet, and measurement systems.

- Mirrors system:
  Four mirrors including grating mirror (M11) are installed in the interaction vacuum chamber as shown in Fig.4.10 (b) and (c), and they play an important role [1]. As shown in Fig.4.10 (b), the M10 mirror has a small hole with a diameter of 5 mm in the center, which allows electrons supplied from the electron gun to travel to the interaction region along the optical axis. Also, this mirror is insulated from the outside so that it is possible to measure the amount of current that does not go through the hole of the mirror. M11 is the grating mirror, and will be discussed in detail below. To put it simply, since the ECE includes higher harmonics radiation, the grating mirror makes it possible to separate the second harmonic radiation from fandamental radiation and third or higher harmonics radiaiton. M12 and M13 mirrors have a function for focusing the beam so that the fundamental radiation and separated second harmonic radiation by the grating mirror can pass through the window at the top of the vacuum chamber.

- Electron gun:
  The electron gun is installed at the bottom of the Vacuum chamber as shown in Fig.4.10 (d). We use the electron gun with model NJK2301 produced by New Japan Radio Co., Ltd. It is optimized for operation with a cathode voltage of -18 kV. There is also a grid in front of the cathode, which allows pulse operation. The cathode has a diameter of 10 mm, and the extracted electrons travel to the interaction region while doing cyclotron motion along the magnetic mirror field. Although the small hole size of the M10 mirror is a diameter of 5 mm, the Larmor radius gradually decreases due to the mirror field effect, thus most of the electrons can pass through the mirror's hole. In order to maintain high vacuum near the electron gun, differential pumping is adopted. The differential pumping system uses a small orifice to connect two parts of vacuum chamber.

- Superconducting magnet:
  We use the superconducting magnet with model JMTD-6.5T140G produced by Japan Superconductor Technology, Inc. shown in Fig.4.10 (a). It is possible to apply a magnetic field strength of 6.5 T at the center of the torus. And, the center position of the magnet is the same as the position where the waist size of the gyrotron beam is focused. The magnetic field strength is set to 2.95 T so that the electron perform cyclotron motion with 84 GHz which is the same as the frequency of the gyrotron. Fig.4.9 shows the measurement results of the distribution for magnetic field strength on the optical axis.

- Diamagnetism measurement:
  As shown in the Fig.4.10 (g), 150 turned enamel wire is wound with a width of 1 cm around the vacuum vessel inside the torus coil. This is called the diamagnetism measurement [5]. When the magnetic flux in the coil changes, an induced electromotive force is generated according to Faraday's law of induction. Although electrons are supplied by an electron gun for the source of radiation, as another option, it is also possible to supply electrons by producing plasma by the high power gyrotron beam. This measurement system can measure the plasma stored energy.

- Measurement ports:
  Fig.4.10 (e) and (f) are a photograph taken from the top of the vacuum chamber. There are four ICF203 flanges on the top. Two of them are CVD diamond windows described in Sec.4.3. Then, the fundamental radiation and second harmonic radiation are passed through. The remaining two ports are used for the vacuum pluming port.

- Measurement systems:
  We have developed measurement systems for millimeter wave with helical wavefront by using a triangular aperture and heterodyne detection at two spatial point [6]. The developed measurement system is installed at the top of the flange for measuring second harmonic radiation shown in Fig.4.10 (f). The distance from the radiation point where it is located on the center of the magnet to the grating is about 700 mm, and one side of the mirror is 130 mm. Therefore, the radiation within only the polar angle of 5 deg. can be reflected at the grating mirror, and be detected by the measurement system. In addition, considering the space distribution of the electrons, the coherence of the radiation disappears when the observer is located on the larger polar angle due to the incoherence of the space distribution of the electrons. However, the radiation near the optical axis can be measured in this experimental device, and the coherence of the radiation is maintained.

  The radiation which is not reflected on the grating mirror will become the multi-reflected background radiation inside the vacuum chamber. However, the multi-reflected background radiation does not matter in the measurement. Because the grating mirror developed in this study is designed so that the second harmonic radiation can be reflected/diffracted efficiently, and it is assumed that the radiation which is not reflected/diffracted on the grating mirror does not have larger intensity than the radiation which is reflected/diffracted on the grating mirror. Therefore, the multi-reflected background radiation can be treated as noise level. In addition, the higher harmonics radiation cannot be propagated in the waveguide due to the cutoff. Thus, these radiations do not matter. In the fusion experimental device, the ECE is observed with multi-reflected background radiation [7]. However, the ECE measurement has been carried out without any problems for the above reasons. The

details of these systems are given in Chapter 6.

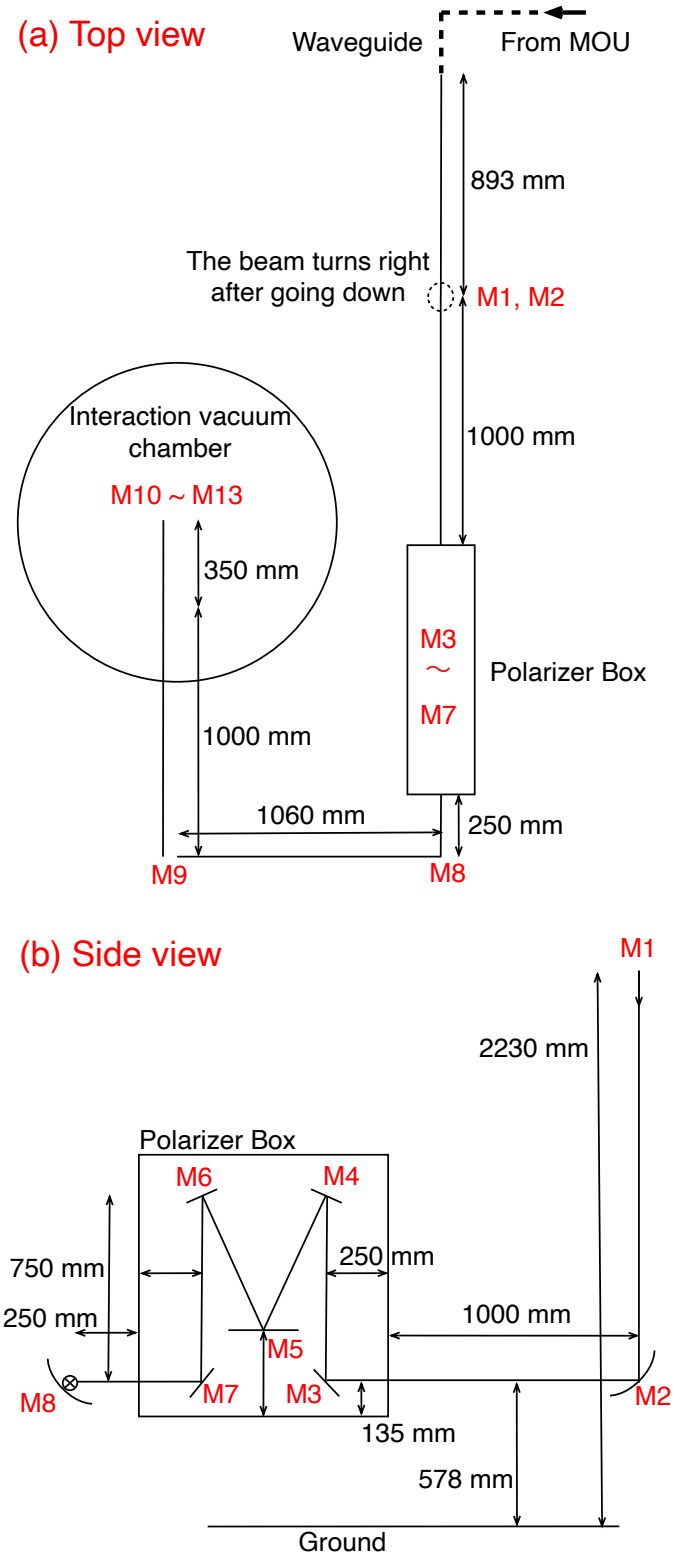

Figure 4.6: Diagram of the transmission system. (a) shows the top view and (b) shows the side view.

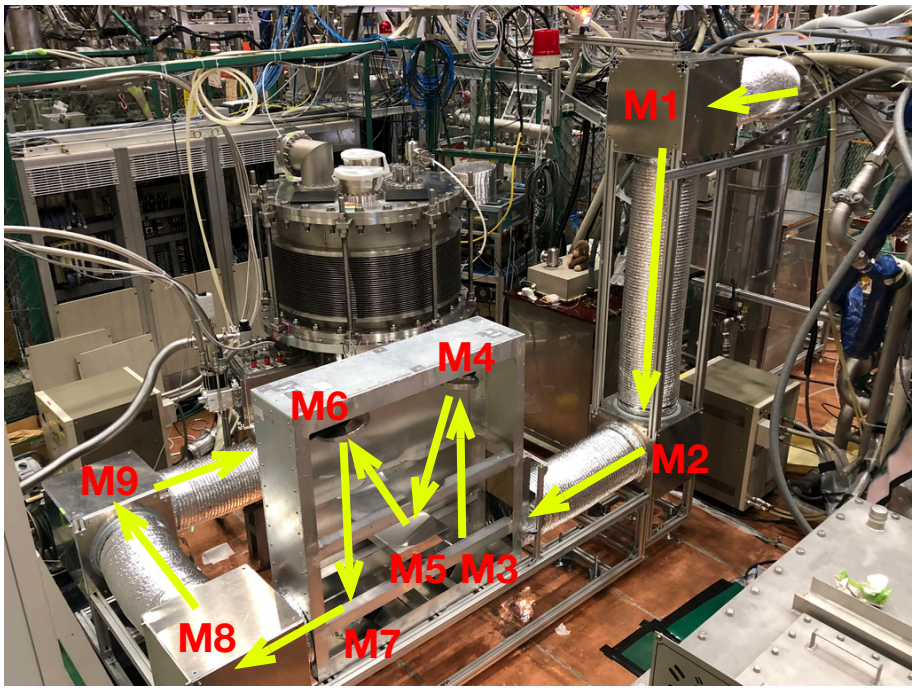

Figure 4.7: Photograph of the transmission system. This transmission system is composed of 13 mirrors including the mirrors in the polarizer box and the vacuum chamber. This transmission system is designed so that the waist size of the beam becomes 30 mm at the center of the superconducting coil where the magnetic field strength is strongest on the optical axis.

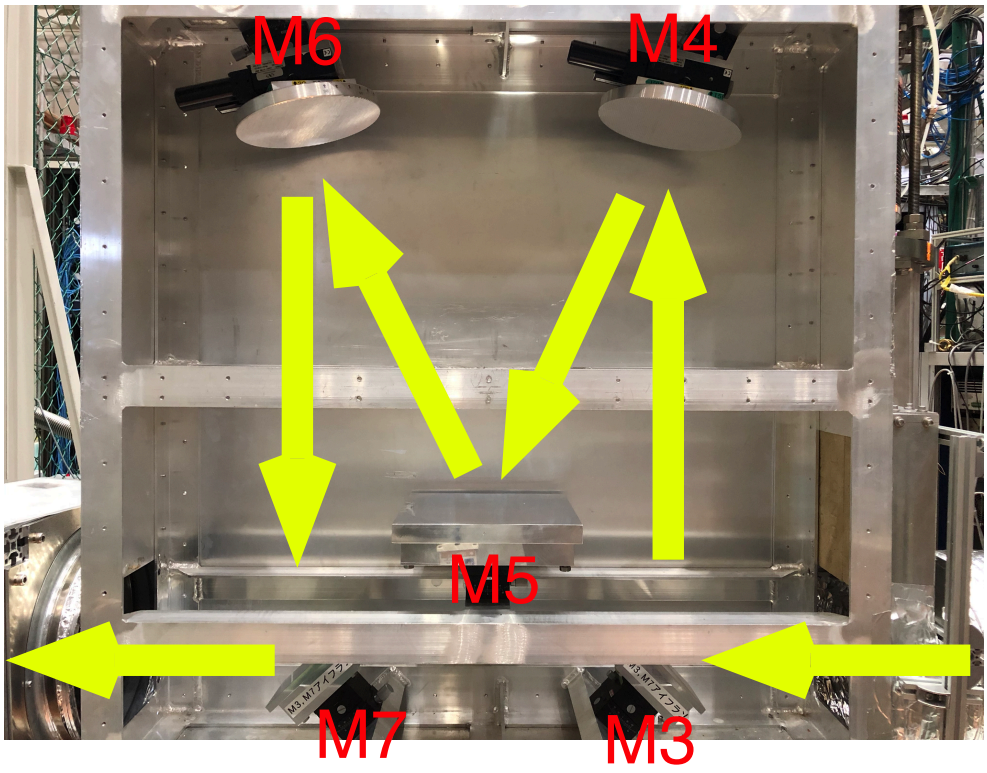

Figure 4.8: Photograph of the polarizer box. This polarizer box is composed of five mirrors including two grooved surface mirrors with $\frac{\lambda}{4}$ and $\frac{\lambda}{8}$.

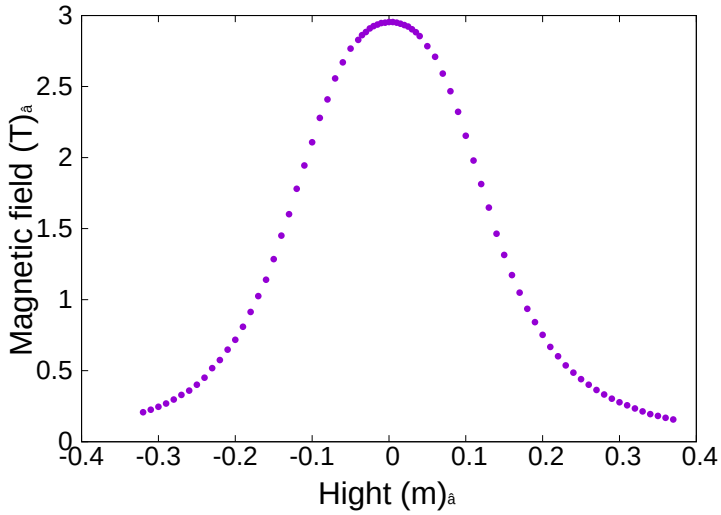

Figure 4.9: Distribution of the magnetic field strength along the optical axis. It is possible to apply a magnetic field strength of 6.5 T at the center of the torus.

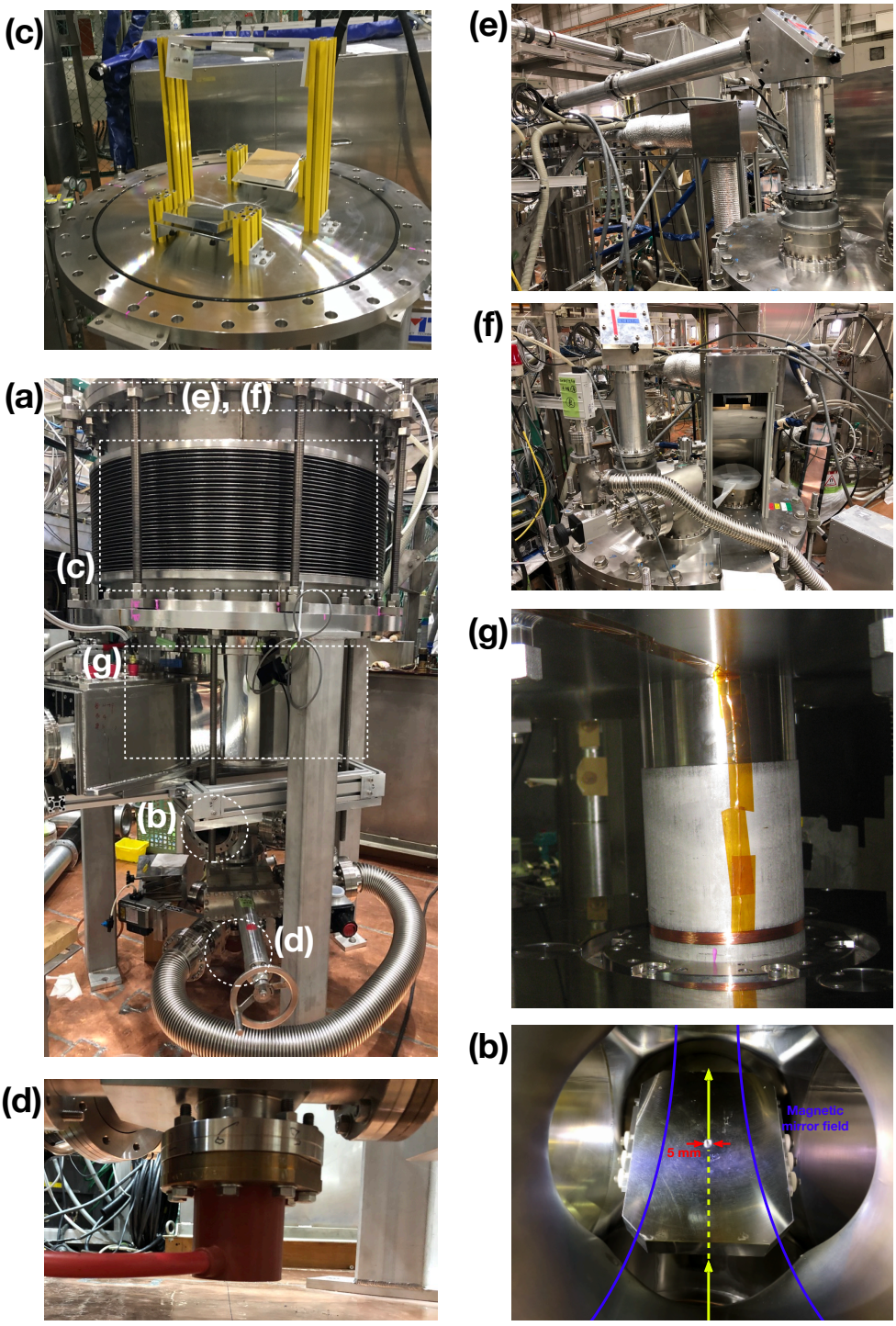

Figure 4.10: (a): Overall photograph of the vacuum chamber. (b): Photograph taken from the top of the vacuum chamber. There are four ICF203 flanges on the top. (c): Photograph of the electron gun installed at the bottom of the vacuum chamber. Photograph of the M10 mirror. The mirror has a small hole with a diameter of 5 mm in the center, which allows electrons supplied from the electron gun to travel to the interaction region along the optical axis. Photograph of the 150 turned enamel wire used in diamagnetism measurement. This is wound with a width of 1 cm around the vacuum vessel inside the torus coil.

Bibliography

[1] Y. Goto, S. Kubo, and T. I. Tsujimura, "Development of the Grating Mirror for the High Power Transmission System and Its General Theory," Plasma Fusion Res., **13**, 3405089 (2018).

[2] T. Shimozuma, "Fusion Plasma Application of Electromagnetic Waves with Hundred Giga Hertz Range of Frequency : Technologies of Electron Cyclotron Resonance Heating Devices," J. Plasma Fusion Res. **82**, 8, 506-516 (2006).

[3] K. Ohkubo, S. Kubo, H. Idei, M. Sato, T. Shimozuma, and Y. Takita, "Coupling of tilting Gaussian beam with hybrid mode in the corrugated waveguide," Int. J. Infrared Millimter Waves **13**, 1, 23 (1997).

[4] T. I. Tsujimura, S. Kubo, T. Shimozuma, S. Kobayashi, K. Okada, Y. Yoshimura, H. Igami, H. Takahashi, S. Ito, Y. Mizuno, K. Okada, R. Makino, K. Kobayashi, Y. Goto, and T. Mutoh "Design of polarizers for a mega-watt long-pulse millimeter-wave transmission line on the large helical device," Rev. Sci. Instrum, **86**, 2 (2015).

[5] V. D. Pustovitov, "Magnetic diagnostics: General principles and the problem of reconstruction of plasma current and pressure profiles in toroidal systems," Nucl. Fusion, **41**, 6 (2001).

[6] Y. Goto, T. I. Tsujimura, and S. Kubo "Diffraction Patterns of the Millimeter Wave with a Helical Wavefront by a Triangular Aperture," J. Infrared Millim. Terahertz Waves, **40**, 9, 943-951 (2019).

[7] Y. Goto, S. Kubo, H. Igami, M. Nishiura, T. Shimozuma, Y. Yoshimura, H. Takahashi, T. I. Tsujimura "Development of the calibration method for a fast steering antenna for investigating the mode conversion window used in EBW heating in the LHD plasma," Jpn. J. Appl. Phys, **58**, 106001 (2019).

Chapter 5

Development of the Grating Mirror

In this chapter, we discuss the development of the grating mirror, which efficiently separates the second harmonic radiation from the ECE including fundamental radiation. As discussed, it is theoretically demonstrated that the higher harmonics radiation from a charged particle in spiral motion has a helical wavefront. As one of the applications of the diffraction grating, the optimized grating mirror designed for the generation experiment of the ECE with helical wavefront plays an important role.

5.1 Grating Condition

In the analysis of radiation with many frequency spectral peaks, the grating mirror plays an important role in separating these frequencies toward the specific angles. Although the diffraction beam is usually a weak signal, we can optimize the grating parameters to maximize the diffraction efficiency by designing the grating with an adequate blaze angle. In this case, the two frequencies ω_1=82.7 GHz and ω_2=165.4 GHz are considered. The grating mirror is designed as shown in Fig.5.1(i). That is, ω_1 is reflected toward +30 deg. and ω_2 is reflected and diffracted toward -30 deg. The grating mirror is designed by the order shown from Fig.5.1(ii) to Fig.5.1(iv). (ii): Note that the ω_1 is only satisfied with the law of reflection (only 0th order diffraction). That is, the injection angle is 15 deg. with respect to the base mirror surface. (iii): To reflect toward -30 deg. with respect to the ω_2, the slope shaped saw-tooth is added on the base mirror surface. The angle of the slope is reflected toward -30 deg. with respect to this slope surface for ω_2. That is, the angle of the slope is 30 deg. This is the blaze angle. (iv): Considering the case in which many slopes are placed regularly, this corresponds to the grating with line spacing d. The direction of the diffracted beam is determined by d. Here, let us decide that the line spacing can be only propagated to -30 deg. for the diffracted beam of the ω_2. A well

known diffraction condition is

$$\sin\theta_{\rm in} + \sin\theta_{m,\rm out} = \frac{mk_g}{nk_0}, \tag{5.1}$$

where m is the diffraction order, n is the harmonics number, $\theta_{\rm in}$ is the injection angle, $\theta_{m,\rm out}$ is the diffraction angle of the mth order, k_g is the wave-number of the grating which is defined by $k_g = 2\pi/d$, and k_0 is the wave-number of the nth harmonics beam. Fig.5.2 shows the relationship between the line spacing and the direction of the diffracted beam. As can be seen from this figure, the line spacing d should be set at 1.878 mm in order to propagate in only the 2nd diffracted beam to -30 deg. direction. Therefore, although the $n = 0$ component, which is only a reflection component on the mirror surface, cannot be ignored, the main diffracted beam can be propagated -30 deg. Fundamental radiation ω_1 can be only reflected to +30 deg. (0th order) without generating the extra diffracted beam by choosing the proper line spacing. Note that the wave length λ_1 of the ω_1 (λ_1= 3.628 mm) is much greater than the height of the slope whth 0.813 mm and the wave ω_1 is recognized the surface of grating mirror we developed as a plane. That is, ω_1 is neither refracted nor diffracted on the added slopes. Therefore, ω_1 is reflected toward +30 deg. and ω_2 is almost reflected and diffracted toward -30 deg. by the many slopes on the mirror. This corresponds to the Littrow mount condition.

5.2 Low Power Test

In order to confirm the efficiency of the grating mirror we developed, low power experiments are carried out. Fig.5.3 shows the experimental set up. The 84 GHz and the 165.4 GHz beam sources are used. These beams are propagated to the grating mirror individually and the reflected or/and the diffracted beam are detected by the horn antenna. Fig.5.4 shows the experimental results. In the 84 GHz, it is found that the beam was propagated to the direction designed precisely. In the 165.4 GHz, the reflected beam and the diffracted beam were distributed mainly in the direction of -30 deg. Some diffracted beams are propagated in the direction of 30 deg. However, it was clearly demonstrated that the radiation at the ω_1 and the ω_2 can be separated by this grating mirror as designed.

5.3 General Theory of the Grating Mirror Development

The grating mirror which was developed here is plane-shaped because machining or development was easier. However, this design method can be generalized to the grating mirror which has an arbitrary base mirror shape such as a concave mirror.

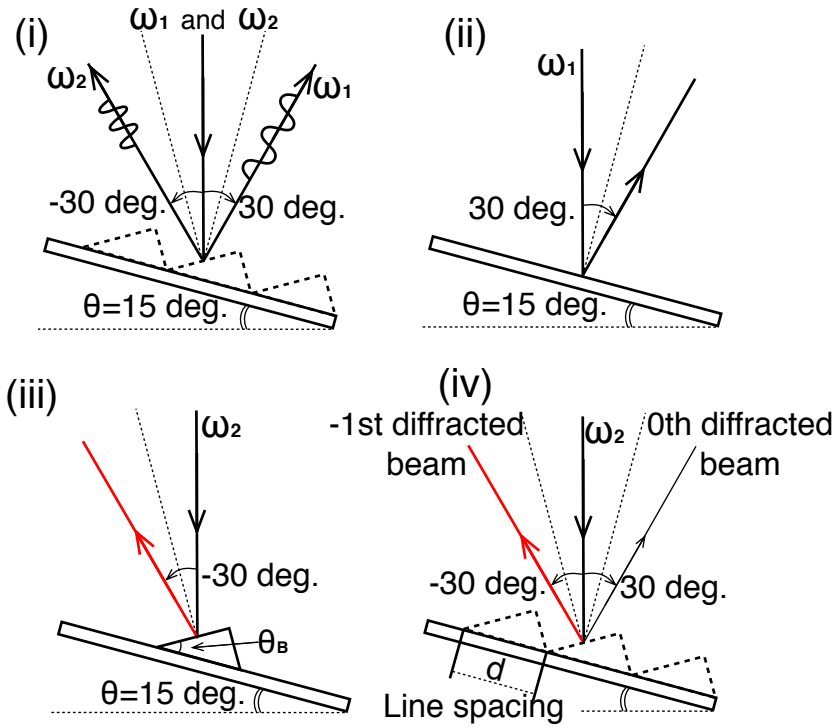

Figure 5.1: (i)Required grating mirror performance. Fundamental high power beam is to be reflected only toward +30 deg. Main power of the 2nd harmonics is to be diffracted toward -30 deg. (ii)The radiation of the frequency ω_1 is only reflected or 0th order diffracted toward +30 deg. direction without higher order diffraction by setting $d < \lambda/2$ or $k_g > 2k_0$ on the grating mirror. (iii)The main power of the radiation of the frequency ω_2 is diffracted toward -30 deg. by the slope with the blaze angle θ_B on the mirror. (iv) Many slopes are placed on the mirror in order to make the grating. Determining the line spacing so that the -1st beam can be directed toward -30 deg [1].

5.3.1 Definition of the Mirror Surface

The local wave-number $\boldsymbol{k}$ of the Gaussian beam which has finite spatial spread is defined by a gradient of the equiphase front Φ [2] as follows,

$$\boldsymbol{k} = \nabla\Phi. \tag{5.2}$$

Once the input and the output of the Gaussian beam parameters are defined, local wave numbers $\boldsymbol{k}_{\rm in} = \nabla\Phi_{\rm in}$ and $\boldsymbol{k}_{\rm out} = \nabla\Phi_{\rm out}$ on a mirror surface should satisfy the equation below,

$$\boldsymbol{k}_{\rm in} - \boldsymbol{k}_{\rm out} = \nabla S_{\rm mirror} \parallel \boldsymbol{N}. \tag{5.3}$$

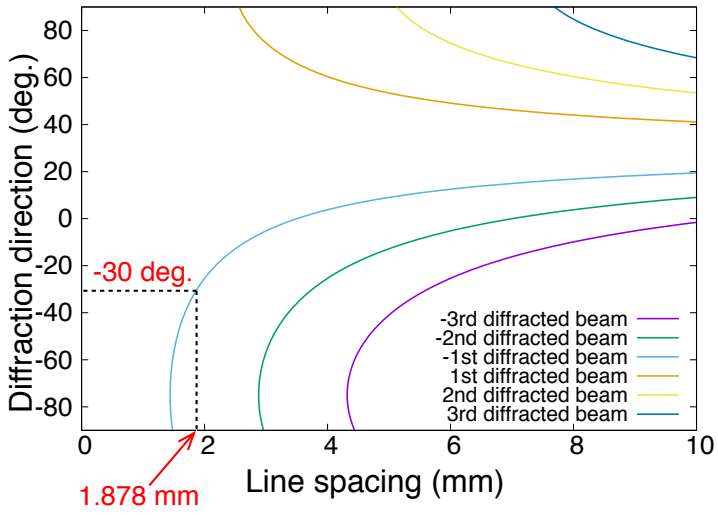

Figure 5.2: Relationship between the line spacing and the direction of the diffracted beam [1].

The S_{mirror} is the mirror surface function defined by $S_{\text{mirror}} = \Phi_{\text{in}} - \Phi_{\text{out}}$. The $\boldsymbol{N}$ is the normal vector of the mirror surface. By integrating eq.(5.3), the mirror surface function is determined as follows,

$$S_{\text{mirror}} = \Phi_{\text{in}} - \Phi_{\text{out}} = \text{const.} \tag{5.4}$$

In other words, the mirror surface is defined as the constant surface of the difference between Φ_{in} and Φ_{out}. This is a phase matching condition or a constant phase distance condition of between input and output beam on the mirror, and can be interpreted as a generalization of the elliptical mirror that satisfies a constant distance between focal points for a geometrical optics [3]. It should be noted that the input beam and the output beam are Gaussian beams. The beam parameter, waist size, and waist position should be matched not only to the phase but also to the intensity on the mirror surface in 0th order. This gives the condition of input and output Gaussian beam parameters.

5.3.2 Relationship between Grating Condition and Mirror Surface

The grating condition for the vector representation is

$$\boldsymbol{k}_{\text{out},m} \cdot \nabla G = \boldsymbol{k}_{\text{out}} \cdot \nabla G + m\boldsymbol{k}_G \cdot \nabla G, \tag{5.5}$$

where $\boldsymbol{k}_{\text{out},m}$ is wave-number vector of the mth order diffracted beam and $\boldsymbol{k}_G$ is the wave-number of the grating. G is the grating function which is defined by $\boldsymbol{k}_G = \nabla G$. Here, the

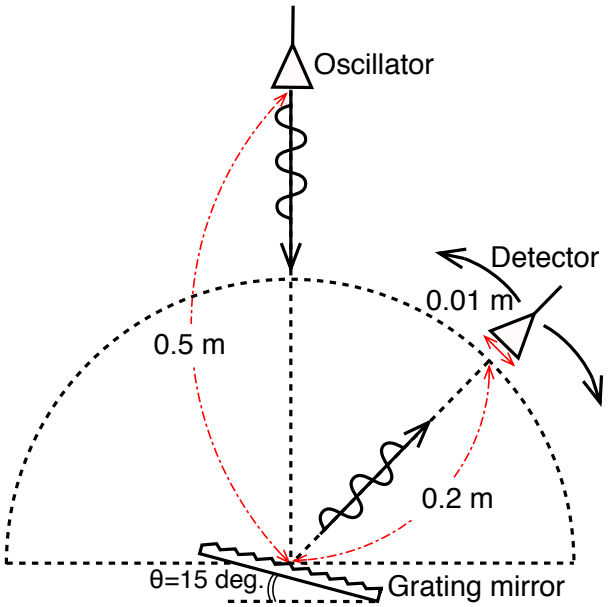

Figure 5.3: Low power experimental set up: The beams which are emitted by the oscillator are reflected or diffracted by the grating mirror. These beam radiation patterns are measured by the angle scanning receiving antenna by 1 deg. Because the experimental setup is arranged so that both long sides of the antenna area and moving distance of the antenna per deg. are almost the same, the angular resolution is best [1].

direction of the $\boldsymbol{k}_G$ is periodic direction of the grating. The orthogonal condition between the grating surface and the mirror surface is

$$\nabla S_{\text{mirror}} \cdot \nabla G = 0. \tag{5.6}$$

Although the relationship which determines the mirror surface function is given by eq.(5.3), the grating mirror is considered as a form in which the grating function is incorporated into this mirror surface function. These relationships are represented as follows,

$$\nabla \Phi_{\text{in},\omega_1} - \nabla \Phi_{\text{out},\omega_1} = \nabla S_{\omega_1} \tag{5.7}$$

$$\nabla \Phi_{\text{in},\omega_2} - \nabla \Phi_{\text{out},\omega_2} = \nabla S_{\omega_2} \tag{5.8}$$

$$\nabla \Phi_{\text{out},\omega_2} \cdot \nabla G + m \nabla G \cdot \nabla G = \nabla \Phi_{\text{out},\omega_2,m} \cdot \nabla G, \tag{5.9}$$

where $\Phi_{\text{in},\omega_1}$, $\Phi_{\text{out},\omega_1}$, and S_{ω_1} are equiphase front of the injection beam, the reflection beam, and the mirror surface function of the these beams, respectively. $\Phi_{\text{in},\omega_2}$, $\Phi_{\text{out},\omega_2}$,

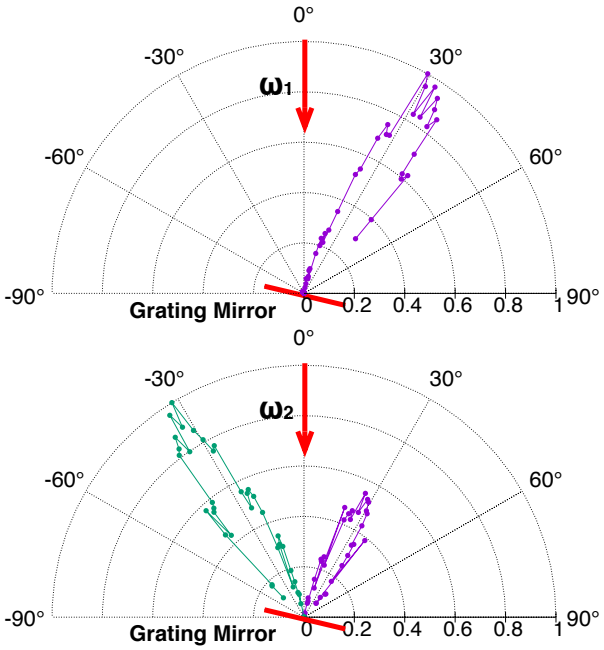

Figure 5.4: Angular distribution of the ω_1 and the ω_2: Intensity is represented by the radial direction and it is normalized by the maximum. Propagation directions of the reflection or diffraction beams are represented by the angle direction [1].

and S_{ω_2} are equiphase front of the injection beam, the refraction beam, and the mirror surface function of these beams, respectively. Eq.(5.9) is replaced by substituting eq.(5.2) for eq.(5.5). $\Phi_{\mathrm{out},\omega_2,m}$ is equiphase front of the mth order diffraction beam. Multiplying eq.(5.8) by ∇G and using the orthogonal condition eq.(5.6), we can obtain the following equation

$$\nabla\Phi_{\mathrm{in},\omega_2} \cdot \nabla G + m\nabla G \cdot \nabla G = \nabla\Phi_{\mathrm{out},\omega_2,m} \cdot \nabla G. \tag{5.10}$$

That is,

$$\nabla(\Phi_{\mathrm{in},\omega_2} - \Phi_{\mathrm{out},\omega_2,m} + mG) \cdot \boldsymbol{N}_G = 0 \tag{5.11}$$

where $\boldsymbol{N}_G$ is the normal vector on the grating function, which is defined by $\boldsymbol{N}_G = \nabla G/|\nabla G|$. If the equiphase of the ω_2 and the equiphase of the mth order diffracted beam are known, the grating function G is determined. Therefore, the grating function G is defined on the mirror surface function S_{ω_1}. Here, the grating function can be shown in Fig.5.5. Fig.5.5 (a) shows the mirror surface defined and calculated by eq.(5.4), and the grating can be defined on this surface so that the diffraction beam can be propagated toward the direction as shown in Fig.5.5 (b). By solving the eq.(5.11), the grating function can be defined as shown in Fig.5.5 (c).

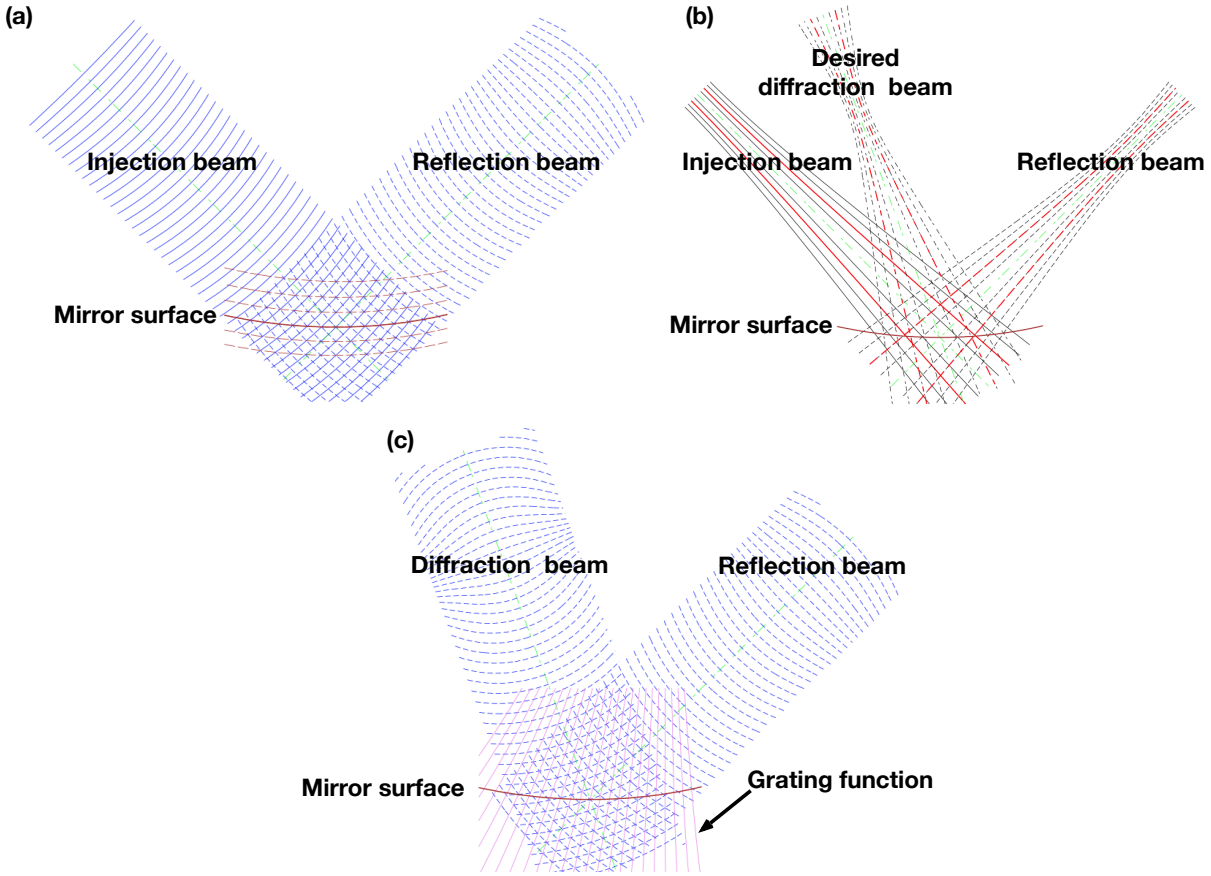

Figure 5.5: (a): Mirror surface calculated by eq.(5.4). (b): Direction of the desired diffraction beam. (c): Definition of the grating function.

Furthermore, the grating efficiency can be optimized by defining grating plane by eq.(5.8). This is equivalent to optimizing blaze angle in order to coincide with the directions of diffraction and reflection on each grating plane. This is a generalization of the method to design a grating on an elliptical mirror support proposed by Tran [4]. So far, only the matching condition of the phase front are discussed. In addition to this phase matching, it is also important to make the intensity profiles match on the mirror/grating surface in order to maintain the purity of the Gaussian beam property. Detailed discussion will be given elsewhere.

5.4 Summary

In this research, development of the grating mirror for the high power transmission system was carried out and its general theory was derived. The development of the plane

grating mirror was carried out in order to separate the fundamental beam and the 2nd harmonics beam. This grating mirror can concentrate the reflection beam and the mth order diffraction beam to the same direction because the shape of the grating has saw-tooth surface. In the results of the low power experiment, although the diffraction beam of the 0th could not be vanished, the fundamental beam and the 2nd harmonics could be separated precisely.

The general theory of the grating mirror was derived. Although the grating mirror is usually plane-shaped because machining or development is easier, it is possible to develop a grating mirror which has arbitrary mirror shape by defining the grating function on the base mirror surface. That is, when Gaussian beam parameters of the injection beam and desired mth order diffraction beam are given, the grating mirror which satisfies the Littrow mount condition can be designed. The grating described in Sec.5.1 was a simple plane grating. We can apply this design method to upgrade this plane grating mirror. Fundamental high power beam can be efficiently focused into a dummy load by designing optimized base mirror. The 2nd harmonics beam can be separated efficiently toward -1st order diffraction direction to form designed Gaussian beam parameter that simplifies the measurement of helical wavefront at the 2nd harmonics frequency. Such an idea of designing a general Littrow mount grating can be applicable to various situations in which normal mirror design is difficult due to limited space or boundary conditions even under high power.

Bibliography

[1] Y. Goto, S. Kubo, and T. I. Tsujimura, "Development of the Grating Mirror for the High Power Transmission System and Its General Theory," Plasma Fusion Res., **13**, 3405089 (2018).

[2] L. D. Landau and E. N. Lifshitz, *The Classical Theory of Fields*, 4th Rev. English Ed., (Butterworth-Heinemann, 1980).

[3] S. Kubo, K. Ohkubo, H. Idei, M. Sato, Y. Takita, M. Iwase, T. Kurodathe, and Torus Group, Fusion Eng. Design, "Antenna and transmission system for high power electron cyclotron heating in a compact helical system," **26**, 319-324, (1995).

[4] M. Q. Tran, H. Cao, J. P. Hogge, W. Kasparek, T. M. Tran, and P. J. Paris, "Properties of Diffraction Gratings Used as Output Couplers in a Quasi-Optical Gyrotron," J. Appl. Phys, **73**, 2089-2102, (1993).

Chapter 6

Development of the Measurement System

In this chapter, we discuss the development of the measurement system for millimeter wave with helical wavefront. Although the cyclotron motion which radiates the vortex beam exists commonly in nature, the vortex radiation has not yet been measured. For this reason, the measurement system for millimeter waves with the vortex property has not yet been developed. The ECE measurements which have already been conducted were focused on one part of the beam or on the beam's phase structure. Given this, we developed the system for measuring vortex beam. We have developed a method to estimate and to identify the Topological Charge (TC) using a vortex beam passively generated from a Gaussian beam.

6.1 Development of the Spiral Mirror

In order to develop the measurement system, we need the vortex beam source in the millimeter wave spectrum. Thus, first we developed a device called a spiral mirror which passively produces vortex beams. We have six kinds of spiral mirrors with every Topological Charge or TC from -3 to +3 except for 0. TC = 0 is a normal mirror. The millimeter wave with a vortex property is generated by conversion from a Gaussian beam from the spiral mirror.

6.1.1 Spiral Mirror with Flat Surface

The simplest mirror has the flat mirror surface. The mirror must have a helical shaped mirror surface to make a reflection beam have a helical wavefront. The helical shaped

mirror surface is defined by

$$x(r,\phi) = r\cos\phi \tag{6.1}$$
$$y(r,\phi) = r\sin\phi \tag{6.2}$$
$$z(r,\phi) = \frac{\phi l d}{2\pi} \tag{6.3}$$

where x, y, and z are the Cartesian coordinate values on the mirror surface; r and ϕ are variables with domains $[0:R]$ and $[0:2\pi]$ on the polar coordinate. R means radius of the mirror and l is equivalent to TC. In addition, d means the height at the mirror origin, and is defined by

$$d = \lambda\cos\theta \tag{6.4}$$

where the θ is the injection angle. The height of the spiral mirror is constant in the radial direction but varies with the azimuthal angle. Therefore, the origin of the spiral mirror is regarded as multivalued function at position $r = 0$. This mirror structure leads to phase singularity of the reflection beam.

6.1.2 Spiral Mirror with Focusing

We also developed the spiral mirrors with focusing. First, we must note that the spiral mirror surface with focusing is not defined by using eq.(5.4) as follows

$$S_{\text{mirror}} = \Phi_{\text{in}} - (\Phi_{\text{out}} + l\phi) = \text{const.} \tag{6.5}$$

Because the constant value which is satisfied with eq.(5.4) is represented by the phase difference value at the intersection point on the beam axis between injection beam and reflection beam, the origin of the mirror surface has only one value. That is, this mirror designed by eq.(6.5) has no singular point on the mirror center.

We resolved this issue, and then developed the spiral mirrors with focusing successfully. In order to design the spiral mirror with focusing, we need the two different types of data. One type of data is that for spiral mirror with flat surface calculated by eq.(6.1) to eq.(6.3). The other data is that for normal mirror with focusing calculated by eq.(5.4). The TC of spiral mirror with flat surface and the curvature of normal mirror with focusing are determined by the spiral mirror with the focusing that we want to design. The normal vector can be defined on the mirror surface. The normal vectors of the spiral mirror with flat surface $\boldsymbol{n}_{\text{flat}}(\boldsymbol{r})$ face only z directions. On the other hand, the normal vectors of the normal mirror with focusing $\boldsymbol{n}_{\text{base}}(\boldsymbol{r})$ face the arbitrary directions. When new normal vectors $\boldsymbol{n}'(\boldsymbol{r})$ can be defined in order to satisfy the relationship below instead of $\boldsymbol{n}_{\text{flat}}(\boldsymbol{r})$, we can obtain the representation of the spiral mirror with focusing (see Fig.6.1).

$$\boldsymbol{n}'(\boldsymbol{r}) \cdot \boldsymbol{n}_{\text{base}}(\boldsymbol{r}) = 0 \tag{6.6}$$

In other words, this means changing the z-value of the spiral mirror with flat surface from the origin so that $\boldsymbol{n}_{\text{flat}}(\boldsymbol{r})$ has the same direction as $\boldsymbol{n}_{\text{base}}(\boldsymbol{r})$.

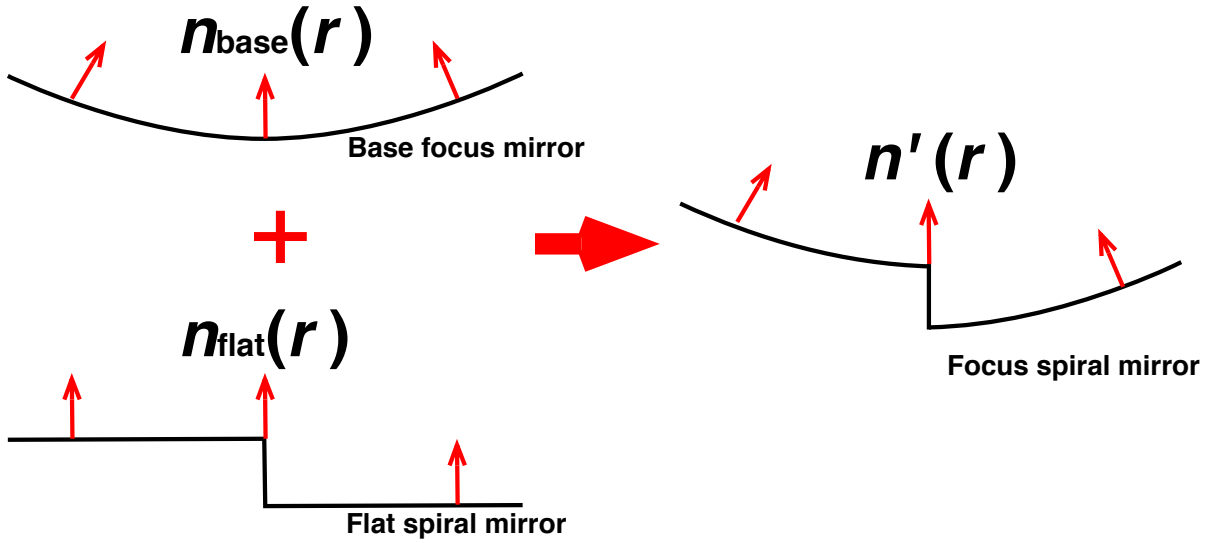

Figure 6.1: Definition of the normal vector on the mirror surface.

6.2 Diffraction Method by a Triangular Aperture

In this section, we will show the measurement method of millimeter-wave radiation with a helical wavefront. We developed a method to estimate a helical wavefront and to identify the TC. This is a diffraction method of a millimeter wave with a helical wavefront by a triangular aperture. The beams in millimeter wave regime are low-energy beams as compared to the beams with shorter wavelength such as γ-ray, X-ray, and ultraviolet. Using a triangular aperture with a larger area is more appropriate for our purpose than are other types of apertures because more diffracted light can be obtained. In addition, other types of apertures such as circular aperture and rectangular aperture also produce the characteristic diffraction patterns. However, these apertures can not identify the differences between the positive TC and the negative TC. This method was successfully confirmed by using the passively generated vortex beam from a Gaussian beam in the millimeter wave regime by a spiral mirror. The characteristic diffraction pattern of the vortex beam by a triangular aperture was observed. Since the diffraction patterns depends on the TC, we can identify the TC of the vortex beam. Actually, diffraction experiments by using several kinds of apertures outside the longer wavelength regime have been carried out, such as diffraction by single slit [25], double slits [8,26,27], triangular aperture [28–31], angular aperture [32], angular double slits [33], and off-axis diffraction by circular aperture [34]. However, a diffraction experiment in the longer wavelength regime including the millimeter wave regime has never been reported. Thus, we will report the diffraction pattern in millimeter wave with helical wavefront for the first time.

6.2.1 Experimental Setup

The diffraction experiment was carried out as shown in Fig.6.2. The millimeter wave with a helical wavefront was generated by conversion from a Gaussian beam from the spiral mirror [35]. Fig.6.3 shows a photograph of the spiral mirror. The z_{m} value (height) of the spiral mirror is constant in the radial direction but varies with the azimuthal angle. The size of the mirror is 130 mm $\times$ 130 mm, which size makes it possible to reflect the beam at least over 90 %. The quality of the beam generated by the spiral mirror depends on the accuracy of the manufacturing whether the height in the azimuthal angle changes smoothly and the step changes sharply or not. If the spiral mirrors have different from the calculated values, the several beams with different TC will be mixed. In this case, the donut-shaped intensity distribution, which is one of the characteristics of the vortex beam, does not appear. But C-shaped intensity distribution appears, or the diffraction patterns which correspond to superposition of the diffraction patterns of each TC appear. Spiral mirrors were manufactured using end mill with a diameter of 0.75 mm. The accuracy of the manufacturing is approximately the diameter of the end mill. However, the minimum wavelength of the millimeter wave used in this study is approximately 1.8 mm. Thus, the spiral mirror is considered to have the accuracy of manufacturing less than one-half of the wavelength. In the experiment, the donut-shaped intensity distribution which is compatible with the calculation result was observed as shown in Fig.6.4. It was also confirmed that only a diffraction pattern by one TC appeared. Therefore, we have successfully confirmed that the vortex beam in millimeter wave with high accuracy has been generated in the experiment. Here, the millimeter-wave used in the experiment has a wavelength of 1.8 mm to 3.6 mm, which is sufficiently long compared to the scratch on the mirror surface as shown in Fig.6.3, and the reflection characteristics do not depend on the mirror surface condition. Furthermore, we also developed the spiral mirror with focusing abilities. The difference of the z_{m} value at the step (at $\phi_{\mathrm{m}} = 0$) depends on the TC of the vortex beam we would like to generate, and on the injection angle. The origin of the spiral mirror has a singular point which is indefinite in z_{m} value. These spiral mirrors are specialized in 45 deg. injection and reflection. We have 6 kinds of spiral mirrors with TC from -3 to +3 except for 0. The Gaussian beam with frequency 154 GHz, power 12-15 mW (measured by Mm Wave high sensitive power meter with model DPM-06 produced by ELVA-1,), and wavelength 1.95 mm were injected into the spiral mirror. Millimeter Wave Broadband BWO source with model G4-143g produced by ELVA-1 was used as the power source. The convex lens was installed between the oscillator and the spiral mirror for focusing the beam waist. The vortex beam generated by the spiral mirror was then injected into the triangular aperture, where the diffracted beam was measured by a sub-THz camera (Terahertz camera with model T30/64/64 produced by Terasense Group Inc.). The high-precision alignment was performed so that the optical axis and the center of gravity of the triangular aperture coincide. The distance from the oscillator to the convex lens was 280 mm, from the convex lens to the spiral mirror was

480 mm, from the spiral mirror to the aperture was 200 mm, and from the aperture to the camera was 250 mm, respectively.

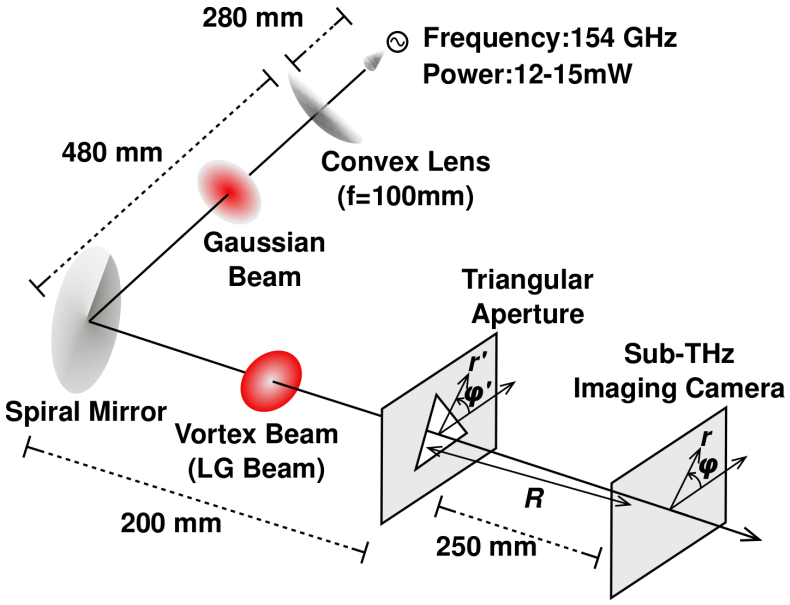

Figure 6.2: Experimental setup [16]: Sub-THz Imaging camera has a sensor size of 192×192 mm and 64×64 pixels, totaling 4096 pixels. The power sensitivity per pixel has 4 - 45 nW/pixel, which depends on the exposure. Frequency sensitivity also has the range from 0.02 THz (20 GHz) to 0.7 THz (700 GHz).

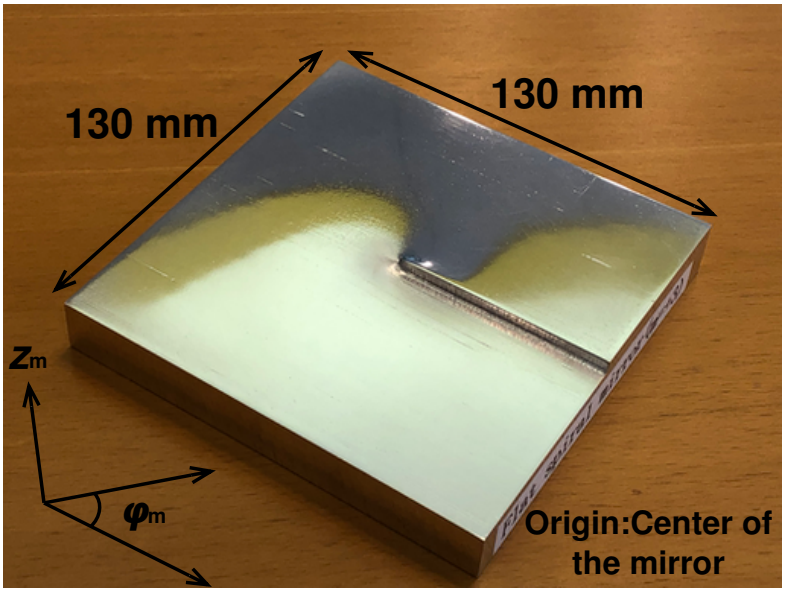

Figure 6.3: Spiral mirror with TC = +3. The origin has a singular point with indefinite z_{m} value, and then the step (at $\phi_{\mathrm{m}} = 0$) depends on TC of the vortex beam and on the injection angle [16].

6.2.2 Huygens-Fresnel Principle

In the calculation, an LG beam was used for the millimeter vortex beam. An LG beam is represented as follows [1],

$$E(r,\phi,z,t) = \sqrt{\frac{2p!}{\pi(p+|l|!)}}\frac{1}{w(z)}\left(\frac{r\sqrt{2}}{w(z)}\right)^{|l|} L_p^{|l|}\left(\frac{2r^2}{w^2(z)}\right) \times e^{\frac{-r^2}{w^2(z)}} e^{\frac{-ikr^2}{2R(z)}} e^{-i(2p+|l|+1)\tan^{-1}(\frac{z}{z_R})} e^{-il\phi} e^{i(kz-\omega t)} \tag{6.7}$$

where E is the electric field; r, z, and ϕ are parameters in the cylindrical coordinate system; p and l are radius index and azimuthal index (l is equivalent to TC); L is associated Laguerre polynomials with p and l; w, k, R, and z_R are waist size, wave-number, radius of curvature, and Rayleigh length, respectively. ω and t are angular frequency and time. Diffraction by an aperture was calculated by the Huygens-Fresnel principle as follows [36],

$$D(r,\phi,z,t) = \frac{1}{4\pi}\oint_s \mathrm{d}\boldsymbol{S}' \cdot \left(\frac{\nabla' E(r',\phi',z',t')}{R} + \frac{\boldsymbol{R}}{R^3}E(r',\phi',z',t') - \frac{\boldsymbol{R}}{cR^2}\frac{\partial E(r',\phi',z',t')}{\partial t'}\right)_{t'=t-\frac{R}{c}} \tag{6.8}$$

where c and t' are light speed and observer time, that is, retarded time, and $\mathrm{d}\boldsymbol{S}'$ means the integration on the aperture area. Fraunhofer diffraction can be applied when the distance between the light source or screen and the aperture has an infinite value. In addition, when the wave with planer equiphase front arrives to the aperture, Fraunhofer diffraction can be applied as well even if the distance has a finite value. However, Fresnel diffraction should be applied in the wave with longer wavelength regime such as millimeter waves where diffraction effect is strong. This is because this equation is a strict mathematical expression of the Huygens-Fresnel principle. Thus, we can calculate a diffraction phenomenon even though the millimeter wave has a stronger diffraction effect.

6.2.3 Experiment and Calculation Results

Fig.6.4 shows the intensity distributions with radial index $p = 0$ and azimuthal index (equivalent to TC) $l = 1$ on the aperture position. The left figure represents the calculation of the intensity distribution from an LG beam, and the right figure shows the intensity distribution of the measured result. We can see that the experimental result clearly had the donut-shaped intensity distribution which was the characteristic of the vortex beam. Here, it was assumed that the calculated vortex beam had waist size of 13 mm in the light of the measured intensity distribution on the aperture position. Also, the white line with triangle represents the size of the triangular aperture. As we can see, an equilateral triangular aperture with sides of 40 mm was used in this experiment. This size was large enough for the vortex beam to pass through the aperture. Actually, diffraction patterns appear more clearly if the size of the aperture is much smaller. However, in that case, most of the power of the vortex beam is cut off at the outside frame of the aperture. The power of the vortex beam before passing through the aperture was ten or more mW. However, only a power of at least 10 mW can be detected by the camera. In other words, the diffraction power is larger than minimal pixel sensitivity at the pixels where the polka-dot patterns are formed if we use the power source as the LG beam with 10 mW. Note that this value completely depends on the experimental setup, especially the aperture size, beam size on the aperture position, and pixel sensitivity. Note that this value totally depends on the experimental setup, especially the aperture size, beam size on the aperture position, pixel sensitivity. Therefore, we set the sides of the aperture to 40 mm, which allowed the power to pass through sufficiently.

Fig.6.5 shows the diffraction patterns by a triangular aperture of a millimeter wave with a helical wavefront. Fig.6.5(a) shows the case of negative TC, which is -1, -2, and -3 from top to bottom. Fig.6.5(b) shows the case of positive TC, which is 1, 2, and 3 from top to bottom. In both figures, the left column represents the calculation results and the right column represents the experimental results. For generating several types of vortex beams, we had to replace the spiral mirror each time. Because it was an important factor that the center of gravity of the aperture coincides with the optical axis of the vortex beam, precise alignment had to be carried out each time. In the experiment, we

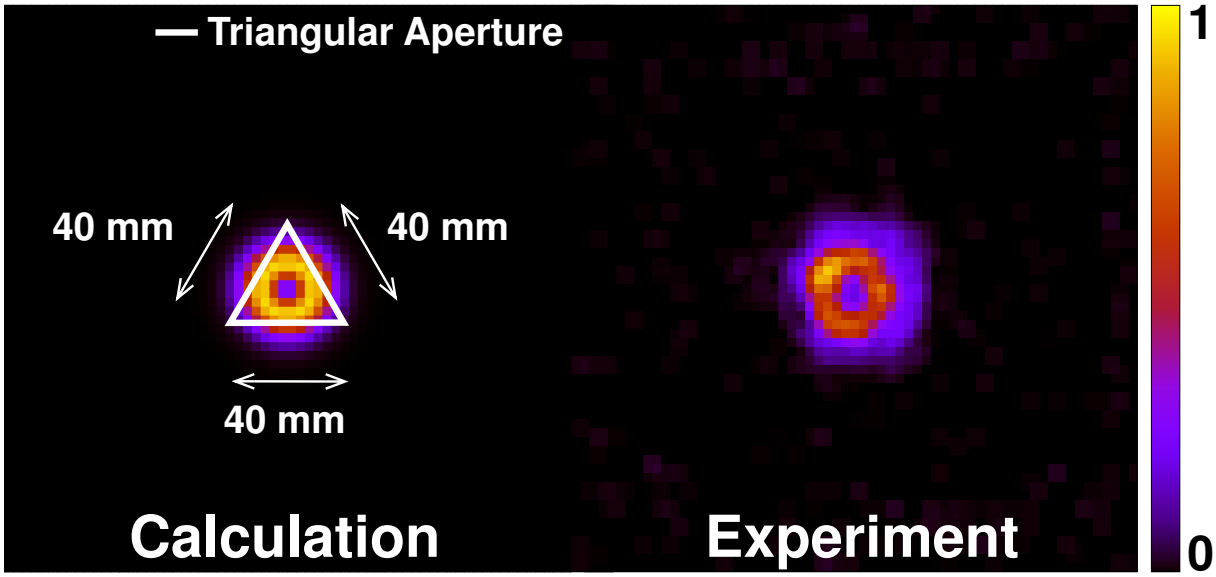

Figure 6.4: Intensity distributions of the millimeter wave in 154 GHz with a helical wavefront at the aperture position [16]. The left figure shows the calculated intensity distribution by eq.(6.7) with waist size 13 mm. The right figure shows the measured intensity distribution. Both figures had clear donut-shaped intensity distribution. Scale of both the vertical axis and the horizontal axis were 200 mm, and the intensity with linear scale was normalized by being maximum value 1. Next, white line with triangle on the left figure represents size of the triangular aperture. The optical axis of the vortex beam coincided with the center of gravity of the triangular aperture. Then the bright ring became slightly larger than the inscribed circle.

obtained the characteristic diffraction patterns which resemble polka-dot patterns. The diffraction patterns were also calculated by the Huygens-Fresnel principle in eq.(6.8). These calculation results were perfectly compatible with the experimental results. Also, as can be seen, these diffraction patterns depended on TC, and negative TC and positive TC were symmetric pairs under reflection. Here, it can be seen that the unevenness of the diffraction patterns appear in the experiment. This is because the deviation between the center of gravity of the triangular aperture and the optical axis of the vortex beam appeared. The calculation results show the ideal situation without these deviations, but it has been found in the calculation that if these centers are slightly shifted, the unevenness appears on the diffraction pattern. In the experiment, precise alignment was carried out so that the unevenness of these centers disappeared. However, the alignment was not perfect. Thus, the unevenness appeared. Note that the diffraction powers measured far from the polka-dot patterns indicate the noise level. Therefore, we were able to estimate the vortex property and identify the TC even in the millimeter wave regime.

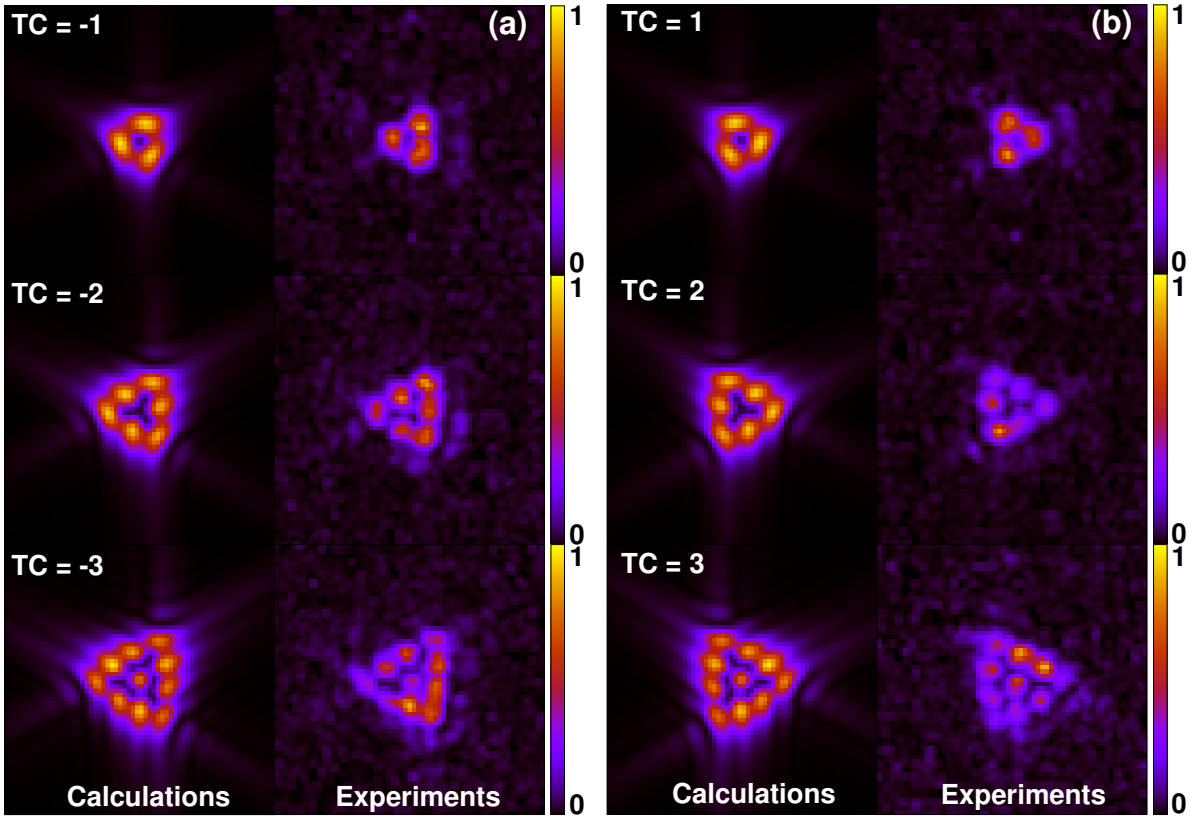

Figure 6.5: (a): Diffraction patterns by the millimeter wave with a helical wavefront with negative TC. The left row shows the calculation results. The right row shows the experimental results. Top figures show TC $= -1$, middle figures show the TC $= -2$, and bottom figures show TC $= -3$. Scale of both the vertical axis and the horizontal axis are 200 mm, and then the intensity is normalized by being maximum value 1. (b): Same as Fig. 4(a), but the sign of the TC is positive [16].

Finally, Fig.6.6 shows the diffraction patterns by a triangular aperture of a millimeter wave without a vortex property, that is, only a Gaussian beam. As we can see, the characteristic diffraction patterns did not appear when the injected beam had no vortex property. This result is also important for identifying between a vortex beam and a Gaussian beam.

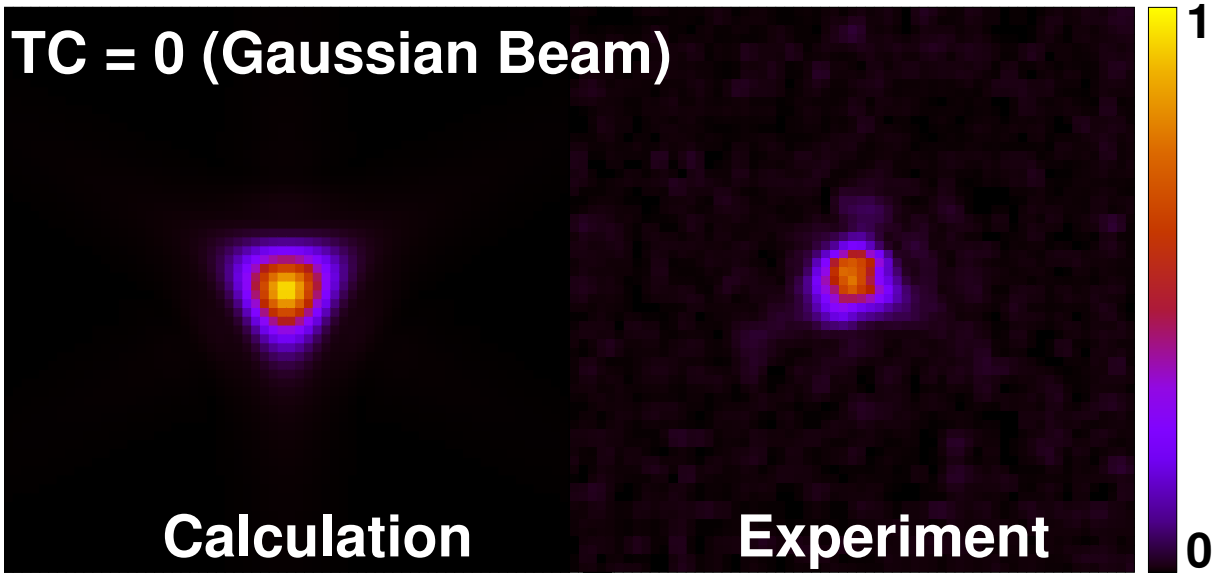

Figure 6.6: Diffraction patterns by the Gaussian millimeter wave (this is equivalent to TC = 0). The left figure shows the calculation result. The right figure shows the experimental result. In the case of the Gaussian beam, the characteristic diffraction pattern did not appear [16].

6.3 Direct Phase Measurement

In this section, we will show the measurement method by heterodyne system for vortex beam with high frequency. As I mentioned, the phase structure of the vortex beam has spatial dependence by azimuthal angle ϕ. That is, for example in the case of $l = 1$, there is the phase difference of 180 deg. when we compare the phase at the two azimuthal angles between $\phi = 0$ deg. and $\phi = 180$ deg. Also, in the case of $l = 2$, there is the phase difference of 360 deg. If we can detect the phase difference directly in addition to the intensity distribution with donut-shaped, the vortex beam can be identified. Therefore, we developed measurement system using heterodyne systems, which are arranged at two spatial points and detect the phase difference.

6.3.1 Heterodyne System

Heterodyne System is one of the measurement system for high frequency signal over 100 GHz which is difficult to be detected by Analog-to-Digital Converter (ADC). However, it is possible to down-convert the high frequency signal to MHz regime with maintaining amplitude and phase by the heterodyne system. As shown in Fig.6.7, the heterodyne system mainly composed of signal combiner called mixer and Local Oscillator (LO). Mixer is a circuit element where the input signal E_R and the LO signal E_L are multiplied by

each other. To put it simply, we consider the signals E_R and E_L below,

$$E_R = E_{R,A}\cos(\omega_R t + \phi_R) \tag{6.9}$$
$$E_L = E_{L,A}\cos(\omega_L t + \phi_L) \tag{6.10}$$

where $E_{R,A}$ and $E_{L,A}$ are amplitude. ω_R and ω_L are frequency. ϕ_R and ϕ_L are initial phase. Then, by multiplying each other

$$\begin{aligned} E_{\rm IF} &= E_R E_L \\ &= E_{R,A}E_{L,A}\frac{\cos\{(\omega_R+\omega_L)t+\phi_R+\phi_L\}+\cos\{(\omega_R-\omega_L)t+\phi_R-\phi_L\}}{2} \end{aligned} \tag{6.11}$$

where $E_{\rm IF}$ is Intermediate Frequency (IF) signal with $\omega_{\rm IF} = \omega_R - \omega_L$. That is, the mixer generates two different frequency components. The high frequency component with $\omega_R + \omega_L$ can be filtered by band pas filter. Therefore, when the frequency of LO is decided properly so that the $\omega_{\rm IF}$ becomes MHz regime, we can obtain the output signal which is down-converted to MHz regime.

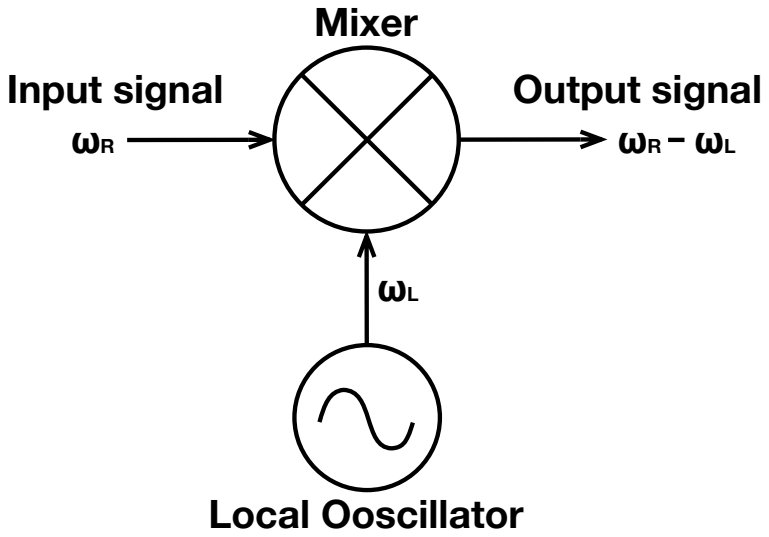

Figure 6.7: Operation principle of the heterodyne method. The input signal is down-converted by multiplying LO signal using mixer.

6.3.2 Two Spatial Points Measurement by Heterodyne Detectors

Two spatial points measurement by heterodyne systems is designed as shown in Fig.6.8. The measurement system has two antennas so that the high frequency signal can be

detected at two spatial points. In the next to antenna, the Orthomode Transducer (OMT) has been installed. The OMT is a waveguide component which can decompose the electric field with two orthogonal field components into each orthogonal component. Therefore, the polarization of the vortex beam can also be identified by this system. The down-converted each signal is detected by ADC through filters and amplifiers.

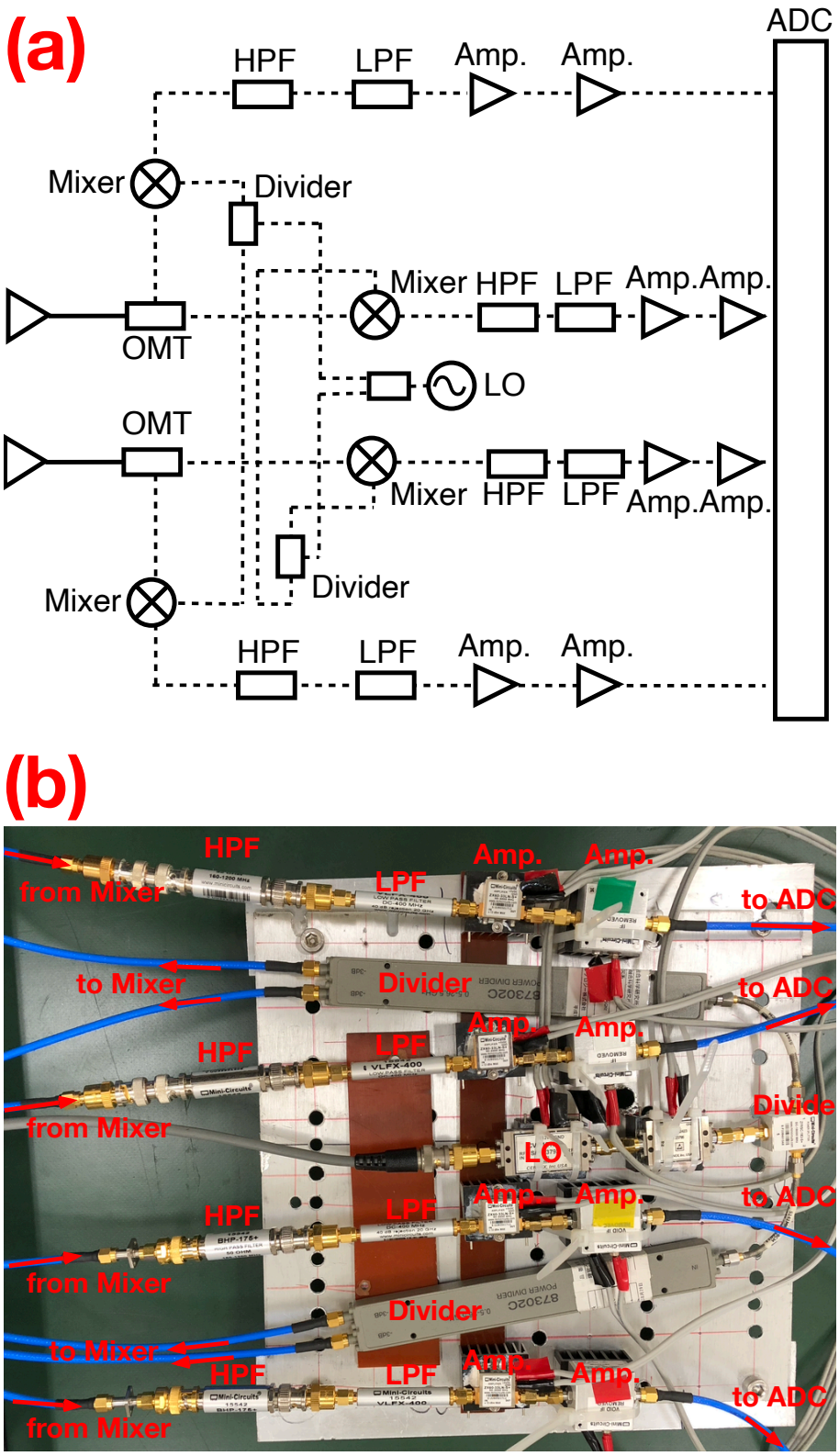

Figure 6.8: Two spatial points measurement by heterodyne system. This measurement system has OMT after antenna so that the polarization of the vortex beam can be identified.

6.4 Summary

In this chapter, we carried out a diffraction experiment by a triangular aperture using passively generated millimeter waves with a helical wavefront, using a spiral mirror. In the experiment, donut-shaped intensity distribution was measured at the aperture position. Based on this intensity distribution, diffraction patterns were calculated using the Huygens-Fresnel principle, which had characteristic diffraction patterns that resemble polka-dot patterns. In the experiment, the same pattern was measured. It became obvious that these diffraction patterns depend on the TC, and that negative TC and positive TC had reflection symmetry. Therefore, we were able to estimate a millimeter wave with a helical wavefront and to identify the TC. In the future, we will adapt this diffraction method by a triangular aperture to a measurement of actively generated ECE. Then we will experimentally demonstrate the vortex property of ECE.

In addition, we developed measurement system for directly identifying the phase difference at two spatial points by heterodyne system. Heterodyne system has a great characteristic regarding measurement for high frequency signal over 100 GHz, which is difficult to be detected by ADC. The spatial phase structure of vortex beam can be identified by detecting the phase difference at the two spatial point even in high frequency signal.

Bibliography

[1] L. Allen, M. W. Beijersbergen, R. J. C. Spreeuw, and J. P. Woerdman, "Orbital angular momentum of light and the transformation of Laguerre-Gaussiean laser modes," Phys. Rev. A, **45**, 8185 (1992).

[2] J. Courtial and K. O'Holleran, "Experiments with twisted light," Eur. Phys. J. Special Topics **145**, 35-47 (2007).

[3] L. Marrucci, C. Manzo, and D. Paparo, "Optical Spin-to-Orbital Angular Momentum Conversion in Inhomogeneous Anisotropic Media," Phys. Rev. Lett., **96**, 163905 (2006).

[4] S. F. Busch, J. C. Balzer, G. Bastian, G. E. Town, and M. Koch, "Extending the Alvarez-Lens Concept to Arbitrary Optical Devices: Tunable Gratings, Lenses, and Spiral Phase Plates," IEEE Trans. Terahertz Sci. Technol., **7**, 3, 320-325, (2017).

[5] S. Sasaki and I. McNulty, "Proposal for Generating Brilliant X-Ray Beams Carrying Orbital Angular Momentum," Phys. Rev. Lett., **100**, 124801 (2008).

[6] J. Bahrdt, K. Holdack, P. Kuske, R. Muller, M. Scheer, and P. Schmid, "First Observation of Photons Carrying Orbital Angular Momentum in Undulator Radiation," Phys. Rev. Lett., **111**, 034801 (2013).

[7] M. Katoh, M. Fujimoto, H. Kawaguchi, K. Tsuchiya, K. Ohmi, T. Kaneyasu, Y. Taira, M. Hosaka, A. Mochihashi, and Y. Takashima, "Angular Momentum of Twisted Radiation from an Electron in Spiral Motion," Phys. Rev. Lett., **118**, 094801 (2017).

[8] M. Katoh, M. Fujimoto, N. S. Mirian, T. Konomi, Y. Taira, T. Kaneyasu, M. Hosaka, N. Yamamoto, A. Mochihashi, Y. Takahashi, K. Kuroda, A. Miyamoto, K. Miyamoto, and S. Sasaki, "Helical Phase Structure of Radiation from an Electron in Circular Motion," Sci. Rep., **7**, 6130 (2017).

[9] Y. Taira, T. Hayakawa, and M. Katoh, "Gamma-ray vortices from nonlinear inverse Thomson scattering of circularly polarized light," Sci. Rep., **7**, 5018 (2017).

[10] Y. Taira and M. Katoh, "Generation of Optical Vortices by Nonlinear Inverse Thomson Scattering at Arbitrary Angle Interactions," Astrophys. J., **860**, 11 (2018).

[11] T. Maruyama, T. Hayakawa, and T. Kajino, "Compton Scattering of γ-Ray Vortex with Laguerre Gaussian Wave Function," Sci. Rep., **9**, 51 (2019).

[12] S. Matsuba, K. Kawase, A. Miyamoto, S. Sasaki, M. Fujimoto, T. Konomi, N. Yamamoto, M. Hosaka, and M. Katoh, "Generation of vector beam with tandem helical undulators," Appl. Phys. Lett., **113**, 021106 (2018).

[13] T. Kaneyasu, Y. Hikosaka, M. Fujimoto, T. Konomi, M. Katoh, H. Iwayama, and E. Shigemasa, "Limitations in photoionization of helium by an extreme ultraviolet optical vortex," Phys. Rev. A, **95**, 023413, (2017).

[14] Y. Taira and M. Katoh, "Gamma-ray vortices emitted from nonlinear inverse Thomson scattering of a two-wavelength laser beam," Phys. Rev. A, **98**, 052130, (2018).

[15] T. Kaneyasu, Y. Hikosaka, M. Fujimoto, H. Iwayama, M. Hosaka, E. Shigemasa, and M. Katoh, "Observation of an optical vortex beam from a helical undulator in the XUV region," J. Synchrotron Rad., **24**, 934-938, (2017).

[16] Y. Goto, T. I. Tsujimura, and S. Kubo, "Development of the Grating Mirror for the High Power Transmission System and Its General Theory," Plasma Fusion Res., **13**, 3405089 (2018).

[17] Y. Yan, G. Xie, M. P.J. Lavery, H. Huang, N. Ahmed, C. Bao, Y. Ren, Y. Cao, L. Li, Z. Zhao, A. F. Molisch, M. Tur, M. J. Padgett, and A. E. Willner, "High-capacity millimetre-wave communications with orbital angular momentum multiplexing," Nat. Commun., **5**, 4876, (2014).

[18] N. Bozinovic, Y. Yue, Y. Ren, M. Tur, P. Kristensen, H. Huang, A. E. Willner, and S. Ramachandran, "Terabit-Scale Orbital Angular Momentum Mode Division Multiplexing in Fibers," Science, **340**, 4876, (2013).

[19] X. Hui, S. Zheng, Y. Chen, Y. Hu, X. Jin, H. Chi, and X. Zhang, "Multiplexed Millimeter Wave Communication with Dual Orbital Angular Momentum (OAM) Mode Antennas," Sci. Rep., **5**, 10148, (2015).

[20] S. Yu, L. Li, and G. Shi, "Dual-polarization and dual-mode orbital angular momentum radio vortex beam generated by using reflective metasurface," Appl. Phys. Express, **9**, 082202, (2016).

[21] S. Yu, L. Li, G. Shi, C. Zhu, and Y. Shi, "Generating multiple orbital angular momentum vortex beams using a metasurface in radio frequency domain," Appl. Phys. Lett., **108**, 241901, (2016).

[22] H. Wu, J. Tang, Z. Yu, J. Yi, S. Chen, J. Xiao, C. Zhao, Y. Li, L. Chena, and S. Wen, "Electrically optical phase controlling for millimeter wave orbital angular momentum multi-modulation communication," Opt. Commun., **393**, 49-55 (2017).

[23] F. Tamburini, E. Mari, B. Thidé, C. Barbieri, and F. Romanato, "Experimental verification of photon angular momentum and vorticity with radio techniques," Appl. Phys. Express, **99**, 204102, (2011).

[24] A, E. Willner, Y. Ren, G. Xie, Y. Yan, L. Li, Z. Zhao, J. Wang, M. Tur, A. F. Molisch, and S. Ashrafi, "Recent advances in high-capacity free-space optical and radio-frequency communications using orbital angular momentum multiplexing," Phil. Trans. R. Soc. A, **375**, 20150439, (2017).

[25] D. P. Ghai, P. Senthilkumaran, and R. Sirohi, "Single-slit diffraction of an optical beam with phase singularity," Opt. Laser. Eng., **47**, vol. 1, 123-126, (2009).

[26] S. Zheng and J. Wang, "Measuring Orbital Angular Momentum (OAM) States of Vortex Beams with Annular Gratings," Sci. Rep., **7**, 40781 (2017).

[27] H. I. Sztul and R. R. Alfano, "Double-slit interference with Laguerre–Gaussian beams," Opt. Lett., **31**, 31, (2006).

[28] L. E. E. de Araujo and M. E. Anderson, "Measuring vortex charge with a triangular aperture," Opt. Lett., **36**, 36, (2011).

[29] J. M. Hickmann, E. J. S. Fonseca, W. C. Soares, and S. Chavez-Cerda, "Unveiling a Truncated Optical Lattice Associated with a Triangular Aperture Using Light's Orbital Angular Momentum," Phys. Rev. Lett., **105**, 053904 (2016).

[30] A. Mourka, J. Baumgartl, C. Shanor, K. Dholakia, and E. M. Wright, "Visualization of the birth of an optical vortex using diffraction from a triangular aperture," Opt. Express, **19**, 7, (2011).

[31] Y. Taira and Y. Kohmura, "Measuring the topological charge of an x-ray vortex using a triangular aperture.pdf," J. Opt., **21**, 045604, (2019).

[32] C. S. Guo, L. L. Lu, and H. T. Wang, "Characterizing topological charge of optical vortices by using an annular aperture," Opt. Lett., **34**, 23, (2009).

[33] D. Fu, D. Chen, R. Liu, Y. Wang, H. Gao, F. Li, and P. Zhang, "Probing the topological charge of a vortex beam with dynamic angular double slits," Opt. Lett., **40**, 5, (2015).

[34] Y. Taira and S. Zhang, "Split in phase singularities of an optical vortex by off-axis diffraction through a simple circular aperture," Opt. Lett., **42**, 7, (2017).

[35] D. P. Ghai, P. Senthilkumaran, and R. Sirohi, "Adaptive helical mirror for generation of optical phase singularity," Appl. Opt., **47**, 10, 1378-1383, (2008).

[36] S. Sunakawa, "Riron Denjikigaku" 3rd ed. [in Japanese] (Theoretical Electromagnetism), Kinokuniya, Tokyo, (2010).

Chapter 7

Summary

In this dissertation, we carried out comprehensive researches from 1) - 4) for experimentally demonstrating an ECE with helical wavefront.

1) Numerical calculation regarding ECE with a helical wavefront from an electron accelerated by a circularly polarized wave.
We have successfully calculated the ECE with helical wavefront from an electron in cyclotron motion under the magnetic field. In this calculation, a RHCP wave was applied to an electron with cyclotron motion under the magnetic field from the outside.

   In the case of a static uniform magnetic field, when the RHCP wave is applied to the electron with cyclotron motion, the electron receives energy from the incident RHCP wave and the relativistic mass gradually increases. Thus, the Larmor radius increases and the cyclotron frequency decreases. Meanwhile, the electron is accelerated in the z-direction (magnetic field direction) by the Lorentz force $\boldsymbol{\beta}_{\perp} \times \boldsymbol{B}_{\mathrm{in}}$, and reaches a relativistic velocity. In this case, the frequency of the RHCP wave seen from the reference frame of electron is observed to be downshifted due to the Doppler effect. The results confirmed a phenomenon called cyclotron auto-resonance, i.e., the relativistic electron cyclotron frequency and the downshifted frequency of RHCP wave seen from the reference frame of electron are almost equal and electron maintains the resonance state. In addition, it was confirmed that the direction of the externally applied electric field and the acceleration direction of the electron were in the same direction. Also, the electron was trapped by the RHCP wave. Although this calculation is performed for a single electron, the same phenomenon occurs for each electron in a multi-electron system. Therefore, by applying RHCP wave to a multi-electron system with a initial random rotational phase, the rotational phase of each electron is controlled and coherent radiation with a helical wavefront can be obtained.

   Radiation from the electron in a such a state was calculated using the Liénard-

Wiechert potential and observed on the upper hemisphere. As a result, only the fundamental radiation appears in the frequency spectrum on the z-axis ($\theta = 0$), and the spectrum of higher harmonics radiation did not appear. However, a spectrum of radiation including higher harmonics was observed at a position away from the optical axis. The absence of harmonics radiation on the optical axis (z-axis) indicates that the intensity distribution of higher harmonics radiation is donut-shaped. This indicates that active radiation from the charged particle with spiral motion produces helical wavefront - one of the characteristics of the vortex beam. In addition, we calculated the phase difference of the radiation at the symmetric point with respect to the beam axis. The higher harmonics have the phase difference with the relationship of $180(n-1)$ deg., while the fundamental radiation has no phase difference. These results suggest that ECE has a helical wavefront from the characteristics of donut-shaped intensity distribution and azimuth-dependent phase structure.

The same calculation was performed for the magnetic mirror field. We confirmed that ECE has a helical wavefront even in the magnetic mirror field, which can be easily realized experimentally. ECE with a helical wavefront will be generated by interaction between the electrons with cyclotron motion in the magnetic mirror field accelerated by the externally applied RHCP wave.

2) Development of the experimental device producing ECE with a helical wavefront.

We designed and constructed the experimental device that generates the ECE with helical wavefront based on the numerical calculation as mentioned in point 1). We created magnetic mirror configuration by the use of superconducting coils. Into such magnetic field, we supplied a group of electrons. An electron gun at the bottom of the device was used as source. The group of electrons follows cyclotron motion and travels to the interaction region. Then, the RHCP wave is applied from the outside to accelerate the electron at the resonance region and control the rotation phase. As a result, coherent cyclotron radiation including fundamental radiation and higher harmonics radiation can be obtained. However, since these optical axes regarding fundamental radiation and higher harmonics radiation are coaxial, they are separated into fundamental and second harmonic radiation by a grating mirror. The separated fundamental radiation is guided to the dummy load, and the second harmonic radiation is measured by the measurement system. This experimental device has already been designed and constructed, including a transmission system for guiding the RHCP wave from the gyrotron.

3) Development of the grating mirror and its general theory.

A grating mirror has been developed to separate only the second harmonic radiation from the fundamental and higher harmonics radiation in the experimental device of 2). A grating mirror with a blaze angle and line spacing that satisfies

the Littrow condition is designed so that the second harmonic radiation can be effectively separated. In other words, the line spacing of the grating mirror and the blaze angle is optimized so that the propagation direction of the -1st order wave diffracted by the grating and the wave reflected on the slope on the saw-tooth is the same. Therefore, low power second harmonic radiation can be effectively measured. This grating mirror is a planar type for the convenience of machining, but in this study, we generalized the design method of the grating mirror and succeeded in defining a grating mirror with an arbitrary surface shape. When parameters, such as the focal point and the waist size of the input Gaussian beam and output of the m-th order diffracted wave, are given, a grating can be designed on the mirror surface.

4) Development of the measurement system for a beam with helical wavefront by a triangular aperture.

We have developed a measurement system to detect a helical wavefront radiation separated by a grating mirror. Although the radiation with a helical wavefront is common in nature, that radiation has not been measured yet. This is either because of the lack of measurement system or attempt to measure the a helical wavefront. Here, the diffraction method by an aperture is excellent because the diffraction can be caused by each photon, that is, the helical wavefront can be identified even if it is not coherent radiation. However as I mentioned, since the harmonics ECE has have low power, it is important to produce a spatially coherent electrons by the externally applied electromagnetic wave for improving the sensitivity of the measurement.

Given this, we developed a diffraction method of the wave with helical wavefront using a triangular aperture. In order to develop the measurement system, we need the beam source with a helical wavefront in the millimeter wave spectrum. First we developed a device called a spiral mirror which passively convert a Gaussian beam into vortex beams. The mirror surface of the spiral mirror has a helical shape, which changes continuously in the azimuth direction and the mirror center is a singular point whose height is not defined. We have developed six kinds of spiral mirrors, one for every Topological Charge (TC) from -3 to +3 except for 0. TC = 0 is a normal mirror. We have also confirmed that each mirror produced a donut-shaped intensity distribution. Therefore, since we have obtained a stable continuous-wave source with a helical wavefront, the measurement system can be developed.

According to the Huygens-Fresnel principle, when a beam with helical wavefront passes through the aperture, characteristic diffraction pattern appears according to its TC. In the case of a triangular aperture, the symmetric diffraction pattern appears depending on the sign of TC. Using a triangular aperture with a larger area is more appropriate for our purpose than other types of aperture because more diffracted light can be obtained. In the experiment, an equilateral triangular aperture with a side of 40 mm was used. Also, the aperture's optical system was designed

and calibrated so that the optical axis and the center of gravity of the triangular aperture coincide. In the experiment, we obtained the characteristic diffraction patterns which resembled polka dot patterns. The data acquisition was made by a sub-THz imaging camera. These experimental results were perfectly compatible with the calculation results based upon Kirchhoff's diffraction formula, which is an exact mathematical expression of the Huygens-Fresnel principle. In addition, we also confirmed that the characteristic diffraction patterns did not appear when the Gaussian beam without a helical wavefront was injected into a triangular aperture. Therefore, we were able to detect a millimeter-wave with a helical wavefront and to identify the TC.

This diffraction method by an aperture can be applied to the radiation without phase coherence because the pattern is a result of self interference pattern for diffracted and non-diffracted beam.